6. SITE 899[1]

Shipboard Scientific Party[2]

HOLE 899A

Date occupied: 26 April 1993

Date departed: 29 April 1993

Time on hole: 2 days, 10 hr, 50 min

Position: 40°46.332'N, 12°12.156'W

Bottom felt (drill-pipe measurement at rig floor, m): 5302.5

Distance between rig floor and sea level (m): 11.54

Water depth (drill-pipe measurement from sea level, m): 5291.0

Total depth (with rig floor, m): 5538.00

Penetration (m): 235.50

Number of cores (including cores having no recovery): 16

Total length of cored section (m): 154.00

Total core recovered (m): 51.45

Core recovery (%): 33

Oldest sediment cored:
Depth (mbsf): 235.5
Nature: claystone
Age: early Miocene
Measured velocity (km/s): 1.64

HOLE 899B

Date occupied: 29 April 1993

Date departed: 10 May 1993

Time on hole: 11 days, 14 hr, 24 min

Position: 40°46.347'N, 12°16.063'W

Bottom felt (drill-pipe measurement at rig floor, m): 5302.5

Distance between rig floor and sea level (m): 11.54

Water depth (drill-pipe measurement from sea level, m): 5291.0

Total depth (from rig floor, m): 5865.00

Penetration (m): 562.50

Number of cores (including cores having no recovery): 37

Total length of cored section (m): 332.0

Total core recovered (m): 173.98

Core recovery (%): 52

Oldest sediment cored:
Depth (mbsf): 549.70
Nature: claystone
Age: Barremian
Measured velocity (km/s): 4.30

Hard rock:
Depth (mbsf): 484.2-557.92
Nature: serpentinite/serpentinized peridotite/gabbro
Measured velocity (km/s): 3.0-6.8

Principal results: Site 899 is situated in the Iberia Abyssal Plain, within the ocean/continent transition (OCT) zone over a semi-elliptical basement ridge having a steep southern flank. Geophysical modeling had predicted that the ridge lay within a part of the OCT, intermediate between thin oceanic crust to the west and thinned continental crust to the east, in which a large positive magnetic anomaly that cannot be modeled by seafloor spreading is found. The site is one of a transect of sites across the OCT designed to study the petrologic changes in the basement rocks within the OCT to identify the processes that accompanied continental breakup and the onset of steady-state seafloor spreading. Rotary cores were obtained from two holes that penetrated a total of 562.5 m of late Pliocene to Late Cretaceous age sediments overlying an unusual serpentinite breccia and serpentinized peridotite having interbedded pre-Late Cretaceous to late Barremian claystone and siltstone. Coring was terminated when the drill string became temporarily trapped near the bottom of the hole. Downhole logs were acquired from within acoustic basement in the interval from 395 to 430 mbsf; deeper logging was prevented by bridges and, when we tried to log from the base of the casing to the top of basement, bridges stopped the logging tools in that interval, too.

1. A 2.9-m.y. hiatus in the middle/late Miocene, correlatable with a regional angular unconformity on seismic reflection profiles, may be related to a compressional phase within the Betic Mountains in southeastern Spain, and structural inversion in the Lusitanian Basin of Portugal.
2. A major hiatus representing most of the Paleogene lies within Core 149-899B-15R (about 360-370 mbsf).
3. Acoustic basement is composed of a series of at least three serpentinite breccia units that overlie discrete sections of serpentinized peridotite, gabbro, and intercalated Early Cretaceous age claystones and siltstones with associated non-MORB type basalts (i.e., mid-ocean ridge-type basalts).

Four lithologic units were identified at Site 899.

1. Unit I (81.50-131.65 mbsf) is a Pliocene silty clay to clayey silt, nannofossil clay with clay, silt, and fine sand with minor nannofossil ooze. The unit consists mainly of terrigenous turbidites.
2. Subunit IIA (131.65-206.6 mbsf) is an early Pliocene to middle Miocene bioturbated nannofossil claystone and claystone with minor silty claystone. The subunit consists mainly of pelagic/hemipelagic sediments with scattered turbidites.

Subunit IIB (206.6-228.6 mbsf in Hole 899A, 230.5-360.2 mbsf in Hole 899B) is a Miocene to Oligocene bioturbated silty claystone to clayey siltstone with calcareous claystone and minor claystone, siltstone, and sandstone. The subunit was probably deposited above the carbonate compensation depth (CCD) by contour currents reworking turbidites.

3. Subunit IIIA (360.6-364.66 mbsf in Hole 899B) is a late Eocene age claystone deposited below the CCD.

Subunit IIIB (364.6-369.9 mbsf in Hole 899B) is a Late Cretaceous age sandy silty claystone with clayey conglomerate and clayey sandstone. It was deposited by a combination of hemipelagic and pelagic settling and by high-density turbidites or sand-silt-clay debris flows.

4. Subunit IVA (369.9-484.2 mbsf in Hole 899B) contains three Campanian to early Maastrichtian serpentinite breccia units, one up to

[1] Sawyer, D.S., Whitmarsh, R.B., Klaus, A., et al., 1994. *Proc. ODP, Init. Repts.,* 149: College Station, TX (Ocean Drilling Program).
[2] Shipboard Scientific Party is as given in list of participants preceding the contents.

95 m thick, and two less than 20 m thick with minor calcareous claystone and claystone.

Subunit IVB (484.2-549.9 mbsf in Hole 899B) was poorly recovered, but includes serpentinite, basalt, gabbro, and claystone, and minor siltstone, of early Aptian to Barremian age.

The most unusual aspect of the sequence of rocks recovered is Unit IV. It consists of three lithologies. These are (1) serpentinite breccias units, up to 95 m thick; (2) unbrecciated serpentinized peridotite and gabbro; and (3) intercalated claystone, unconsolidated altered serpentinite, and minor siltstone associated with basalt fragments as individual pieces in the cores or as clasts within the sediment. The clasts in the breccia units are up to 1 m thick. At least 90% of these clasts are serpentinized peridotite, many of which display a fabric indicative of moderate-temperature/high-pressure ductile deformation, and the remainder are fragments of metamorphosed magnesium-rich igneous rock. These breccia units are largely structureless and unsorted. Rarely, flow structures and the sediment/breccia contact are seen near the bases of the breccia units. The matrix has a texture that, in a tectonic setting, indicates shear deformation under low normal stress that typically results from high fluid pressures. Clasts of continental basement rocks and sediment are entirely absent, but clasts possibly composed of basalt and microgabbro are present. Below the breccia units, Subunit IVB is principally unbrecciated boulder-sized blocks of serpentinite, but also contains intercalated siltstones and claystones and intercalated clasts of basalt, microgabbro, and chlorite-bearing mylonite. This subunit is interpreted as a series of mass flow deposits. Both subunits contain intercalated Early Cretaceous age sediments exhibiting a normal stratigraphic sequence that gets younger uphole.

The cores at Site 899 provide a discontinuous fossil record from the late Pliocene through Late Cretaceous. Calcareous nannofossils generally are present, but sometimes are rare in the Cretaceous section. Planktonic foraminifers are abundant to common in the late Pliocene to late early Miocene age deposits, but are less common or absent below. A hiatus representing at least 2.9 m.y. lasted from middle Miocene to late Miocene time. A major hiatus representing most of the Paleogene lies within Core 149-899B-15R. The presence of the Early Cretaceous age nannoflora is especially important for providing a tentative stratigraphy for the serpentinite breccias.

Acoustic formations 1Aand 1B are widely recognized in multichannel seismic reflection profiles on the western Iberia margin and have been locally dated by previous drilling. At Site 899, acoustic formation boundary 1A/1B correlates with the middle/late Miocene hiatus at 170 mbsf.

A few potential paleomagnetic reversals were observed in the sedimentary section. Sediment natural remanent magnetization (NRM) intensities range from 0.1 to 1.0 mA/m. Within Unit IV, the serpentinite breccias have a very stable normal magnetization that may correspond to a period within the Cretaceous Long Normal Superchron. Between 470 and 520 mbsf, a possible pattern of reversals was observed. Magnetic susceptibility was moderately high in Unit I (3×10^{-4} SI units), low in Subunit IIB (about 1×10^{-4} SI units), and very high within Unit IV (about 1×10^{-2} SI units).

Physical property measurements in the sediments show a small, but steady, increase in bulk density, seismic velocity, formation factor, shear strength, and thermal conductivity, and a concomitant decrease in porosity with depth. Within the acoustic basement, the altered ultramafic rocks have higher densities, but relatively low grain densities (both about 2.5 g/cm^3). Electrical resistivity is particularly high in parts of the serpentinite breccia (up to 800 Ωm), as are seismic velocity (4.2-6.9 km/s), and thermal conductivity (1.4-2.5 W/m·K).

Downhole logs were obtained from part of the thick serpentinite breccia unit in the top of Subunit IVA (395-430 mbsf). These showed a low natural gamma-ray count (5-10 API units), low aluminum content (1-1.5 wt%), a high resistivity (mean 150 and maximum 1000 Ωm), low porosity (0%-10%) and compressional and shear wave velocities of 3.81 to 4.85 and about 2.3 km/s, respectively. Local higher velocities, resistivities, and densities appear to correlate with blocks of serpentinized peridotite. Core index and log bulk densities agree within ± 0.05 g/cm^3.

Interstitial-water samples were obtained from within Unit I through Subunit IIB (81.5-350 mbsf). The sulfate concentration is almost constant (18.5-19.9 mM) in most of the hole, with a steady decrease within the lower half of lithostratigraphic Subunit IIB to a minimum of 15.5 mM. Sulfate is depleted with respect to seawater, indicating that sulfate reduction has probably occurred in the unsampled section from 0 to 81.5 mbsf. Profiles of carbonate content vs. depth reflect a history of generally low biological productivity, and deposition of hemipelagic sediment below the CCD, combined with delivery by turbidites of carbonate-rich material that had initially been deposited above the CCD. Unit I contains 0.3% organic carbon, which is much less than that at Sites 897 and 898. Organic C/N ratios from Unit I and the upper part of Subunit IIB are variable; a few values are anomalously low. Concentrations of biogenic methane encountered in headspace gas analyses of lithostratigraphic Unit I through Subunit IIIB generally are low. Methanogenesis may have been inhibited by the generally high sulfate concentrations.

BACKGROUND AND SCIENTIFIC OBJECTIVES

Site 899 (Fig. 1 in "Site 897" chapter, this volume) was one of a series of sites drilled during Leg 149 to elucidate the nature of the top of the crust (acoustic basement) within the ocean/continent transition (OCT) beneath the Iberia Abyssal Plain. The regional background to this and the other Leg 149 sites is presented elsewhere (see "Introduction" chapter, this volume; Whitmarsh, Miles, and Mauffret, 1990; Whitmarsh, Pinheiro, et al., 1993). Site 899, an alternative site to Site 898, was chosen at sea when the loss of drill pipe prevented us from coring an adequate section of basement at Site 898. Site 899 was located 8.5 nmi (15.7 km) northwest of Site 898 and 10 nmi (18.5 km) east-southeast of Site 897 (see "Site Geophysics" section, this chapter). Site 899 was chosen to sample a basement high located between the thin oceanic crust to the west and the weakly magnetized, thinned continental crust to the east (see Fig. 4 in "Introduction" chapter, this volume). The site is located within an intermediate zone of high magnetization and smooth acoustic basement (between the basement highs) that is located between the latter two crustal types. The basement high under the site is roughly circular in plan view with a steep southern slope, and its shape contrasts strongly with the linear north-south basement ridges and valleys at, and west of, Site 897 (Fig. 2 in "Site 897" chapter, this volume). The basement high is not well imaged on the two *JOIDES Resolution* single-channel seismic profiles that cross it, but appears to have a broad rounded top with two subsidiary peaks (Figs. 1 and 2). We expected the high to be a fault block consisting of thinned continental crust. Although the discovery of this site was fortuitous, its location even nearer than Site 898 to Site 897 was seen as advantageous for potentially allowing the OCT to be defined even more closely than it would have been had only Site 898 been drilled to basement.

A hyperbolic acoustic reflection peaking at 0.5 s two-way traveltime (about 470 mbsf) on the single-channel seismic reflection profiles across the site was conservatively chosen as acoustic basement. A shallower hyperbola peaks at 0.4 s two-way traveltime (about 370 mbsf). By analogy with Site 398, 110 km east of Site 898, we expected to encounter ooze/chalk with turbidites over chalk, mudstone, and claystone (Sibuet, Ryan, et al., 1979). Seismic reflection profiles traced back to Site 398 indicated that the basal sediments would be as old as late Eocene/early Oligocene. A regional unconformity, which resulted from gentle folding during the northwest-southeast Rif-Betic compressional phase in southern Spain and North Africa and which is visible clearly on seismic reflection profiles from the Iberia Abyssal Plain, was expected to occur at about 190 mbsf. In the vicinity of Site 899, the unconformity is marked by horizontal sedimentary reflectors that onlap low-angle west-dipping reflectors (Fig. 1). These sediments thicken to at least 1.7 s two-way traveltime (1.9 km) in the basin underlain by the smooth basement west of the site and to at least 1.5 s two-way traveltime (1.6 km) to the east. Although we anticipated that acoustic basement at Site 899 might contain continental rocks, the exact petrology of these rocks and the amount of any synrift igneous material was completely unknown.

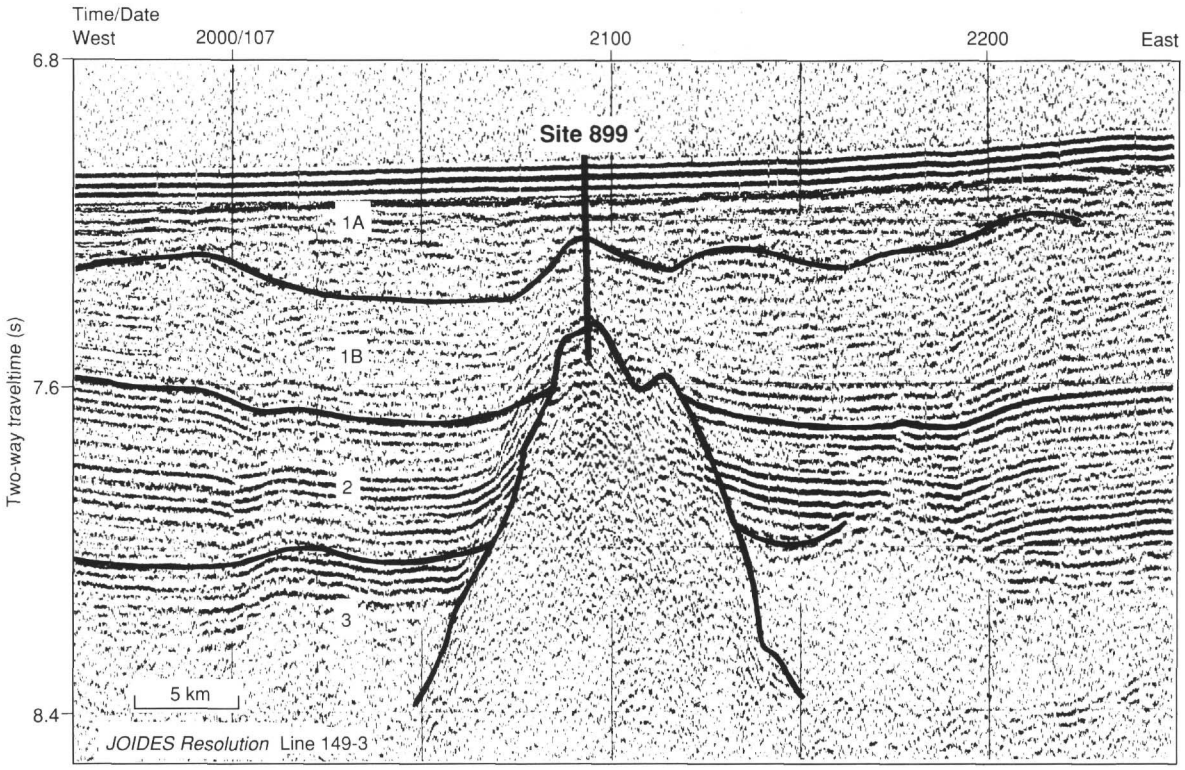

Figure 1. East-west single-channel seismic reflection profile across Site 899 (See Fig. 3 for location). Thick vertical line indicates the penetration of the borehole. The enhanced lines on the section indicate the boundaries between acoustic formations 1A, 1B, 2, and 3, defined by Groupe Galice (1979) (see "Integration of Seismic Profiles with Observations from the Site" section, this chapter). The angular unconformity between acoustic formations 1A and 1B is described in the text. Vertical exaggeration is about 10:1.

OPERATIONS

Hole 899A

After completing drilling at Site 898, the ship was moved 8 nmi (15.7 km) northwest to Site 899. We deployed a Datasonics beacon at 40°46.34'N, 12°16.07'W. This location had been confirmed during the geophysical survey prior to the mid-leg Lisbon port call (end of Leg 149B). After the ship was stabilized in dynamic positioning mode over the primary beacon, a second backup Datasonics beacon was deployed.

A rotary core barrel (RCB) bottom-hole assembly (BHA) was assembled and run to the seafloor. The vibration-isolated television (VIT) was lowered, and the seafloor was observed at 5302.5 mbrf. A jet-in test was conducted from the seafloor to 5366.5 mbrf (0.0-64.0 mbsf), beyond which depth we were unable to penetrate. We then drilled from 5366.5 to 5384.0 mbrf (64.0-81.5 mbsf). Cores 149-899A-1R to -16R were taken from 5384.0 to 5538.0 mbrf (81.5-235.5 mbsf; Table 1). Well-compacted clay was cored at 5512.5 mbrf (210 mbsf); we stopped coring at 5538.0 mbrf (235.5 mbsf) to set a reentry cone, 49.6 m of 16-in. casing, and 216 m of 11.75-in. casing.

Hole 899B

The ship was moved 20 m north to 40°46.347'N, 12°16.063'W. We assembled three joints of 16-in. casing (49.62 m) with a three-cone drill bit inside the casing about 0.15 m above the shoe and attached it to a reentry cone. The reentry cone and casing were run to the seafloor, where the casing was jetted-in to 5352.1 mbrf (49.6 mbsf), placing the reentry cone on the seafloor. The drill bit was disconnected from the casing, and we drilled to 5529.5 mbrf (227.0 mbsf). The hole was filled with a mixture of sepiolite clay and seawater, and we pulled out of the hole.

We assembled 216 m of 11-3/4-in. casing and lowered it to 5518.9 mbrf (216.4 mbsf). The casing was cemented in place. After pulling out of the hole, we assembled an RCB-BHA having a chisel point center bit and mechanical bit release (MBR) and lowered it to the seafloor. We reentered the hole, encountered cement at 5508.0 mbrf (205.5 mbsf) and drilled through the cement and the 11-3/4-in. casing shoe. A 4.5-m section of new hole was drilled to 5533.0 mbrf (230.5 mbsf) to break down completely pieces of the shoe.

Cores 149-899B-1R to -37R were taken from 5533.0 to 5865.0 mbrf (230.5-562.5 mbsf), with 332.0 m cored and 173.41 m recovered (Table 1). Hard rock (acoustic basement) was encountered at 369.8 mbsf. Below Core 149-899B-26R (464.2 mbsf), recovery decreased (to less than 20%) and hole conditions deteriorated. We discontinued coring at 557.6 mbsf because of high torque, overpull, and continuous sloughing of material into the bottom of the hole.

The hole was reamed from 5764.0 to 5860.1 mbrf, and Core 149-899B-37R was taken from 5860.1 to 5865.0 mbrf (557.6-562.5 mbsf), with 4.9 m cored and 0.19 m recovered. Hole conditions remained poor, and we again attempted to ream and wash the hole from 5505.0 to 5865.0 mbrf (202.5-562.5 mbsf). We encountered several bridges that had to be drilled through (a wash barrel was recovered from this section). Finally, the pipe became stuck at 5852.0 mbrf (549.5 mbsf) and after pulling free with difficulty, we decided to terminate coring at Site 899B.

The original plan for logging at Hole 899B was to drop the bit on the seafloor. Because of the unstable hole conditions, the importance of logging the peridotite basement, the risk of the hole collapsing should the drill string be pulled out of the hole to drop the bit, and the

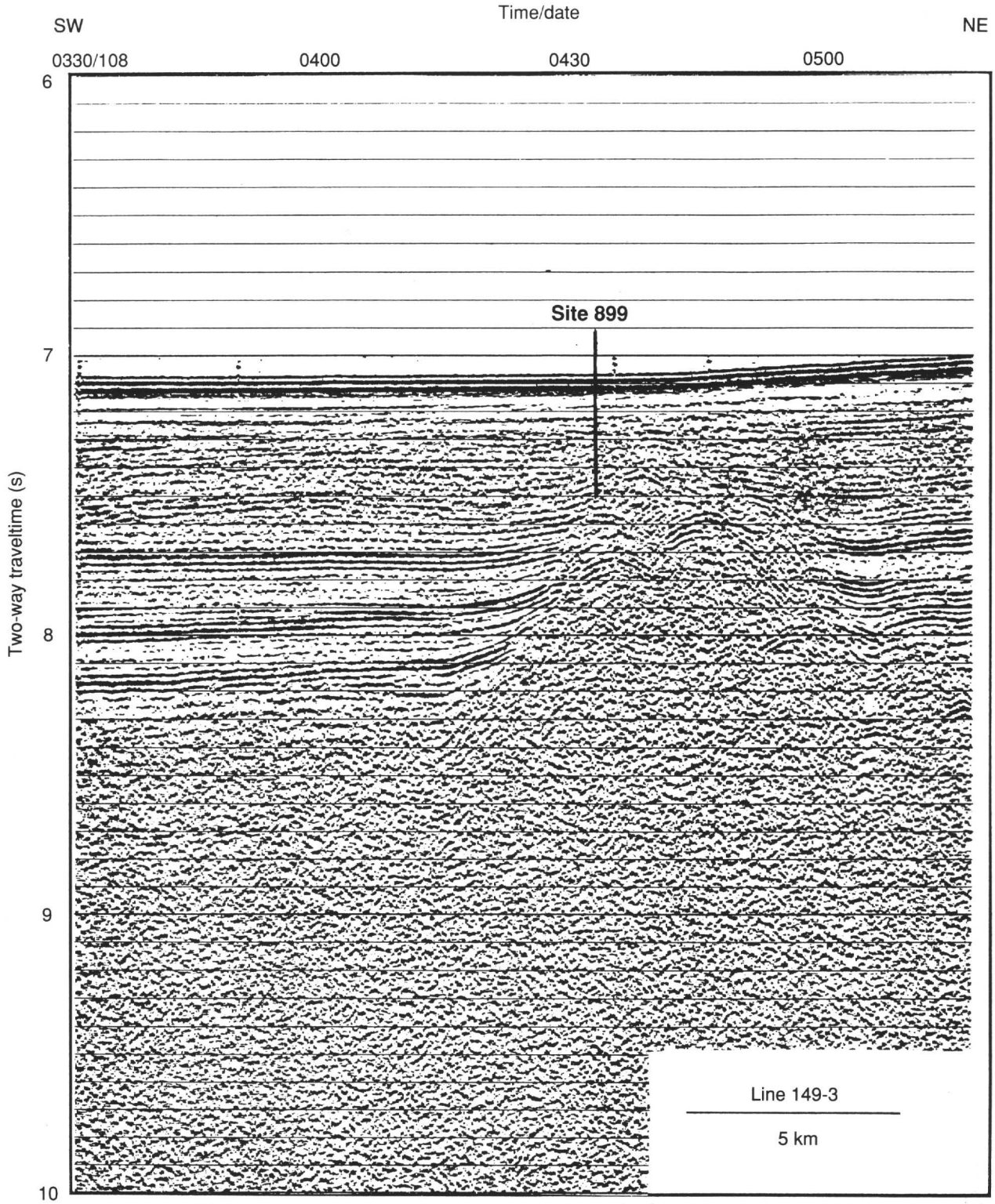

Figure 2. Single-channel seismic profile *JOIDES Resolution* 149-3 (southwest-northeast portion) near Site 899. The location of this profile is shown in Figure 3. The projected location of Site 899 is indicated by the vertical line. Vertical exaggeration is about 13:1.

probability that an open-ended drill string could not be worked back down below the top of basement to obtain logs in the basement, we decided to release the bit in the hole.

The bit was released using the MBR at 5841.6 mbrf (539.1 mbsf). The open drill string was pulled to 5696.3 mbrf (393.8 mbsf), which was just below the top of the peridotite breccia at 369.8 mbsf (for details of the logging operations see "Downhole Logging" section, this chapter). The first two logging runs (Run 1 = dual induction tool [DIT], caliper tool [MCD], dipole shear imager [DSI], natural gamma-ray spectrometry tool [NGT-C], and the Lamont temperature logging tool [TLT]; Run 2 = slim-hole lithodensity logging tool [HLDT], dual porosity compensated neutron tool [CNT-G], sonic

Table 1. Coring summary for Site 899.

Core	Date (1993)	Time (UTC)	Depth (mbsf)	Length cored (m)	Length recovered (m)	Recovery (%)
149-899A						
1R	Apr 27	1540	81.5–91.1	9.6	4.75	49.5
2R	Apr 27	1655	91.1–100.8	9.7	2.84	29.3
3R	Apr 27	1810	100.8–110.4	9.6	4.67	48.6
4R	Apr 27	1925	110.4–120.1	9.7	3.14	32.4
5R	Apr 27	2040	120.1–129.7	9.6	4.33	45.1
6R	Apr 27	2155	129.7–139.0	9.3	5.27	56.6
7R	Apr 27	2335	139.0–148.7	9.7	1.03	10.6
8R	Apr 28	0105	148.7–158.3	9.6	2.97	30.9
9R	Apr 28	0230	158.3–168.0	9.7	4.45	45.9
10R	Apr 28	0350	168.0–177.6	9.6	0.88	9.2
11R	Apr 28	0520	177.6–187.3	9.7	2.20	22.7
12R	Apr 28	0645	187.3–197.0	9.7	0.00	0.0
13R	Apr 28	0815	197.0–206.6	9.6	0.10	1.0
14R	Apr 28	0935	206.6–216.3	9.7	4.47	46.1
15R	Apr 28	1050	216.3–225.9	9.6	7.65	79.7
16R	Apr 28	1225	225.9–235.5	9.6	2.70	28.1
Coring totals				154.0	51.45	33.4
			Drilled 0–230.5 mbsf			
149-899B-						
1R	May 3	0830	230.5–234.8	4.3	3.87	90.0
2R	May 3	0955	234.8–244.4	9.6	4.53	47.2
3R	May 3	1120	244.4–254.0	9.6	9.26	96.4
4R	May 3	1250	254.0–263.7	9.7	7.95	81.9
5R	May 3	1415	263.7–273.4	9.7	8.42	86.8
6R	May 3	1545	273.4–283.0	9.6	8.13	84.7
7R	May 3	1715	283.0–292.6	9.6	9.71	101.0
8R	May 3	1900	292.6–302.3	9.7	9.79	101.0
9R	May 3	2040	302.3–312.0	9.7	8.34	86.0
10R	May 3	2220	312.0–321.6	9.6	7.88	82.1
11R	May 4	0025	321.6–331.2	9.6	6.71	69.9
12R	May 4	0245	331.2–340.9	9.7	7.69	79.3
13R	May 4	0530	340.9–350.6	9.7	8.88	91.5
14R	May 4	0800	350.6–360.2	9.6	7.80	81.2
15R	May 4	1030	360.2–369.8	9.6	7.21	75.1
16R	May 4	1310	369.8–379.4	9.6	4.03	42.0
17R	May 4	1850	379.4–389.1	9.7	3.88	40.0
18R	May 4	2340	389.1–398.3	9.2	5.98	65.0
19R	May 5	0305	398.3–407.7	9.4	5.15	54.8
20R	May 5	0745	407.7–417.1	9.4	4.72	50.2
21R	May 5	1220	417.1–426.3	9.2	6.11	66.4
22R	May 5	1600	426.3–435.6	9.3	2.31	24.8
23R	May 6	0055	435.6–445.3	9.7	4.32	44.5
24R	May 6	0440	445.3–454.7	9.4	3.91	41.6
25R	May 6	0830	454.7–464.2	9.5	3.14	33.0
26R	May 6	1145	464.2–473.6	9.4	1.58	16.8
27R	May 6	1430	473.6–482.9	9.3	1.94	20.8
28R	May 6	1940	482.9–492.1	9.2	1.42	15.4
29R	May 7	0005	492.1–501.3	9.2	1.50	16.3
30R	May 7	0445	501.3–510.5	9.2	2.26	24.5
31R	May 7	1010	510.5–520.0	9.5	1.71	18.0
32R	May 7	1250	520.0–529.5	9.5	0.50	5.3
33R	May 7	1545	529.5–538.9	9.4	0.50	5.3
34R	May 7	1905	538.9–548.4	9.5	0.80	8.4
35R	May 7	2315	548.4–557.6	9.2	1.29	14.0
36W	May 8	0515	557.6–557.6	0.0	0.57	(wash core)
37R	May 8	0800	557.6–562.5	4.9	0.19	3.9
Coring totals				332.0	173.41	52.2
Drilled totals				230.5	0.00	
Washed totals				0.0	0.57	
Combined totals				562.5	173.98	

digital logging tool [SDTC], NGT-C, and TLT) were successfully run to 5757.0 mbrf (454.5 mbsf) and 5747.0 mbrf (444.5 mbsf), respectively. The neutron source of the induced gamma-ray spectrometry tool (GST-A) malfunctioned during our initial attempt at the third logging run (GST-A, aluminum activation clay tool [ACTC], CNT-G, NGT-C, and TLT). We replaced the GST-A source and the logging run was made. Although the neutron source failed again, we continued logging with the remaining tools in this combination to 5737.0 mbrf (434.5 mbsf). During this run, sediment had accumulated in the bottom of the hole, which decreased the amount of section that was possible to log; thus, we decided to discontinue logging this interval. The drill string then was pulled up to 5496.5 mbrf (194 mbsf), inside the casing, and we made a fourth logging run with the Formation Microscanner/NGT-C/TLT combination tool. This tool was unable to penetrate more than 4 m below the end of the casing, and logging was terminated. The drill pipe was pulled out of the hole, and the two beacons recalled and recovered.

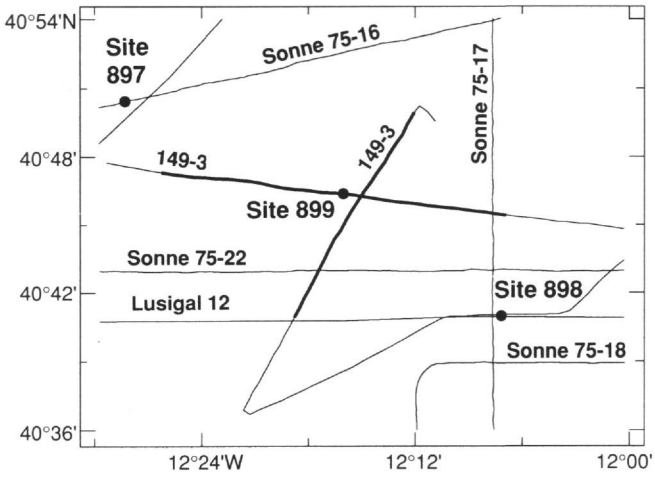

Figure 3. Multichannel seismic data and *JOIDES Resolution* Line 149-3 track chart near Site 899. The bold lines indicate the east-west and southwest-north east parts of Line 149-3, shown in Figures 1 and 2, respectively.

SITE GEOPHYSICS

Geophysical Data near Site 899

Seismic-reflection data from the two intersecting portions of *JOIDES Resolution* single-channel seismic-reflection profile 149-3 (Figs. 1 through 3) shows that the basement high on which Site 899 is located is a roughly circular feature having a diameter about 4 km at its top and 8 km at its base. It rises about 750 m above the basement in the adjacent basins. The top of the high is not clearly imaged in the unmigrated seismic profile. Two or three diffractions off the top of the high suggest that it has two or three local peaks. The depth to basement at the site is not clear. The shallowest diffraction is at about 370 mbsf, but this may be basement or may have been caused by a fault in the overlying sediment, similar to one seen in seismic-reflection data across Site 898 (Fig. 1 in "Site 898" chapter, this volume). A stronger diffraction at about 490 mbsf seems more certain to be the top of basement or to be within basement. The Miocene unconformity, perhaps as shallow as 120 mbsf at Site 899 and to the north and east of the site, deepens toward the south and west. By analogy to Site 897, where we drilled the deepest reflector that covers basement at Site 899, we expected that the oldest regionally extensive sediments would be Eocene in age. The deeper reflectors onlap the basement high at about the same depth on each side of the high.

Magnetic data (Fig. 7 in "Site 897" chapter, this volume; P.R. Miles, J. Verhoef, and R. MacNab, pers. comm., 1993) show that Site 899 is located on the northwest side of the same magnetic anomaly high on which Site 898 is located. The magnetic high is only slightly elongated in the north northwest-south southeast direction and is not aligned parallel to the margin, as are most of the magnetic anomalies farther to the west. Beslier et al. (1993) and Whitmarsh, Miles, and Mauffret (1990) interpreted seismic profiles and magnetic data, respectively, to indicate that Site 899 is located near the oceanward edge of extended continental crust.

LITHOSTRATIGRAPHY AND PETROLOGY

Introduction

Drilling at Holes 899A and 899B penetrated a 562.5-m-thick succession in which four lithostratigraphic units were recognized (Fig. 4; Table 2). Units I and II are similar to those encountered at Sites 897

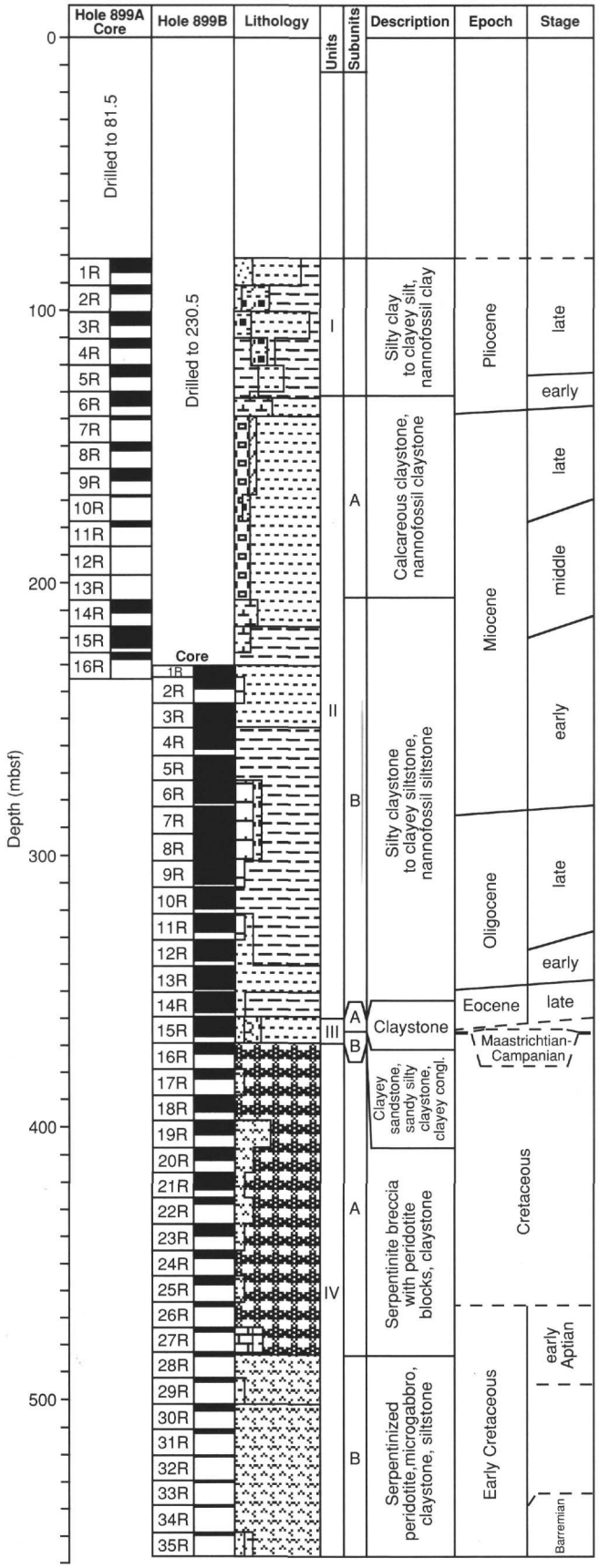

Figure 4. Master column for Site 899.

and 898, and Unit III is broadly comparable to Unit III at Site 897. However, Unit IV at Site 899, although consisting of a mixture of serpentinized peridotite and Early Cretaceous sediments, contains a distinctive upper breccia subunit that is not well-developed in Unit IV at Site 897.

Subsequent drilling at Site 900 suggested the regional stratigraphic correlation shown in Figure 5. At Sites 897 through 900 the gross lithostratigraphy consists of a lower carbonate-rich contourite-turbidite-pelagite sequence and an upper turbidite-pelagite sequence. The two sequences contrast sharply in terms of evidence for reworking by contour currents (which is present only in the lower sequence) and in the abundance of siliceous allochems (which are virtually absent in the upper sequence).

The ages, averaged lithologic compositions, overall colors, facies and depositional environments, boundary depths, and cored intervals of Units I through IV are summarized in Table 2; Tables 3 and 4 show the color variations exhibited by the lithologies in Units I and II and Unit III, respectively.

Rotary coring (RCB) was employed in both holes. Hole 899A was washed down to 81.5 mbsf, where drilling commenced in Unit I and terminated at 235.5 mbsf in Subunit IIB. Coring in Hole 899B started at 230.5 mbsf in Subunit IIB and terminated at 562.5 mbsf in Unit IV.

Unit I contains greenish gray siliciclastic turbidites capped by light gray nannofossil-rich hemipelagic/pelagic sediments. Subunit IIA consists of intensely bioturbated hemipelagic/pelagic brown clay stone and nannofossil claystone with scattered turbidites. Subunit IIB, dominated by greenish-gray upward-darkening sequences of nannofossil silty claystone and clayey siltstone, is interpreted as turbiditic sediments reworked by contour currents. Unit III (9.3 m thick) comprises an upper Subunit IIIA of brown claystone and organic-rich black concretions and a lower subunit (IIIB) of sandy silty claystone, yellow sandstone and dark reddish brown clayey conglomerate. The clayey conglomerate may represent a layer of highly weathered material that was derived from the immediately underlying serpentinite breccia.

Unit IV contains serpentinite breccias and blocks intercalated with early Aptian to Barremian sediments. Subunit IVA consists of an unusual serpentinite breccia intercalated with calcareous claystone, claystone, and basalt pieces. Subunit IVB consists of similar sedimentary lithologies interbedded with discrete unbrecciated sections of serpentinite, serpentinized peridotite, and gabbros.

Figure 6 is a plot of ages-vs.-depths (see Table 5) for the sedimentary sequence penetrated at Site 899. Sediment accumulation rates, generalized from Figure 6, vary less than rates observed for the corresponding lithostratigraphic units at Sites 897 and 898: Unit I, 35 m/m.y.; Unit II, 10 m/m.y. Currently available biostratigraphic information does not permit one to evaluate sediment accumulation rates for Units III and IV.

Unit I

Cores 149-899A-1R through -6R-2, 45 cm
Depth: 81.5-131.65 mbsf
Age: late to early Pliocene

General Description

In Hole 899A, 21.68 m of Unit I was recovered, which represents an average recovery of 43.6%. The unit consists of turbidites and associated pelagic/hemipelagic sediments. The turbidites exhibit classical Bouma sequences (Bouma, 1962), and range in thickness from about 5 (e.g., Section 149-899A-5R-1) to 150 (e.g., Section 149-899A-3R-1) cm; these turbidites are comparable to those described in Unit I at Sites 897 and 898.

Core disturbance in Unit I is moderate to soupy. In the first three cores, sediment flow-in resulted from the mobilization of the thick (>20 cm), water-saturated, fine- to medium-grained, basal sand layers of the turbidites. Sedimentary structures in these layers are destroyed or disrupted.

Table 2. Summary of lithostratigraphic Units I through IV at Site 899.

Unit	Age	Thickness (m)	Lithology	Percentage (%)[a]	Color	Facies and *environment* (total meters described)	Intervals (mbsf) 899A	Intervals (mbsf) 899B	Occurrence 899A	Occurrence 899B
I	Pliocene	50.15A	Nannofossil ooze Nannofossil clay Clay Silty clay to clayey silt Silt and fine sand	6 25 17 36 16	Greens and grays	Terrigenous turbidites *Abyssal plain* [21.7]	Shallowest = 81.50 Base = 131.65 Top not observed		1R-1 at 0 cm 6R-2 at 45 cm	
IIA	early Pliocene to middle Miocene	74.95A	Nannofossil clay Clay Nannofossil ooze Silty clay Silt and sand	67 20 1 8 4	Browns	Hemipelagic/pelagic deposits and minor turbidites *Abyssal plain, above CCD* [13.77]	Top = 131.65 Base = 206.6		6R-2 at 45 cm 13R-CC	
IIB	middle Miocene to late Eocene	(22A)[b] 136.1B	Calcareous claystone Claystone Silty clayst. to clayey siltst. Siltstone and sandstone	27 2 68 3	Gray/ green/ brown	Calcareous turbidites reworked by contour currents *Abyssal plain, above CCD* [124.17]	Top = 206.6 Base = 228.6	Top = 230.5 Base = 360.6	14R-1 at 0 cm 16R-CC	1R-1at 0 cm 15R-1 at 42 cm
IIIA	late Eocene	4.0B	Claystone	100	Brown	Pelagic/hemipelagic *Abyssal plain, below CCD* [3.77]		Top = 360.6 Base = 364.6		15R-1 at 42 cm 15R-3 at 141 cm
IIIB	Late Cretaceous	5.3B	Clayey conglomerate Clayey sandstone Sandy silty claystone	30 10 60	Variegated	High-density turbidity flow and debris flow [2.7]		Top = 364.6 Base = 369.9		5R-3 at 141 cm 16R-1 at 7 cm
IVA	pre-Late Cretaceous to early Aptian	114.3B	Serpentinite breccia Calcareous claystone Claystone Basalt clasts	90 5 5 <1	Variegated	[45.27]		Top = 369.9 Base = 484.2		16R-1 at 7 cm 28R-1 at 128 cm
IVB	early Aptian to Barremian	73.72B	Serpentinite Gabbro Siltstone Claystone	60 20 5 15	Variegated	[8.95]		Top = 484.2 Deepest = 557.92 Base not observed		28R-1 at 128 cm 37R-1 at 32 cm

[a] Visual estimates only for Units III and IV.
[b] ( ) Indicates partial penetration of subunit.

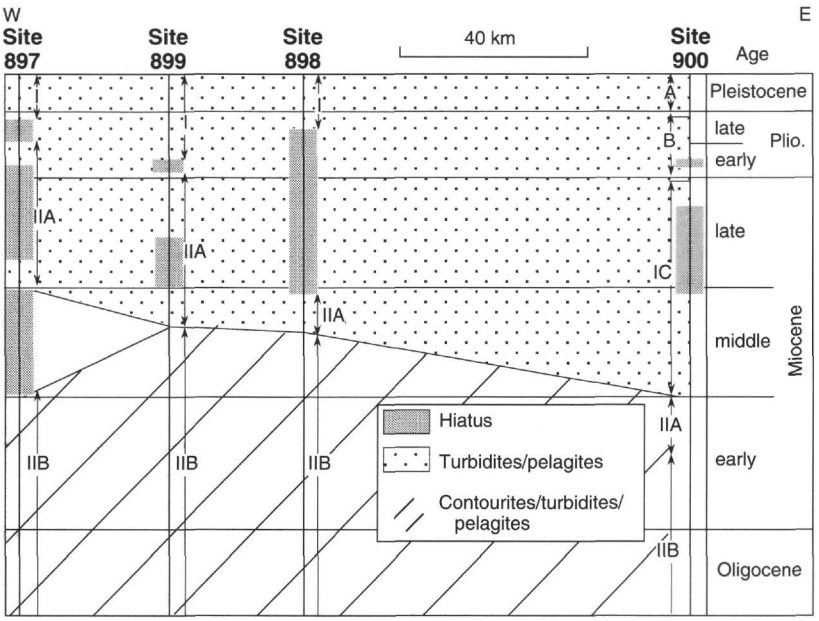

Figure 5. Regional stratigraphic correlation chart for Sites 897 to 900. The lower contourite-turbidite-pelagite sequence contains abundant siliceous allochems and reworked carbonate grains. The upper turbidite-pelagite sequence shows no evidence of reworking by contour currents.

Table 3. Color variations of lithologies in Units I and II.

Color	Munsell code	Sand/ sandstone	Silty sand/ stone	Sandy silt/ stone; siltstone	Clayey silt/stone; silty clay/ stone	Clay/stone	Calc./ nanno. clay/ stone or silty clayst.	Nannofossil clay clay/stone	Nannofossil ooze/chalk
Dark gray	N4								
Medium gray	N5			■					
Medium light gray	N6								
Light gray	N7	o							
Very lightgray	N8	o							
White	N9								
Dark yellowish brown	10YR 4/2				o	o	+ ■		
Mod. yellowish brown	10YR 5/4							+	
Yellowish brown	10YR 5/2						+	+	
Pale yellowish brown	10YR 6/2								+
Very pale orange	10YR 8/2								
Reddish orange	5YR 4/2						■		
Medium brown	5YR 4/4						■		
Brownish gray	5YR 4/1						■		
Olive black	5Y 2/1				o	o			
Olive gray	5Y 4/1	o	o	o ■	o	■		o ■	+ ■
Light olive gray	5Y 5/1,5/2	+			o ■	o		■	+
Light olive gray	5Y 6/1	■				■	o +	o + ■	+
Yellowish gray	5Y 8/1	o						o +	+
Grayish green	10GY 5/2								
Greenish black	5GY 2/1								
Dark greenish gray	5GY 4/1	o	o		■				
Greenish gray	5GY 5/1				■		■		
Greenish gray	5GY 6/1	■			■			■	
Light greenish gray	5GY 8/1							+ ■	
Greenish black	5G 2/1,2/2					■			
Dark greenish gray	5G 4/1					■			
Greenish gray	5G 6/1,7/1		+	■	■		■		

Note: Unit I = o; Subunit IIA = +; Subunit IIB = ■.

Sediment color ranges from olive black to light gray and light olive gray, with lighter-colored sediments containing a higher carbonate content (Table 3). Medium thickness color-banding of olive gray and light olive gray occurs in Section 149-899A-5R-2. Major lithologies are olive gray silty clay, which changes below Core 149-899A-5R to dark yellowish brown, and very light gray to white calcareous clay to nannofossil ooze. Minor lithologies include greenish black and olive gray sand to silty sand and dark greenish gray to very light gray foraminifer-rich sand (e.g., Sections 149-899A-5R-1, -5R-2, -5R-3). Interbedded silt laminae in silty clay are present in Section 149-899A-4R-2.

The turbidite sequences in Unit I consist of a basal sandy silt to silty sand layer that passes upward into silty clay that has been overlain by nannofossil clay. The sand layers decrease in thickness from about 30 cm in Core 149-899A-1R to 3 to 5 cm in Cores 149-899A-4R to -6R. Lamination and cross-lamination occur in a few of the sands. Bioturbation commonly mixes the light gray pelagic calcareous clay and nannofossil ooze into the underlying darker green silty clay; no distinct ichnofauna is visible. Thin reddish purple (5RP 2/2) bands, which cross-cut bedding, are visible in Sections 149-899A-3R-1, -4R-1, and -6R-1.

Petrography

Applying the classification of Folk (1980), sands and silts of Unit I are subarkoses, arkoses, and lithic arkoses. Grain types in Unit I

Table 4. Color variation of lithologies in Unit III.

Color	Munsell code	Silty sand/stone sandstone	Siltstone	Silty claystone	Claystone	Concretion	Conglomerate
Light gray	N7				o		o
Mod. reddish orange	10R 2/2						o
Very dusky red	10R 6/6						o
Dark yellowish brown	10YR 4/2				▲		
Mod. yellowish brown	10YR 5/4	o			▲		
Yellowish brown	10YR 5/2				▲		
Pale yellowish brown	10YR 6/2				▲		
Grayish orange	10YR 7/4		▲				
Mod. orange pink	5YR 8/4			o			
Moderate brown	5YR 4/4				o ▲		
Light brown	5YR 5/6	o		o	▲		
Pale brown	5YR 5/2				o		
Brownish black	5YR 2/1					▲	
Mod. greenish yellow	10Y 7/4						o
Light olive gray	5Y 5/2				o		
Light olive brown	5Y 5/6			▲			
Dusky yellow	5Y 6/4	o			o		
Yellowish gray	5Y 7/2	o			o		
Greenish gray	5G 6/1				o ▲		

Note: Subunit IIIA = ▲ ; Subunit IIIB = o.

Table 5. Biostratigraphic data used to constrain sediment accumulation rates for Site 899.

Code	Datum	Age and range (Ma)	Depth range (mbsf)
1	T. *Reticulofenestra pseudoumbilica*	3.56	123.49–124.43
2	T. *Discoaster quinqueramus*	5.38	134.97–139.52
3	B. *Amaurolithus delicatus*	7.01	151.67–162.01
4	Base NN11 (T. *Discoaster loblichii*)	8.28	162.01–162.75
5	B. *Discoaster kugleri*	12.20	179.80–197.08
6	B. *Triquetrorhabdulus rugosus*	12.50	197.08–197.10
7	T. *Sphenolithus heteromorphus*	13.37	197.10–206.78
8	TA. *Discoaster deflandrei*	16.05	211.07–220.55
9	T. *Sphenolithus belemnos*	18.80	233.51–233.86
10	T. *Triquetrorhabdulus carinatus*	20.00	233.86–248.93
11	Base NN1 (T. common *S. ciperoensis*)	24.70	281.53–285.29
12	T. *Sphenolithus distentus*	27.60	310.64–312.83
13	B. *Sphenolithus ciperoensis*	29.40	327.45–334.11
14	T. *Discoaster barbadiensis*	35.60	346.02–349.70
15	Late Cretaceous (Maastrichtian?)	65.00–70.00	364.67
16	late early Aptian	118.00–120.00	465.05
17	early early Aptian	122.00–125.00	492.31
18	Barremian	125.00–128.00	549.56

Note: T. = top; B. = bottom; TA. = top acme.

indicate derivation from a source area that exposed mostly sedimentary, metamorphic, and, possibly, granitic rocks. The detailed petrography of the sediments in Unit I is identical to that described for Site 898 (see "Site 898" chapter, "Lithostratigraphy" section, this volume).

Depositional Processes

The depositional setting and processes for Unit I are similar to those interpreted for the same unit at Site 897. Turbidity current deposition periodically interrupted pelagic sedimentation.

Unit II

Cores 149-899A-6R-2, 45 cm, to 149-899B-15R-1, 42 cm
Depth: 131.65-360.6 mbsf
Age: early Pliocene to late Eocene

General Description

The major lithologies in Unit II are silty clay/claystone with silt and nannofossil clay/claystone (Table 2). Minor lithologies include clay/claystone, siltstone, clayey silty sandstone, silty sand/sandstone, foraminiferal silty sandstone, and nannofossil chalk.

The transition from Units I to II is marked by a change from gray green siliciclastic turbidites to a sequence dominated by uniformly mottled brownish clay. The boundary between the two units has been placed at the last, clearly identifiable turbidite having a silty sand base at 45 cm in Section 149-899A-6R-2.

Unit II is divided into two subunits on the basis of a gradational change in sediments from poorly consolidated to lithified. Starting from the top of Core 149-899A-14R, and for all the cores in Hole 899B, a saw was used to split the cores. Therefore, all the lithologies below Subunit IIA are described as "stones."

Subunit IIA is dominated by burrow-mottled brownish clay and nannofossil clay. Subunit IIB consists predominantly of grayish green, darkening-upward sequences of nannofossil claystone, and claystone with silt and siltstone with clay. The subunit contains a significant amount of biogenic siliceous material. The boundary between Subunits IIA and IIB is not observed because nothing was recovered in Core 149-899A-12R, and only 1% recovery in Core 149-899A-13R comprising yellowish gray clay. Therefore, the top of Subunit IIB is placed at the top of Core 149-899A-14R, which contains the first sediments showing upward-darkening sequences.

Subunit IIA

The recovery in cores from Subunit IIA (0%-46%) averaged 25%. This subunit is dominated by dark yellowish brown to very pale orange clay, calcareous clay, and nannofossil clay. Minor lithologies include nannofossil ooze and silty sand/sandy silt, which locally contain abundant foraminifers. The lighter-colored sediments have higher carbonate contents. The lithologies generally are mixed by moderate-to-intense bioturbation, which created mottled gradations between relatively carbonate-rich and carbonate-poor sediments. No identifiable ichnofauna could be recognized. Some thin (1-5 cm) intervals of laminated silty sand/sandy silt with sharp bases and gradational tops occur. In Cores 149-899A-7R and -8R and Interval 149-899A-9R-1, 0-70 cm, these are overlain by brown clay, but elsewhere, lighter-colored nannofossil clays occur above them.

Subunit IIB

The average recovery in cores from Subunit IIB was 78% and ranged from 28% to 101%. Most of this recovery is characterized by an alternation of clay- and carbonate-rich lithologies that form upward-darkening sequences ranging in thickness between 10 and 30 cm. These sequences usually have sharp bases and tops, and the lithologies are mixed by moderate-to-intense bioturbation. These are mostly grayish green, but are brown at their tops in Cores 149-899B-10R, -12R, -13R, and -14R.

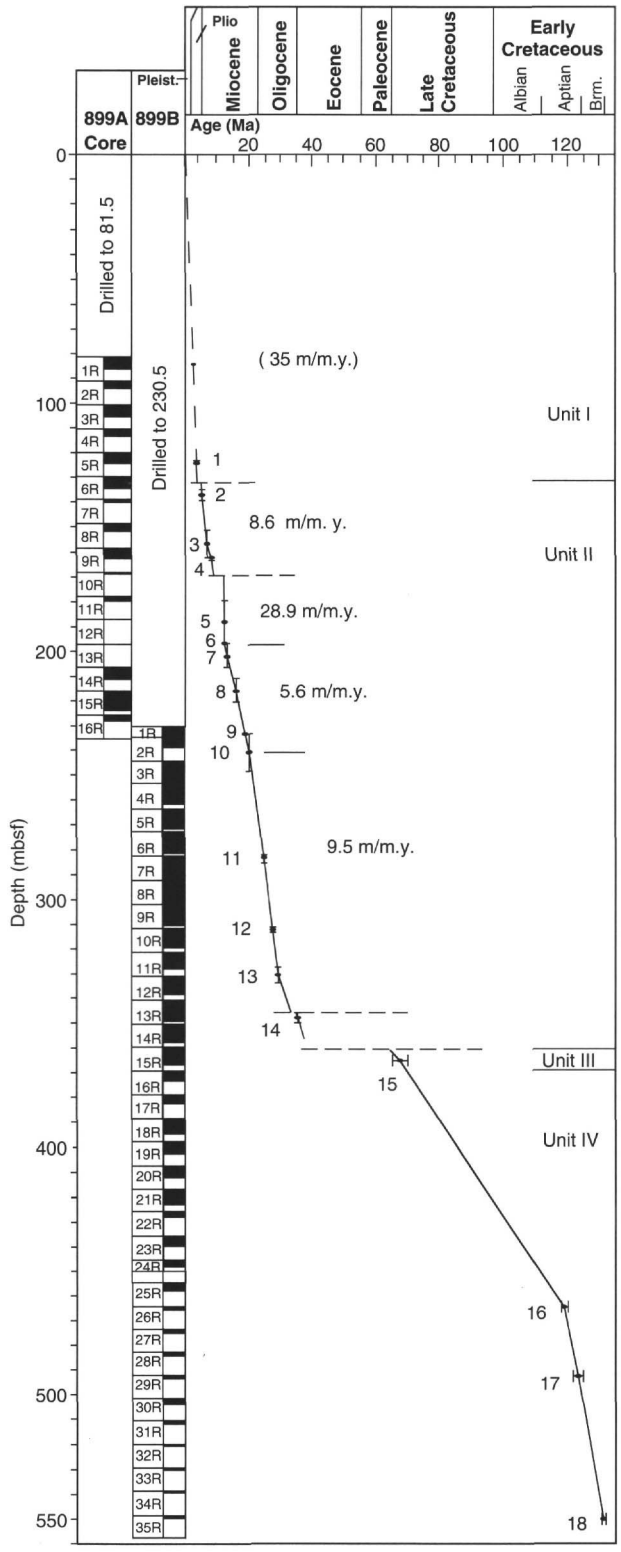

Figure 6. Curve of ages vs. depths for Site 899, plotted from data in Table 3. Each data point is shown with depth error bars. Bold horizontal lines are unconformities. Light horizontal lines are major lithostratigraphic unit boundaries. Slopes of lines connecting adjacent data points are sediment accumulation rates for that time or depth interval. Note that sediment accumulation rates of lithostratigraphic Unit II are substantially lower than those of Unit I.

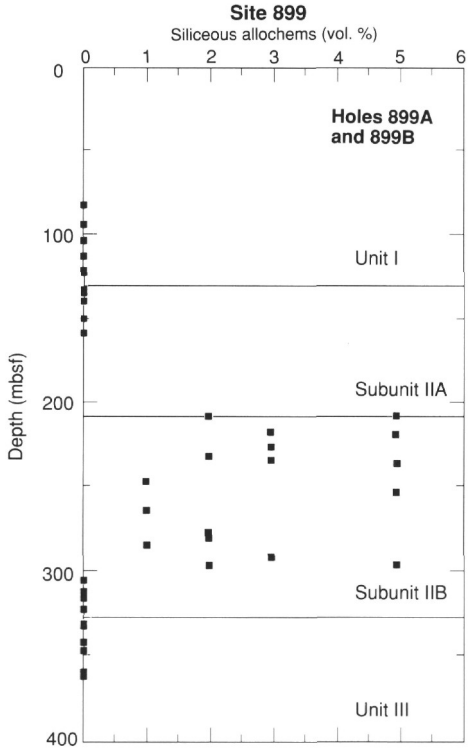

Figure 7. Variation in the content of biogenic siliceous material (sponge spicules, radiolarians, and diatoms) with depth, as revealed by smear-slide analyses.

The upward-darkening sequences are absent in places. Olive gray silty claystones occur in Intervals 149-899A-16R-1, 88 cm, to -16R-CC. Brown claystones with silt occur (e.g., Intervals 149-899B-10R-3, 55-105 cm, and -13R-2, 30 cm, to -13R-4, 80 cm). In places within such intervals, the boundary of the brown coloration is not parallel to bedding and sometimes cuts across burrow traces, which suggests that this coloring is the result of diagenesis.

Major lithologies in Subunit IIB are olive-gray, yellowish brown, and moderate brown silty claystone or clayey siltstone, and light greenish, olive gray, and grayish-orange nannofossil or calcareous claystone. Minor lithologies include claystone, calcareous fine sandstone to siltstone, and silty nannofossil claystone. In sandy and silty lithologies, siliceous allochems (diatoms, sponge spicules, and radiolarians) are common (up to 5% by volume; Fig. 7). Grayish red-purple (5RP 4/2) and dusky blue (5PB 3/2) laminae or blebs (possibly manganese oxide) are scattered throughout.

The typical upward-darkening sequence in Subunit IIB is similar to that described in Subunit IIB at Site 898 (see "Lithostratigraphy" section, "Site 898" chapter, this volume). It begins with a basal, thin bed (up to 5 cm thick, but more commonly 0.5 to 3 cm thick) of mixed biogenic (calcareous and siliceous) and terrigenous fine sandstone to siltstone. Parallel lamination, cross-lamination, ripple cross-lamination, and subtle normally graded bedding are frequent in these sandstones and siltstones. Foraminifer-rich fine sandstones also show scattered, subtle reversely graded bedding, with concentrations of large foraminifer tests on bed tops.

The fine sandstone beds have sharp and flat bases and sharp-to-gradational tops (Fig. 8A). Many of these beds show planar or cross-lamination (Figs. 8B and 8C). Where tops are gradational, the transition from the fine calcareous sandstone to the upper nannofossil claystone is sometimes characterized by a wavy, parallel, or lenticular lamination, as well as by burrow mottling between them. The sand-

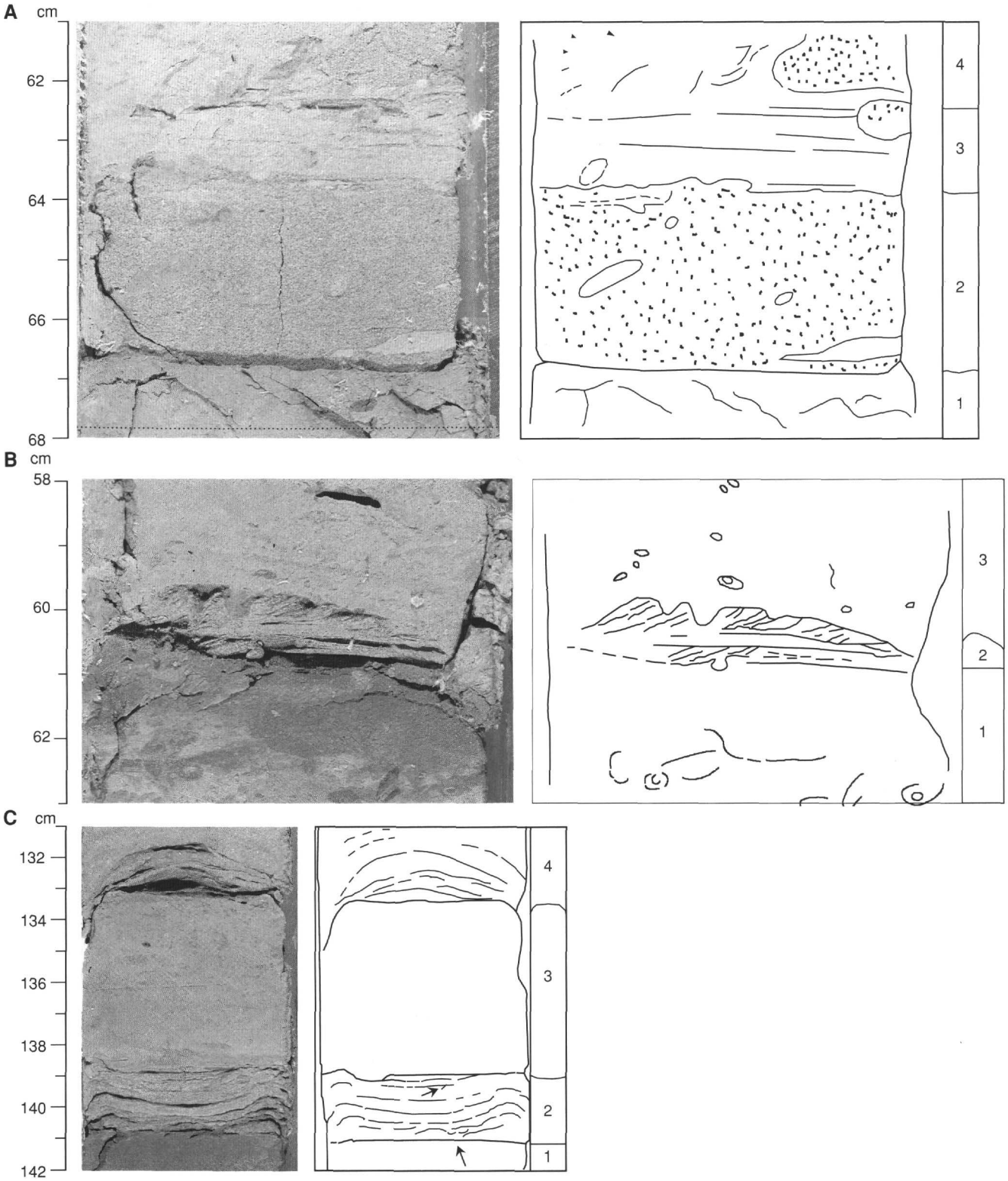

Figure 8. Silty sand beds in Subunit IIB, showing evidence of reworking and deposition by contour currents, rather than turbidity flows: the sands do not show normal grading characteristic of turbidites. **A.** Interval 149-899A-15R-3, 61-68 cm; (1) claystone with silt at top of underlying upward-darkening sequence; (2) massive foraminifer-rich silty sand, showing sharp base and top (slightly burrowed) and scattered burrows; (3) parallel-laminated nannofossil claystone; (4) bioturbated silty claystone with large sand-filled burrows on the right. **B**. Interval 149-899A-15R-5, 58-63 cm. (1) lighter nannofossil claystone and darker claystone with silt mixed by bioturbation at the top of underlying upward-darkening sequence; (2) cross-laminated silty sandstone with small load cast at the base and burrowed top; the mound-shaped upper surface suggests the presence of a current ripple; (3) faintly laminated and slightly bioturbated *(?Chondrites)* nannofossil claystone. **C**. Interval 149-899B-5R-4, 131-142 cm. (1) claystone with silt; (2) parallel-laminated silty sandstone disturbed by drilling, with a sharp base and top, and showing small burrows (arrows); (3) nannofossil claystone showing upward increase in *Chondrites* of density burrows; (4) parallel-laminated sandstone showing sharp base and top overlain by faintly laminated nannofossil claystone.

stone and siltstone beds make up about 5% of the total thickness of Subunit IIB.

The basal silt- and sand-rich intervals of the upward darkening sequences are overlain by nannofossil claystones. The boundary with the overlying darker silty claystones and claystones is transitional as a result of mixing by bioturbation. A clearly identifiable ichnofauna (*Zoophycos, Planolites,* and *Chondrites*) has been concentrated (or is more clearly visible) in the light-colored, carbonate-rich lithologies in the lower part of each individual sequence. Usually, burrowing extends down to the basal calcareous sandstone bed.

In Hole 899B, slump structures involving claystones and nannofossil claystones are present in several cores (Intervals 149-899B-3R-4, 85-110 cm; 149-899B-5R-3, 30-80 cm; 149-899B-7R-4, 90-95 cm; and 149-899B-8R-3, 100-145 cm); some of these are illustrated in Figure 9.

Petrography

Sand- and silt-sized detritus in Unit II includes components similar to the assemblage observed in Unit I. Unit II also contains clay-rich lithologies that are similar to those in Unit I, except that the Type 2 clay-rich lithologies (oriented clays in carbonate-poor lithologies; defined in "Lithostratigraphy" section, "Site 897" chapter, this volume) are a more persistent and volumetrically significant part of the lithologic assemblage.

Depositional Processes

Subunit IIA

Continuous, slow accumulation by settling through the water column accounts for the clay and nannofossil ooze and for some of the nannofossil clay in this subunit. The few sharp-based, normally graded sequences suggest scattered turbidity flows that transported siliciclastic sand and silts or nannofossil clay material. The moderate-to-intense bioturbation indicates relatively slow deposition, as confirmed by the sediment accumulation rate (Fig. 6) in dysaerobic or normal oxygenated conditions. The relatively high content of biogenic carbonate components indicates that deposition occurred above the CCD.

The position of Subunit IIA, between the terrigenous sandy turbidites of Unit I and the distal, muddy current-deposited facies of Subunit IIB, suggests deposition in an abyssal plain setting that was dominated by hemipelagic and pelagic sedimentation, but that occasionally received siliciclastic and carbonate materials from mud-dominated turbidity flows.

Subunit IIB

Although repetitive, upward-darkening sequences can be seen through most of Subunit IIB, these do not exhibit the clear, normally graded turbidite signature characteristic of Unit I. Thin silty sand and silt intervals at the bases of many of the upward-darkening sequences lack clear, normal grading (Fig. 8). Silty sands and silts that contain small-scale cross-stratification and parallel lamination indicate bottom current activity (Fig. 8B). Some show reverse grading or have sharp tops as well as sharp bases. The tops often show "lag deposits" of large foraminifer tests. All these features point to reworking by contour currents, as described by Stow and Piper (1984). Possibly, some of the homogeneous, carbonate-poor terrigenous silty claystones and claystones may be mud turbidites or contourites.

The high carbonate content and well-preserved nannofossils (see "Biostratigraphy" section, this chapter) indicate deposition above the CCD, and the ubiquitous bioturbation suggests at least a dysaerobic, if not normally oxygenated, environment. The slumped intervals (Fig. 9) indicate penecontemporaneous downslope movement of sediments.

The presence of turbidites, contourites, and slump deposits in Subunit IIB indicates an abyssal plain setting near the continental rise, consistent with the site's location on the continental side of the Iberia Abyssal Plain, and the relatively low sediment accumulation rate.

Unit III

Cores 149-899B-15R-1, 42 cm, to -16R-1, 7 cm
Depth: 360.6-369.9 mbsf
Age: late Eocene to Campanian/early Maastrichtian

General Description

The boundary between Units II and III was placed at the first occurrence of bands containing disseminated black organic material within claystones. Above the boundary, there is a gradual downward change in color from reddish brown to yellowish brown.

Unit III occurs almost entirely within Core 149-899B-15R and is divided into two subunits. Subunit IIIA is entirely claystone with bands of disseminated black organic material, and Subunit IIIB contains variegated sandy silty claystone, sandstone, and clayey conglomerate. The top of Subunit IIIB is marked by the first sandstone layer at 141 cm in Core 149-899B-15R-3. The colors of the lithologies in Subunit III are summarized in Table 4.

Subunit IIIA

Subunit IIIA consists of mottled, dark yellowish brown and pale yellowish brown (Table 4) claystone with grayish orange lenses of siltstones in the upper part of Section 149-899B-15R-1. The claystones contain several black (N1) organic-rich layers, 2 to 10 cm thick, as well as very hard, brownish black (5YR 2/1) concretions (up to 0.5 by 1 cm). Bioturbation decreases from the top to the bottom of the subunit.

The clay minerals in the carbonate-poor claystone and silty claystone in Subunit IIIA are highly oriented. Silt grains, where present, generally have coatings of yellow birefringent clay. These petrographic characteristics correspond to Type 2 claystones (see definition in "Lithostratigraphy" section, "Site 897" chapter, this volume).

Subunit IIIB

Lithologies within Subunit IIIB include variegated sandstone with clayey silty matrix, very compacted moderate brown sandy silty claystone, white highly altered volcanic ash, laminated brown claystone, lighter-colored silty claystone with black concretions (Fig. 10), and a poorly cemented, multicolored, polymictic, clayey conglomerate. Highly altered basaltic clasts are present in the gravel- and sand-sized fractions. Two different types of sandstone are present:

1. Laminated, poorly sorted, poorly cemented sandstone having thin laminae of claystone (Intervals 149-899B-15R-3, 141-150 cm, and 15R-4, 0-30 cm).
2. Medium-grained, brown, ferruginous-rich sandstone with well-rounded grains, generally fining upward, but exhibiting normal and reverse grading in Section 149-899A-15R-4.

A few localized beds of dark brown to yellowish brown, bioturbated, highly cemented siltstone to claystone are present in Section 149-899B-15R-4.

The lower part of Subunit IIIB consists of a highly weathered, polymictic, poorly cemented, matrix-rich, variegated conglomerate (Table 4). The clasts include black metasediments, white claystone, granule-sized green grains of expandable clay mineral, and highly altered pebble-sized basalt clasts. A yellowish sandstone at 127 cm in Section 149-899B-15R-4 yielded Campanian to early Maastrichtian foraminifers (see "Biostratigraphy" section, this chapter). Silt- and sand-sized material in Subunit IIIB is mostly quartz and alkali feldspar, and therefore, sandstones and siltstones in this subunit have been classified as arkoses (from classification of Folk, 1980).

Depositional Processes

Subunit IIIA

The carbonate-poor claystones of Subunit IIIA are the result of slow accumulation in an oxygenated environment, probably below

the CCD. This depositional environment is similar to that described for Subunit IIIA at Site 897 (see "Lithostratigraphy" section, "Site 897" chapter, this volume).

Subunit IIIB

Subunit IIIB is interpreted as a mixture of fine-grained hemipelagic/pelagic deposits and high-density turbidity currents or fluidized sand-silt-clay debris flows that developed on relatively gentle slopes, as interpreted for this subunit at Site 897. The basal, poorly sorted, clayey conglomerate interval may have developed as a "weathering" zone, with reworked material having been developed from the top of Unit IV. This zone might have formed sometime during the period between the youngest date (early Aptian) obtained from sediments in the underlying Unit IV, and the Campanian to Maastrichtian age of the sandstone that overlies the red brown conglomerate in Subunit IIIB.

Unit IV

Cores 149-899B-16R-1, 7 cm, to -37R-1, 32 cm
Depth: 369.9-557.9 mbsf
Age: pre-Late Cretaceous to late Barremian

General Description

The upper boundary of Unit IV corresponds to the top of acoustic basement (see "Integration of Seismic Profiles with Observations from the Site" section, this chapter). Figure 11 (back-pocket figure) depicts the lithologic sequence observed in Unit IV, which has been correlated to recovered intervals. Three main lithologic associations were observed within this unit:

1. A serpentinite breccia that occurs in three intervals (designated the Upper, Middle, and Lower Breccia Units) and ranges in thickness from nearly 100 to less than 10m;
2. An association of claystones, calcareous claystones, soft, altered, and deformed serpentine masses, and minor siltstone that occurs intercalated between the breccia intervals and between the sections of serpentinized ultramafic rocks;
3. Discrete sections of unbrecciated serpentinite, serpentinized peridotite, gabbro, and basalt. The basalt fragments are of variable composition and some occur within the claystones and the soft, altered, and deformed serpentine masses.

Unit IV is divided into two subunits (see Fig. 11, back-pocket figure). The top of Subunit IVA was placed at the top of the Upper Breccia Unit (Core 149-899B-16R-1 at 7 cm). This subunit consists of the serpentinite breccias and their associated sedimentary intervals. Core recovery in this subunit averaged 40%. Recovery in cores above and below the top of Unit IV was near 50%, so the change to the breccias characteristic of Subunit IVA occurs over only a few meters.

The Upper Breccia Unit is approximately 95 m thick and constitutes 83% of the recovered interval in Subunit IVA. The Middle and Lower Breccia Units are thinner and are separated from the Upper Breccia Unit and one another by sediments (Fig. 11, back-pocket figure).

The top of Subunit IVB is placed at the base of the Lower Breccia Unit (Fig. 11, back-pocket figure; Core 149-899B-28R-1 at 128 cm). Subunit IVB consists of sedimentary intervals and discrete, boulder-sized intervals (30 cm to >3 m thick) of serpentinized mafic and ultramafic rocks. Core recovery in this subunit averaged 14% and about 80% of the rock recovered consists of pieces of serpentinite, serpentinized peridotite, and microgabbroic rocks. Although much of this material shows evidence of fracturing and other deformation, breccia units similar to those described in Subunit IVA are not present.

Serpentinite Breccias

Lithologic Description

The Upper, Lower, and Middle Breccia Units are similar in lithology. The following description, based on study of the thicker Upper Breccia Unit, probably applies to all three units.

The breccias are poorly sorted, polymictic breccias composed of angular clasts with a very restricted range of composition. No obvious distinction can be seen between "clasts" and "matrix," and a continuous range of particle sizes from microscopic fragments to boulder-sized blocks more than 1 m wide is present. The rocks are coherent, although the nature of any cement is uncertain and not obvious under the microscope (see below).

Shape can be estimated only for the smaller (<4 cm) clasts. These are generally equidimensional and have an estimated visual sphericity of about 0.8 (Folk, 1980), probably reflecting the isotropic nature of most of the igneous and metamorphic rocks that formed these clasts. The estimated average roundness of each clast is about 0.2 to 0.3 (Folk, 1980) for clasts contained entirely within the bounds of the core. However, microscopic clasts appear to be even less rounded (0.1-0.2), indicating that these relatively soft serpentinite fragments have suffered minimal transport prior to inclusion in the breccia or significant fracturing during entrainment or emplacement.

The composition of the clasts is a striking feature of these three breccia units. Clasts of only two types are present (see detailed discussion below). The dominant lithology is serpentinitized peridotite (>90% of all fragments). The peridotitic fragments vary widely in composition, and both pyroxene-rich and olivine-rich (dunitic) types are present. Some of the serpentinized peridotite clasts show evidence of deformation prior to inclusion in the breccia (see "Structural Geology" section, this chapter). In the upper part of the Upper Breccia Unit, (Cores 149-899B-16R and -17R), the clasts are dominantly yellow (typically 10YR 4/2 to 10YR 5/4), calcitized, and oxidized; elsewhere in the Upper Breccia Unit, and in the other two breccia units, the serpentinite clasts are greenish black (5GY 2/1). Fragments of metamorphosed Mg-rich igneous rocks (<10% of all clasts) constitute the only other clast type present. Such rock fragments generally are small in size (<10 cm), and white, gray, or even pink. The mineralogy of these metamorphic fragments is discussed in more detail below.

Clast size was studied by systematically measuring the larger clasts in the recovered cores through the Upper Breccia Unit (Table 6). Apparent maximum size shown on the cut surface of the core was recorded. For larger, boulder-sized blocks, the measurement recorded is the length of continuous core that intersected the block. A histogram drawn from 156 clasts having an apparent maximum size greater than 2 cm (Fig. 12) shows that smaller fragments (2-5 cm) dominate and that the size distribution is approximately logarithmic binomial. The median size of clasts >2 cm is 3.75 cm. This size distribution mimics that found in some glacial tills and in the lunar regolith.

Figure 13 shows the apparent maximum size of each measured clast plotted vs. depth, demonstrating that there is a tendency for larger clasts to be restricted to the central part of the Upper Breccia Unit. The significance, if any, of this relationship is uncertain.

Although the bulk composition of these three breccia units is clear from examination of the clasts, three samples were analyzed for major elements. The samples did not contain large clasts and thus are representative of the finer material within the Upper Breccia Unit (Table 7). The ultramafic bulk composition of the unit was confirmed by these analytical data. This conclusion also is supported by analyses of trace elements in a much larger sample set (Table 8).

In summary, the breccia units are poorly sorted, and composed of a suite of ultramafic clasts of a restricted compositional range. The clasts vary widely in size from boulders to microscopic pieces, and the small and microscopic fragments are highly angular in shape.

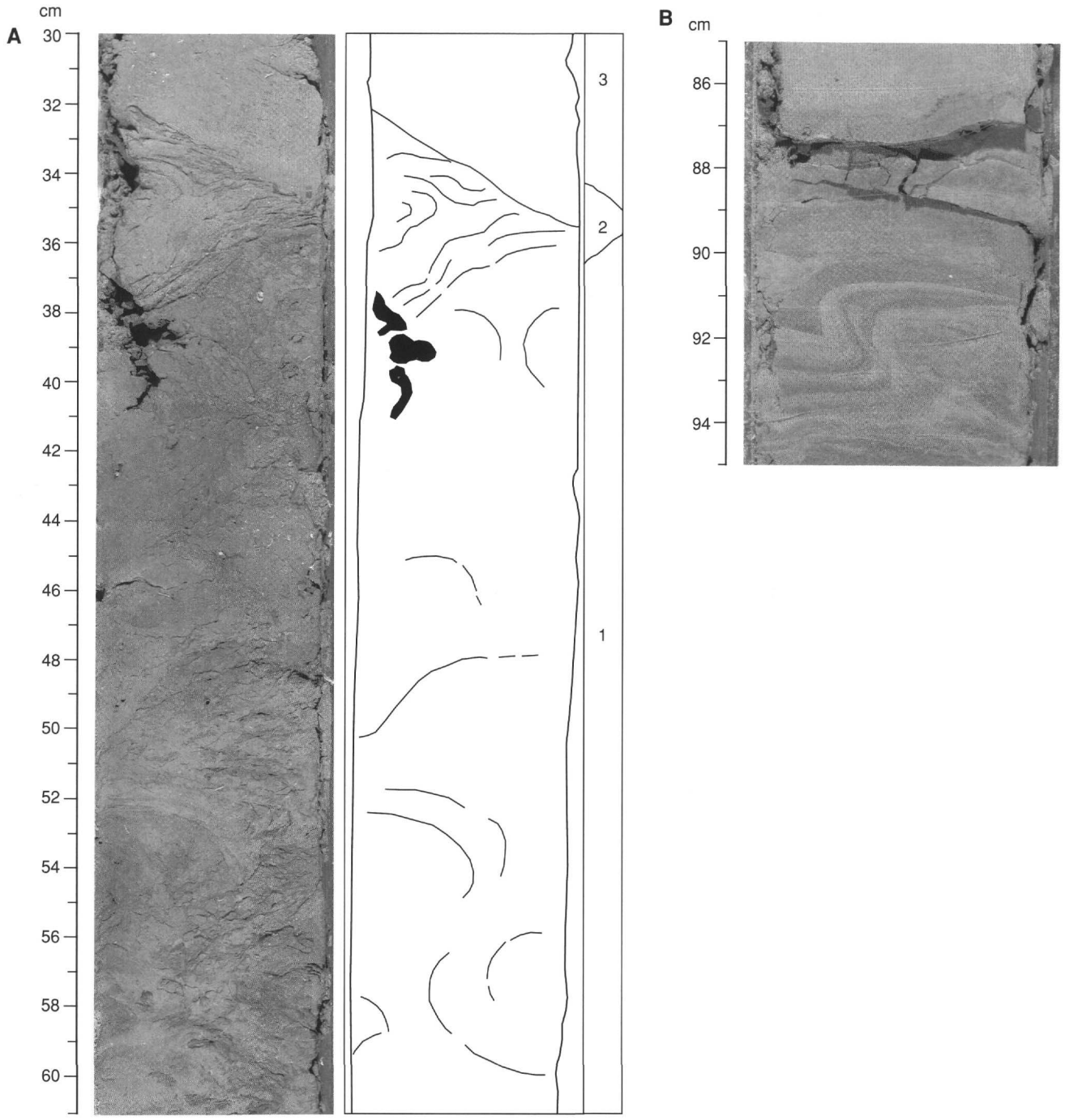

Figure 9. Slump structures in Subunit IIB. **A**. Deformed zone probably produced by slumping. The deformed claystone interval (1) is overlain by a deformed clayey siltstone (2), which is truncated by a nannofossil claystone with *Chondrites* burrows; Interval 149-899B-5R-3, 30-61 cm. **B**. Small slump fold at the base of an upward-darkening sequence; Interval 149-899B-7R-4, 85-95 cm. **C**. Large slump fold that has inverted a sandy basal interval of attribute: (1) silty sand base; (2) bioturbated nannofossil claystone repeated by fold (lower interval is the right way up); (3) nannofossil claystone in core of slump fold (Interval 149-899B-8R-3, 93-139 cm).

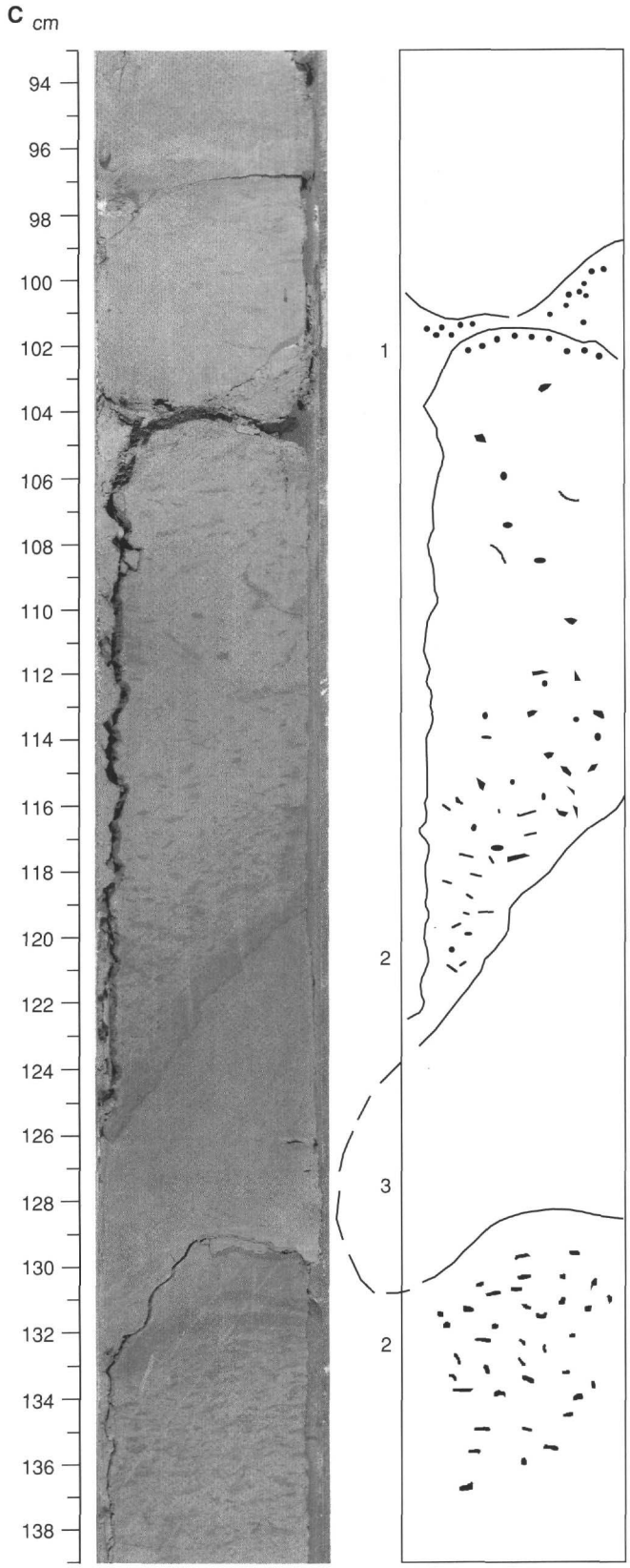

Figure 9 (continued).

Table 6. Apparent maximum clast size in Upper Breccia Unit of Subunit IVA.

Clast no.	Core, section, interval (cm)	Diam. (cm)	Truncated (?)	Color	Lithology
1	16R-1, 58–61	4		10YR7/4	Yellow carbonated mesh serpentinite
2	16R-1, 66–69	3		10YR7/4	Yellow carbonated mesh serpentinite
3	16R-1, 86–88	2		10YR4/2	Yellow carbonated mesh serpentinite
4	16R-2, 8–10	2		5G2/1	Fine-grained gray metamorphic rock(?)
5	16R-2, 16R–21	5		5G2/1	Fine-grained gray metamorphic rock(?) cut by two generations of veins, (one pinkish)
6	16R-2, 66–68	2	T	10YR8/2	Yellow calcitized mesh serpentinite
7	16R-2, 73–78	4		10YR7/4	Yellow calcitized mesh serpentinite
8	16R-2, 83–87	4		10YR7/4	Yellow calcitized mesh serpentinite
9	16R-2, 88–91	4		5G4/1	Mantled fine-grained clast of gray metamorphic rock
10	16R-2, 91–95	4	T	10YR8/2 5G4/1	Yellow calcitized mesh serpentinite
11	16R-2, 112–115	4	T	10YR8/2 5G4/1	Yellow calcitized mesh serpentinite
12	16R-2, 123–125	2		SPECKLED 5G2/1	Mantled speckled gray rock
13	16R-3, 1–5	5		10YR6/6	Veined serpentinized pyroxenite
14	16R-3, 5–8	4		5Y8/1	Carbonated yellow mesh serpentinite
15	16R-3, 15–16	2		5GY4/1	Fine-grained gray metamorphic rock
16	16R-3, 19–21	3		5GY4/1	Fine-grained gray metamorphic rock
17	16R-3, 39–54	6	T	10YR7/4	Carbonated yellow mesh serpentinite
18	16R-4, 7–14	8	T	10YR7/4	Carbonated yellow mesh serpentinite
19	16R-4, 24–29	5		10YR7/4	Carbonated yellow mesh serpentinite with relict grains of green chrome diopside
20	16R-4, 136–137	2		5BG3/2	Angular green serpentinite
21	16R-4, 138–140	2		10YR7/4	Ghost-veined carbonated yellow mesh serpentinite
22	17R-1				Piece 1 is a siliceous sedimentary drlling dropstone
23	17R-2				Piece 2 is a fine-grained serpentinite drilling dropstone
24	17R-1, 8–40	32	T	10YR7/4	Large block of yellow carbonated mesh serpentinite Pieces 3 thru 6 is probably one block
25	17R-1, 67–73	6	T	10YR7/4	Ghost veined carbonated yellow mesh serpentinite
26	17R-1, 107–110	3		10R8/2 GREEN	Pink green chertlike serpentinite block
27	17R-1, 120–123	4		10YR4/2	Dark yellow mesh serpentinite
28	17R-2, 19–24	5	T	10YR7/4	Dark yellow mesh serpentinite (ghost)
29	17R-2, 23–26	6	T	10YR7/4	Dark yellow mesh serpentinite (ghost)
30	17R-2, 110–113	3		5YR7/2	Pinkish yellow serpentinite
31	17R-2, 139–143	4		10YR6/2	Carbonated yellow mesh serpentinite with internal dark-gray patches
32	17R-3, 110–116	8	T	10YR7/4	Piece 12 is a yellow calcitized mesh serpentinite clast (no matrix)
33	17R-3, 47–51	4		10YR2/2	Dark yellow calcitized mesh serpentinite with maghemite(?) patches
34	17R-3, 38–40	2		10YR2/2	Dark yellow calcitized mesh serpentinite with maghemite(?) patches
35	17R-3, 26–29	3		10YR2/2	Dark yellow calcitized mesh serpentinite with maghemite(?) patches
36	18R-1, 65–68	4		10YR2/2	Dark gray/yellow mesh serpentinite Altered and carbonated with maghemite(?) patches
37	18R-2, 38–41	3		5YR5/6	Serpentine, but not mesh serpentinite, with dark brown stain and carbonate
38	18R-2, 0–9	9	T	10YR6/6	Green brown serpeninized pyroxene bearing peridotite Margin of clast marked by veins
39	18R-2, 51–53	3		5R8/2 N7	Piece 2 - streaky rock, gray-pink, altered metamorphic clast?
40	18R-2, 54–57	5		5R8/2 N7	Piece 3 - streaky rock, gray-pink, altered metamorphic clast
41	18R-2, 74–81	8	T	5YR4/1	Angular maghemite serpentinite block
42	18R-2, 86–89	3		10YR6/6	Angular clast of brown serpentine
43	18R-2, 89–92	3		10YR2/2	Dark brown mesh serpentinite with maghemite
44	18R-2, 102–103	2		N4	Gray zoned and mantled clast
45	18R-3, 15–18	3		5YR4/1	Angular maghemite serpentinite block
46	18R-3, 77–79	3		10YR4/2	Gray mesh serpentinite
47	18R-3, 82–85	6	T	5YR5/6	Yellow serpentinite block cut by veins going from matrix into block
48	18R-3, 89–90	3		5YR5/6	Yellow serpentinite block cut by veins going from matrix into block
49	18R-3, 89–92	4		5YR5/6	Yellow serpentinite block cut by veins going from matrix into block
50	18R-4, 2–9	T		10YR6/6	Yellow carbonated serpentinite with veins going from matrix into block
51	18R-4, 3–7	4		10YR2/2	Mesh serpentinite with maghemite staining
52	18R-4, 20–24	4		10YR2/2	Yellow mesh serpentinite cut by veins of maghemite
53	18R-4, 58–63	6	T	10YR2/2	Angular block cut by veins of maghemite
54	18R-4, 107–111	4		5EY6/1	Varigated green-yellow serpentinite
55	18R-5, 13–15	2		5GY4/1	Metamorphic rock clast
56	18R-5, 34–38	4	T	5GY4/1	Pyroxenite(?) clast with pyroxene altered to brown Fe-oxides(?)
57	18R-5, 37–49	12	T	5GY4/1	Pyroxenite(?) clast with pyroxene altered to brown Fe-oxides(?)
58	18R-5, 68–74	6	T	10YR6/6	Large pyroxenite block oxidized and carbonated
59	18R-5, 77–81	4		5GY4/1	Metamorphic rock
60	18R-5, 79–83	4		5GY4/1	Metamorphic rock
61	18R-5, 99–102	3		10YR2/2	Serpentinite with maghemite staining
62	19R-1, 8–16	8	T	5G2/1	Pyroxenite clast
63	19R-1, 21–24	4	T	5G4/1	Mesh serpentinite clast without carbonate
64	19R-1, 92–96	3	T	10YR6/6	Yellow mottled calcitized serpentinite
65	19R-1, 91–93	2		10YR6/6	Dark yellow mottled calcitized serpentinite
66	19R-1, 110–114	4		5YR5/6	Dark yellow mottled calcitized serpentinite
67	19R-1, 135–142	7	T	5G4/1	Green pyroxenite
68	19R-2, 8–12	4	T	5G4/1	Green gray pyroxenite cut by vein
69	19R-2, 45–49	4	T	5GY6/1	Serpentinite?
70	19R-2, 87–90	6	T	5GY4/1	Fine grained metamorphic rock?
71	19R-2, 98–100	3			Pink-gray veined clast
72	19R-2, 107–112	6	T	5GY4/1	Gray-green serpentinite ghost
73	19R-2, 120–134	14	T	5G4/1	Pyroxenite
74	19R-3&4, 0–75	184	T	5G4/1	Large serpentinite block in Sections 3 (0 cm) to Section 4 (75 cm)
75	20R-1, 50–55	5	T	5G4/1	Veined and multicolored serpentinite
76	20R-1, 61–63	2.0			Pink pebble
77	20R-1, 87–93	7	T	5GY6/1	Veined and multicolored serpentinite ghost
78	20R-1, 131–136	5		N6	Gray metamorphic rock?
79	20R-2, 0–59	59	T	5G4/1	Noncalcitized serpentinite fragment
80	20R-2, 88–95	7	T	N6	Fine-grained gray diorite?
81	20R-2, 136–140	4	T	N6	Rounded gray metamorphic rock clast cut by vein; no zone of alteration at the margin
82	20R-3, 20–24	4		N6	Gray metamorphic rock cut by external serpentine vein
83	20R-3, 35–42	7	T	N5	Fine- to coarse-grained serpentinite clast with thin dark veins
84	20R-3, 76–78	2		N7	Metamorphic rock clast with large serpentine vein that stops at the clast boundary
85	20R-3, 114–117	3		N6	Fine-to-coarse rounded serpentinite clast with gray area within a larger darker region
86	20R-4, 17–28	11	T	5Y8/1 to N5	Multicolored serpentinite clast included within a larger dark serpentinite region
87	21R-1, 4–9	5	T	10YR5/4	Multicolored clast with veined border
88	21R-1, 19–24	2	T	10YR8/6	Several small angular to rounded clasts

Table 6. (continued).

Clast no.	Core, section, interval (cm)	Diam. (cm)	Truncated (?)	Color	Lithology
89	21R-1, 5–8	3		10YR7/4	Angular fragment cut by later vein
90	21R-1, 54–56	3		10YR7/4	Orange patches in white to light gray matrix resulting from mineral growth pattern
91	21R-1, 56–61	5		10YR7/4	Orange patches cut by numerous veins
92	21R-1, 101–104	5	T	N4	Brecciated metamorphic rock clast with serpentine veins
93	21R-2, 21–24	5		5YR4/1	Rounded brecciated clast bounded and cut by later veins
94	21R-2, 31–36	4		5YR4/1	Rounded brecciated clast bounded and cut by later veins
95	21R-2, 31–36	4		10YR6/6	Subrounded clast with relict crystal outlines replaced by orange mineral, clast cut by veins
96	21R-2, 48–123	55	T	N6	Large block of serpentinized peridotite cut by serpentine veins
97	21R-3, 0–9	10	T	5GY6/1	Serpentinized peridotite clast bounded by large veins
98	21R-3, 29–32	3		N5	Subangular metamorphic rock clast rimmed by vein, altered coarse materials within clast
99	21R-3, 51–54	4		N4	Rounded metamorphic rock clast partially bounded by veins and cut by veins
100	21R-3, 93–95	2		5B9/1	Subangular clast
101	21R-3, 115–117	3		N7	Rounded metamorphic rock clast with surrounding vein slightly beyond actual clast boundary
102	21R-4, 41–44	4		N7	Rounded metamorphic rock clast faulted in two with a white vein at one end of both pieces
103	21R-4, 58–128	70	T	N5	Large serpentinized peridotite clast
104	21R-4, 129–135	6		N7	Altered metamorphic rock clast?
105	21R-5, 34–42	8		N7	Subangular altered metamorphic rock
106	21R-5, 40–43	3		5YR6/1	Altered serpentinized peridotite(?) partially surrounded and cut by veins
107	22R-1, 7–10	3		N8	Angular white talc(?) clast
108	22R-1, 9–12	4		5Y4/1	Serpentinized peridotite clast
109	22R-1, 26–29	5		5B7/1	Serpentinized peridotite clast with large vein border zone with breccia
110	22R-1, 108–114	5		N7	Altered metamorphic rock clast?
111	22R-1, 117–120	3		5Y6/1	Rounded serpentinized peridotite clast
112	22R-1, 125–130	5		5Y6/1	Subangular serpentinized peridotite clast
113	22R-1, 135–137	2		N6	Subangular altered metamorphic rock clast
114	22R-2, 0–48	4	T	5Y4/1	Large block of serpentinized peridotite
115	22R-2, 54–57	3		5Y4/1	Serpentinized peridotite clast with magnetite? veins that is partly bounded by a vein
116	22R-2, 108–113	5		N7	Light-colored clast with contorted veins
117	23R-1, 39–41	2		N3	Subrounded clast with internal structure of a zoned vein
118	23R-1, 45–48	3		N7	Rounded altered metamorphic rock clast
119	23R-1, 60–63	3		N6	Rounded serpentinized peridotite clast
120	23R-1, 93–95	2		N6	Angular altered metamorphic rock clast
121	23R-1, 95–97	3		N6	Angular altered metamorphic rock clast
122	23R-1, 139–142	3		N7	Subrounded serpentinized peridotite clast
123	23R-2, 1–3	2		N7	Altered metamorphic rock clast
124	23R-2, 7–9	2		N7	Altered metamorphic rock clast
125	23R-2, 34–68	34	T	N6	Serpentinized peridotite clast
126	23R-2, 117–119	2		N2	Serpentinized peridotite clast
127	23R-2, 137–139	2		5Y4/1	Serpentinized peridotite clast
128	23R-3, 29–31	2		N7	Altered metamorphic rock clast
129	23R-3, 29–31	2		N8	Badly altered metamorphic rock clast
130	23R-3, 37–39	3		5YR6/4	Angular serpentinized peridotite clast
131	23R-3, 43–46	3		N3	Altered metamorphic rock with veins; contains small en-echelon rock slivers in the veins
132	23R-3, 104–107	3		5YR6/4	Angular serpentinized peridotite clast
133	23R-3, 117–120	4		N7 to 5R7/4	Serpentinized peridotite clast cut by veins, including a bright pink clast
134	23R-4, 9–11	3		N6	Subrounded altered metamorphic rock clast
135	23R-4, 25–29	5		5YR5/6	Clast with orange mineral alteration
136	24R-1, 8–10	3		N6	Subangular metamorphic rock clast surrounded by a vein
137	24R-1, 36–38	2		N6	Subangular metamorphic rock clast surrounded by a vein
138	24R-1, 50–53	3		5Y4/1	Serpentinized peridotite clast surrounded by a vein
139	24R-2, 20–23	3		5Y4/1	Serpentinized peridotite clast
140	24R-2, 25–30	5		N3	Altered metamorphic rock clast
141	24R-2, 49–51	2		N3	Angular clast of altered metamorphic rock
142	24R-2, 53–55	2		N5	Rounded clast of altered metamorphic rock
143	24R-2, 127–132	5		5GY6/1	Serpentinized peridotite clast
144	24R-2, 134–140	6		N6	Altered microdiorite? clast
145	24R-3, 61–63	3		5YR6/4	Serpentinized peridotite with bluish veins
146	24R-3, 76–78	2		N6	Altered metamorphic rock clast
147	25R-1, 79–81	2		N6	Altered metamorphic rock clast
148	25R-2, 27–29	2		N7	Altered metamorphic rock clast
149	25R-2, 91–93	2		N7	Altered metamorphic rock clast
150	25R-3, 8–10	2		25RY6/1	Serpentinized peridotite clast
151	25R-3, 62–64	2		25RYR6/4	Orange alteration in clast
152	26R-1, 4–8	4		N6	Serpentinized peridotite clast
153	26R-1, 13–12	2		N3	Altered metamorphic rock clast
154	26R-1, 23–25	2		N3	Altered metamorphic rock clast
155	26R-1, 43–45	2		N6	Serpentinized peridotite clast
156	26R-1, 123–125	2		N4	*Metamorphic rock with feathery (?)plagioclase radiating from nucleation sites*
157	26R-2, 27–29	2		N4	Altered metamorphic rock clast
158	26R-2, 29–32	3		N7	Vein rimmed serpentinized peridotite clast

Note: Only clasts larger than 2 cm were measured.

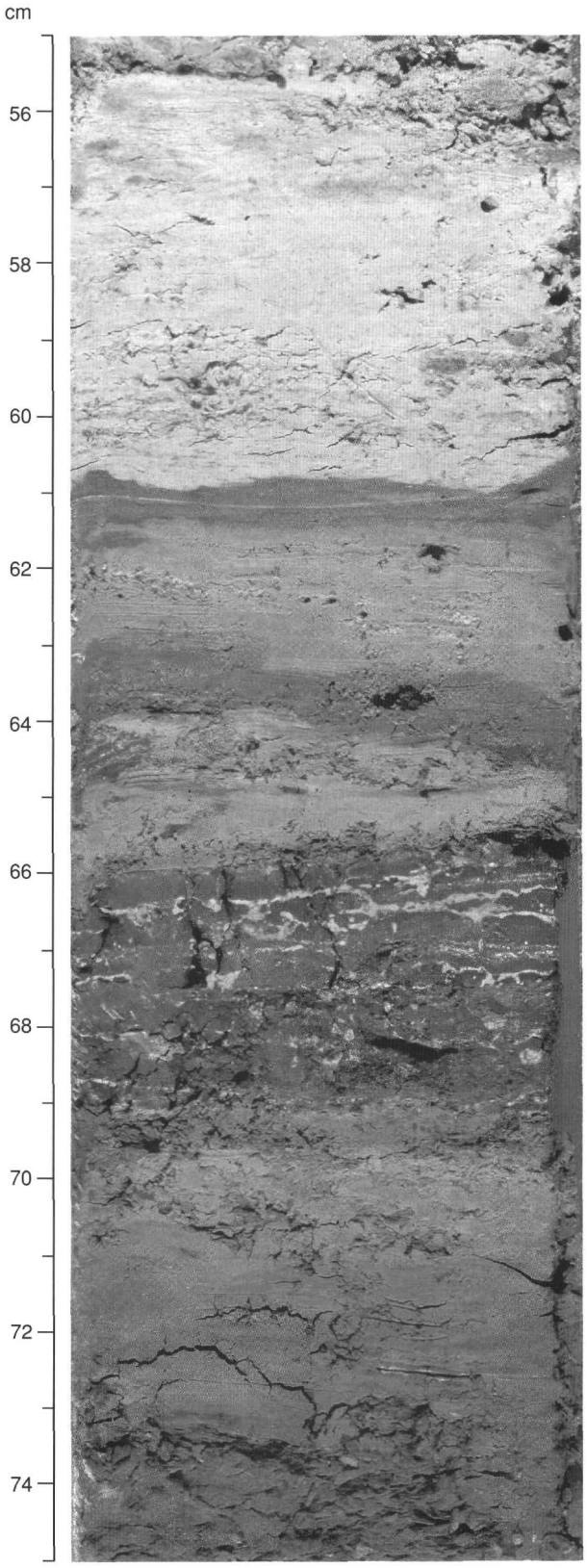

Figure 10. Subunit IIIB. Small-scale variations within clay-rich lithologies include white claystone (55.5-61 cm, possible volcanic ash?), moderate brown claystone with black concretions, and bioturbated dusky yellow claystone (61-66 cm), all overlying dark reddish brown clayey conglomerate (Interval 149-899B-15R-4, 55-75 cm).

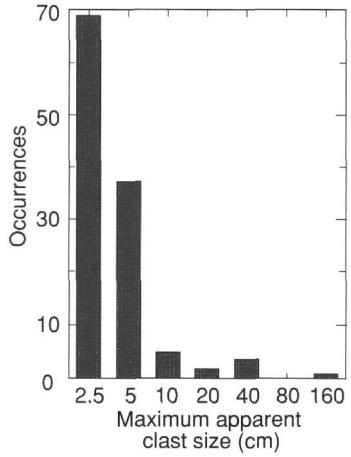

Figure 12. Histogram of apparent maximum size of clasts from the Upper Breccia Unit.

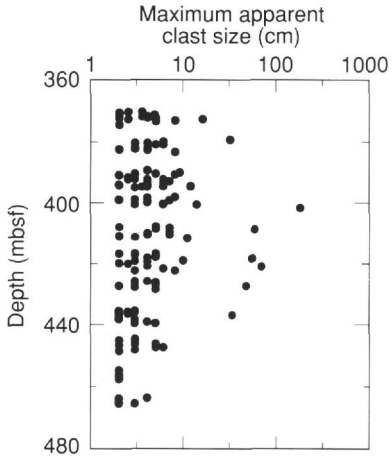

Figure 13. Apparent maximum clast size in the Upper Breccia Unit vs. depth. A slight tendency exists for the larger clasts to occur preferentially in the center of the Upper Breccia Unit (note logarithmic size scale).

Clast Petrology

Only two types of clast occur within the three breccias. Most are serpentinized peridotites, but a minority (<10%) of the clasts are metamorphosed Mg-rich igneous rocks.

Serpentinized Peridotite Clasts

The larger blocks (cobbles to boulders) are variable in composition and range from altered serpentinites to pyroxene-rich and pyroxene-poor peridotites. In the upper part of the Upper Breccia Unit (Cores 149-899B-16R to -18R), the serpentinite clasts have been highly altered. Bright green granules and rare larger clasts appear to be made of clay (smectite?), possibly derived from pyroxene crystals. Other fragments are gravel-sized, white to creamy, altered serpentinite, crosscut by purple to dark blue serpentine veins. Some of these contain a similar bright green mineral (e.g., Intervals 149-899B-16R-3, 43-60 cm, and-17R-1, 16-38 cm; Fig. 14).

Below this altered horizon in the Upper Breccia Unit, the dominant clasts are serpentinized peridotites that lack the obvious clay alteration. Several different varieties can be distinguished:

1. Pyroxenites, with pale and dark green pyroxene crystals, locally altered to an orange to red mineral (e.g., Intervals 149-899B-

Table 7. Major element composition of three samples from the Upper Breccia Unit of Subunit IVA, Hole 899B.

Core, section, interval (cm)	SiO_2	TiO_2	Al_2O_3	Fe_2O_3	MnO	MgO	CaO	Na_2O	K_2O	P_2O_5	Total	$CaCO_3$
149-898B-												
18R-3, 70–72	41.97	0.15	3.07	8.70	0.10	37.25	8.69	0.10	0.00	0.06	100.06	13.00
18R-4, 74–76	44.65	0.13	2.72	9.03	0.10	41.47	1.79	0.10	0.00	0.06	100.02	2.40
24R-3, 75–78	44.34	0.14	3.03	10.50	0.12	40.14	1.91	0.10	0.00	0.05	100.31	2.30

Table 8. Trace element composition of 21 samples from the top of the Upper Breccia Unit, Subunit IVA, Hole 899B.

Core, section, interval (cm)	Depth (mbsf)	Nb	Zr	Y	Sr	Rb	Zn	Cu	Ni	Cr	V	TiO_2	Ba	$CaCO_3$
149-899B-														
16R-1, 76–78	370.56	15	46	4	61	13	273	48	2199	4164	135	4511	18	0.80
16R-3, 73–75	373.12	11	14	1	55	7	72	8	1178	2157	53	1013	71	50.90
17R-1, 82–84	380.22	12	16	1	49	6	68	7	1668	1929	59	1695	47	30.10
17R-3, 73–76	383.03	11	12	0	37	5	28	9	1712	1953	56	1080	32	20.60
18R-1, 74–76	389.84	13	15	2	79	7	53	3	1225	1748	68	1515	54	41.50
18R-3, 70–72	392.35	13	19	3	33	5	34	6	1812	1993	61	1555	11	13.00
18R-5, 73–75	394.97	13	14	0	50	5	18	3	1166	1152	37	975	46	28.40
19R-1, 78–81	399.08	13	14	2	22	5	29	4	1939	2116	53	1353	2	2.60
19R-3, 80–82	401.95	11	6	0	44	6	37	0	3096	2538	43	647	8	0.40
20R-1, 79–82	408.49	12	16	2	78	5	25	4	1836	2082	61	1689	8	8.70
20R-3, 74–76	411.33	13	16	2	25	6	28	5	1722	1976	53	1713	9	1.70
21R-1, 70–73	417.80	12	17	1	58	6	28	12	1615	1734	50	1365	19	10.70
21R-3, 72–75	420.20	12	17	2	23	5	31	3	1575	2014	57	1454	14	6.60
21R-5, 78–81	423.20	12	5	0	5	5	36	0	2429	1990	35	428	12	0.50
22R-1, 59–62	426.89	13	15	1	16	6	29	0	1774	1894	57	1480	12	3.20
23R-1, 74–76	436.34	13	18	1	15	5	29	0	1868	2031	54	1417	5	2.40
23R-3, 66–72	439.14	13	17	2	14	6	30	3	1937	1922	53	1484	6	1.20
24R-1, 64–67	445.94	11	5	0	50	6	20	0	1876	1804	47	465	50	28.50
24R-3, 75–78	449.01	12	15	2	20	6	32	3	1829	2135	52	1431	12	2.30
25R-3, 73–76	458.20	13	20	1	17	5	33	4	1823	2478	49	1345	14	3.40
26R-1, 65–68	464.85	12	8	2	20	6	40	6	2359	1810	69	1374	12	0.40
Mean bulk composition (n = 21)		12	15	1	37	6	46	6	1840	2077	57	1428	22	
Mean bulk composition of noncarbonated serpentinite samples from Hole 897D (n = 18)		12	14	2	32	6	29	4	1839	1940	55	1387	6	

19R-2, 5-15 cm; -24R-3, 100-108 cm; -27R-1, 142-150 cm; -28R-1, 55-65 cm). Pyroxenite also was often observed as zones (0.4->2 cm thick) within individual clasts (e.g., Intervals 149-899B-29R-1, 110-130 cm, and -30R-1, 20-50 cm).

2. Banded peridotite, which displays alternating pyroxene- and olivine-rich bands, crosscut by numerous serpentine and calcite veins (Section 149-899B-19R-3; Interval 149-899B-19R-4, 0-75 cm);

3. Plagioclase-bearing peridotite in which spinel crystals are rimmed by a white alteration product of plagioclase (e.g., Interval 149-899B-20R-2, 32-50 cm; Fig. 15).

4. Dunite, associated with the boundary of the pyroxenitic zones, or occurring in bands within pyroxene-bearing areas (e.g., Section 149-899B-30R-2).

5. Deformed serpentinized peridotite, with a well-marked foliation in the serpentine mesh texture (e.g., Intervals 149-899B-18R-4, 57-63 cm; -19R-4, 130-140 cm; -20R-4, 90-100 cm; and -22R-2, 15-45 cm).

Weakly deformed peridotites are the most frequent lithology. They display coarse-grained textures and are serpentinized, with the mesh structure appearing more fine-grained in serpentinized dunites. The only primary mineral remaining is spinel. In places (e.g., Section 149-899B-19R-2), clasts are composed of highly deformed serpentinite with porphyroclastic to mylonitic textures. Some former olivine-rich bands have been replaced by fine mesh serpentinite. Elsewhere, colorless fibrous amphibole has replaced orthopyroxenes and chlorite has formed within magnetite- and spinel-rich zones. Pumpellyite-rich zones may represent former clinopyroxene. Similar retrograde metamorphic assemblages were observed in Subunit IVB (Interval 149-899B-29R-1, 129-132 cm) in an undeformed former clinopyroxenite band that crosscut serpentinized dunites. These metamorphic replacements are not homogeneously distributed for, in places, the texture and mineralogy have been obscured by later alteration and the rocks have a patchy pale gray color (e.g., Intervals 149-899B-19R-3, 0-15 cm; -20R-2, 13-21 cm; -21R-2, 50-95 cm; -28R-1, 103-112 cm; also Fig. 16). However, the original textures are recognizable.

In thin section, the smaller fragments are mostly serpentinite clasts. Discrete, scattered magnetite, pyroxene, and brown-spinel crystals also occur and represent remnants of unserpentinized peridotites.

Thin sections of pebble- to sand-sized clasts display well-crystallized serpentine (clear areas with uniform extinction). Other areas of serpentine are cloudy and are made of short crystals. Both well-crystallized and cloudy serpentine may coexist in a single fragment and seem to be, respectively, recrystallized and "relict" serpentine. A third type of serpentine has large crystals (up to 2.5 mm) with an obvious and regular cleavage (lizardite derived from bastite?). These crystals often are bent and/or crosscut by the most recent serpentinite crystallization event, which produced the clear serpentine (Interval 149-899B-21R-5, 32-36 cm).

One section contains what appear to be small sedimentary particles (Interval 149-899B-26R-1, 30-34 cm). These fragments, with sizes between 0.2 to 1.8 mm, have very fine-grained dusty cores rimmed by clear zones, 0.05 to 0.1 mm thick, that resemble serpentine. Other more angular fragments, classified as serpentinite in plane

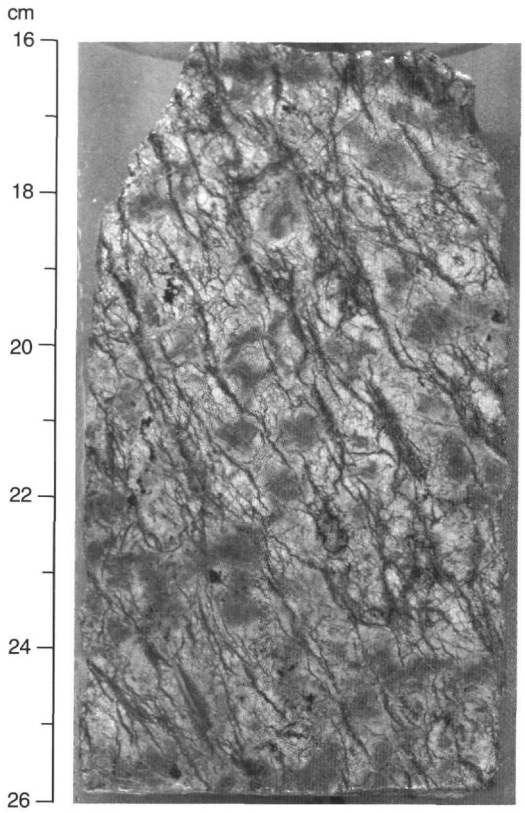

Figure 14. Single large serpentinite clast cut by roughly parallel fractures filled with serpentine. Alteration has produced the typical light gray-dark gray mottled serpentinite pattern (Upper Breccia Unit, Subunit IVA; Interval 149-899B-17R-1, 16-26 cm).

polarized light, are isotropic. A few fine-grained clasts of serpentinite display the characteristic fabric of mylonitized serpentinite (Interval 149-899B-20R-3, 50-53 cm).

Metamorphic Clasts

Shipboard examination of the breccias failed to identify any fragments of continental basement, and no clasts containing quartz were recovered. Only one 2-cm feldspar-bearing clast was found. It shows porphyroclastic feldspar, granulated epidote, a brown mica, and zircon. The type of feldspar is unclear and needs further study.

The most common metamorphic clast type found in the breccia unit is gray to white (rarely pink and green), very fine-grained, and displays no preferred mineral orientation (Fig. 17). Some clasts have been crosscut by veinlets restricted to the clast or extending into the matrix, the blocks may be fractured and the pieces slightly displaced (Interval 149-899B-20R-3, 43-52 cm). These fine-grained clasts appear to be low-grade metamorphic Mg- and/or Ca-rich rocks. Few of them have an intersertal texture. The clasts display several mineral associations, which may be grouped as follows:

1. Chlorite + magnetite ± sphene. In these rocks, the chlorite, which may constitute 90% of the rock, has crystallized without any preferred orientation. It displays deep blue anomalous birefringence under crossed-polars, unlike the normal silvery chlorite that occurs frequently in these serpentinites (Interval 149-899B-16R-2, 87-91 cm).
2. Talc. This mineral dominates in distinctive white and soft clasts. It may be accompanied by fibrous amphibole or by chlorite and, in the

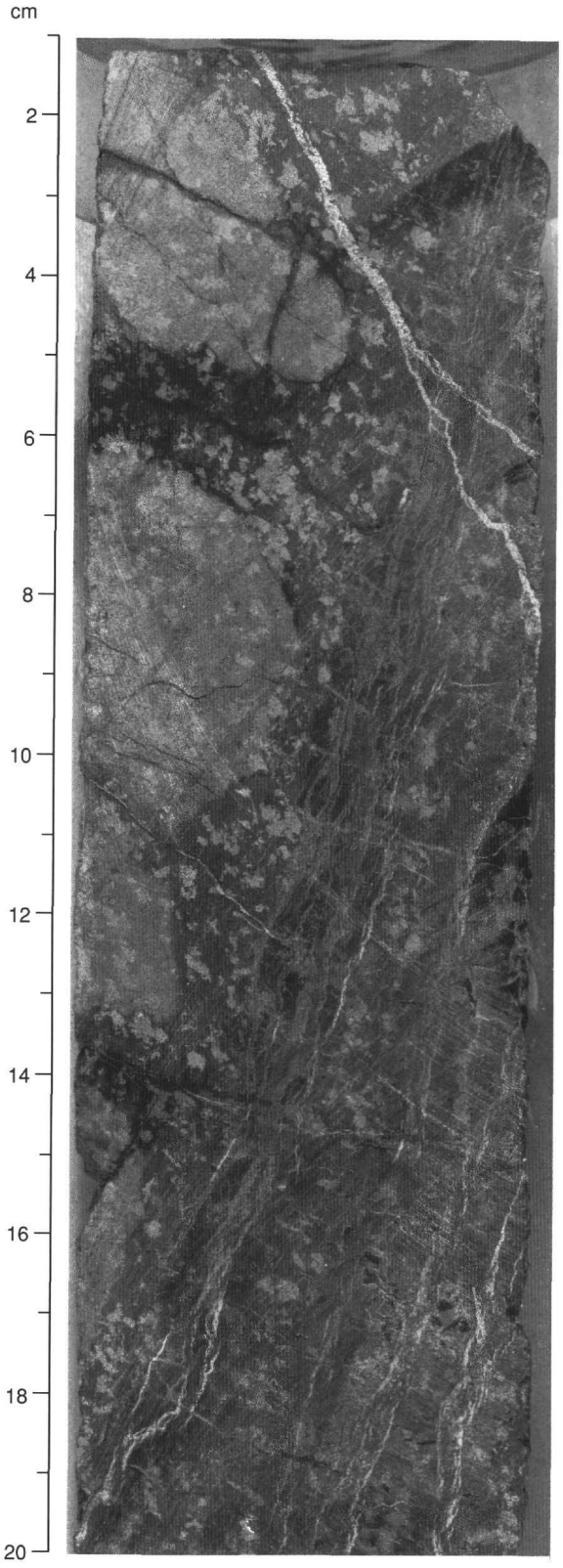

Figure 15. Boulder of banded serpentinized peridotite in Upper Breccia Unit, Subunit IVA (Interval 149-899B-19R-3, 1-20 cm). The dark layers are dunitic bands where discontinuous thin veins of white serpentine have been concentrated. In the upper left part of the core, the serpentinized peridotite has been locally obscured in white patches.

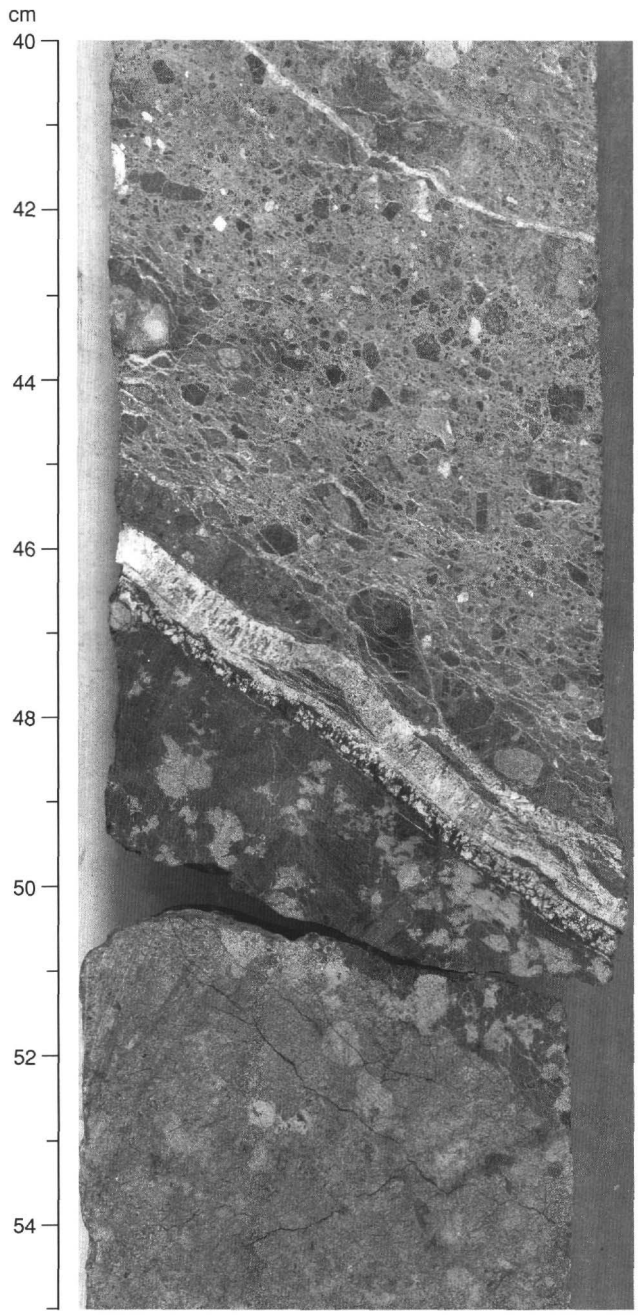

Figure 16. Large serpentinite clast with "ghostlike" crystals separated from the finer breccia matrix by a wide, composite vein at the clast margin. Thin anastomosing calcite veins also occur in the adjacent finer-grained breccia. Except along the boundary, peridotite in the serpentinite clast has been obscured by lighter colored serpentine (Upper Breccia Unit, Subunit IVA; Interval 149-899B-21R-2, 40-55 cm).

latter case, the clast is typically complex with distinct areas for each mineral. The great ductility of talc explains the contorted foliation displayed in many of these clasts (Interval 149-899B-20R-2, 90-95 cm).

3. Chlorite + epidote + fibrous amphibole. No foliation is noticeable. The chlorite displays anomalous light brown birefringence under crossed-polars, sometimes with a variety showing anomalous blue birefringence. The amphibole may be tremolite or actinolite.

4. Chlorite + pumpellyite + prehnite + fibrous amphibole. Larger crystals of the amphibole (1 by 0.2 mm) are prismatic and display a faint pale brown color.

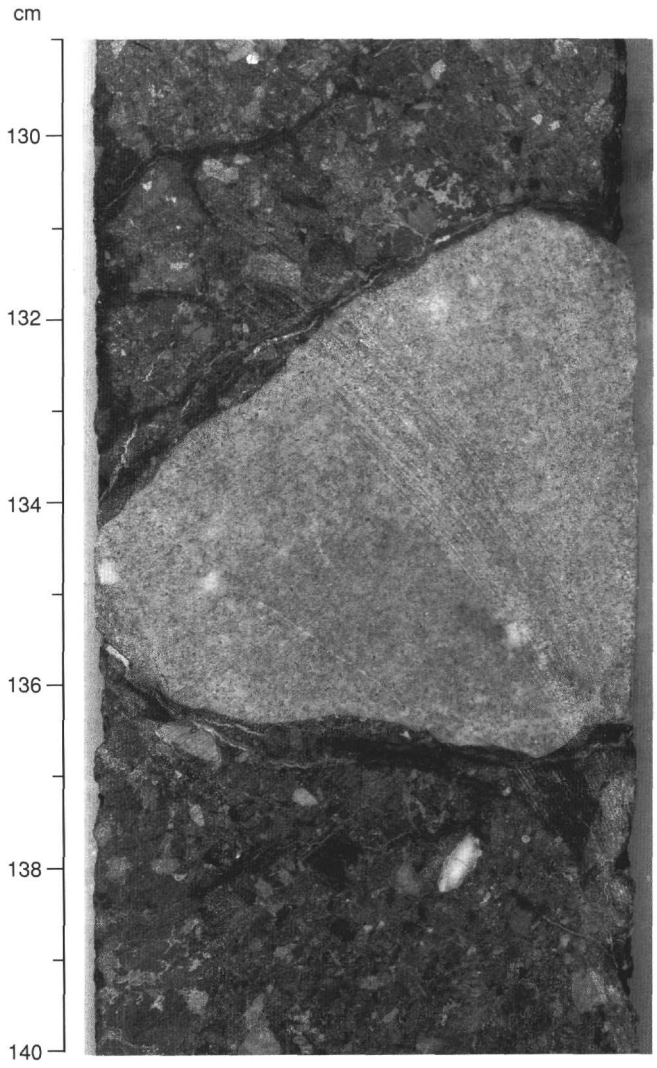

Figure 17. Large clast of light gray, metamorphosed, Mg-rich igneous rock with fine-grained structureless fabric surrounded by darker breccia matrix. Saw marks are visible on the surface of the clast (Upper Breccia Unit, Subunit IVA; Interval 149-899B-20R-1, 129-140 cm).

5. Chlorite (with blue or white anomalous birefringence) + pumpellyite + zoisite + sphene. The two latter minerals may be associated in zoned clasts that are pink (zoisite) and green (pumpellyite, amphibole, chlorite, and pumpellyite alone). A few serpentine and prehnite patches also may occur in these clasts (Interval 149-899B-23R-3, 117-120 cm).

Discussion of Emplacement and Origin of the Breccia Units

Several features of the breccia units constrain potential models for the mode of emplacement of the breccia. Some of the more important of these features are the composition, texture, structure, and stratigraphic framework. These aspects of the units are discussed here with a view to identifying the processes leading to the formation of the units and their origin.

The serpentinite bulk composition of the breccia units significantly constrains their mode of origin. Possible basaltic and microgabbroic rocks are also present among the metamorphic clasts. They are identified by their unmodified texture. No fragments of sedimentary rocks, pelitic metamorphic rock, or granitic clasts are included.

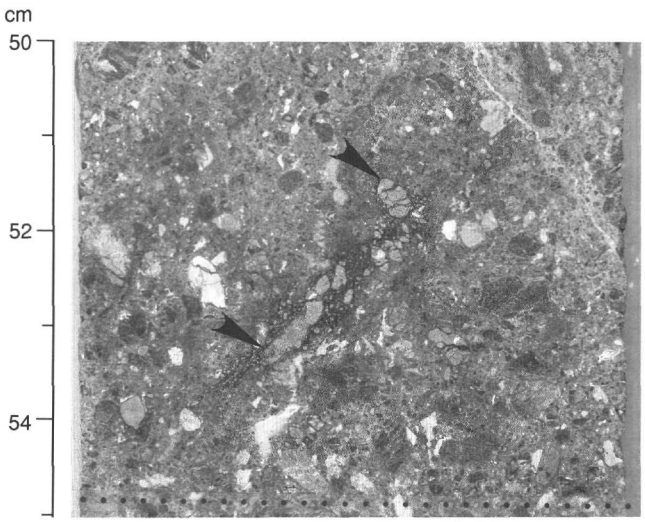

Figure 18. Partially disintegrated breccia clast (between arrows; Upper Breccia Unit, Subunit IVA; Interval 149-899B-26R-1, 50-55 cm).

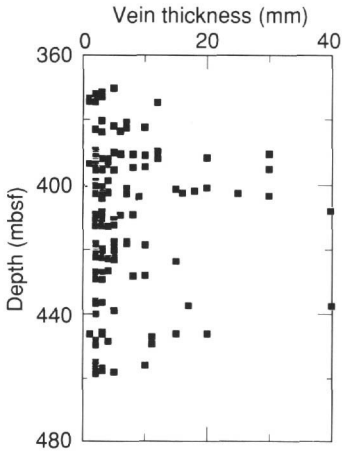

Figure 19. Distribution and size of calcite veins in the Upper Breccia Unit, Subunit IVA, Hole 899B.

As noted above, most of the clasts and boulder-sized blocks within the breccia units are serpentinized peridotite. The small fraction of the clasts (<10%) that are metamorphic contain a mineral assemblage characteristic of the prehnite-pumpellyite facies. Any model for the origin of the breccias must generate this specific mineral assemblage.

Texture is a striking feature of these breccias. Initial shipboard studies suggested that the fragments range in size from submicroscopic to boulder-sized blocks. All the smaller (1-20 mm) and microscopic (<l mm) clasts appear to be angular; and there is complete size gradation between "clasts" and "matrix" that makes this distinction arbitrary. Examples of fragments that appear to have been broken and granulated into elongated ribbons are common and visible at both the hand-specimen and microscopic scale (Fig. 18). Textures of this type are not characteristic of normal sedimentary mass flows, while volcaniclastic, submarine ash flows of this composition are very rare.

A third general feature of the unit is the overall absence of structure and sorting within the breccia. Within the Upper Breccia Unit, only a very few examples of a primary planar fabric were seen (e.g., penetrative deformation, zone of sorting, and so forth) that crosses the core. Most examples were short, discontinuous shear zones related to the margins of boulder-sized blocks (Fig. 16; see "Structural Geology" section, this chapter). However, a weak, irregular penetrative shear fabric within the breccia was observed in places at the top and base of the Upper Breccia Unit and the base of the Lower Breccia Unit. Overall, the breccia units are best described as unsorted and without planar structures (but see "Structural Geology" section, this chapter). We interpret this as indicating essentially instantaneous formation of each of the three breccia units.

The stratigraphic framework presented above (Fig. 11, back-pocket figure) also significantly constrains the origin of the breccias. The sequence of biostratigraphic ages of intercalated fine-grained sediments within Unit IV (Tables 2 and 3; Fig. 11, back-pocket figure) suggests a normal stratigraphic succession. It is for this reason that the Lower Breccia Unit may be considered the oldest of the three tabular breccias. Any tectonic model for the origin and emplacement of the breccias must generate this apparent stratigraphy.

Finally, low temperatures of emplacement/formation for the breccia units are indicated by the absence of thermal metamorphism in the underlying sediments (see below). Certainly, the bases of the breccias were never exposed to elevated temperatures (? 50°>100°C). The center of the thicker, Upper Breccia Unit might have reached higher temperatures without affecting the adjacent sediments, but no evidence is seen that the clasts themselves have been altered by post-emplacement thermal metamorphism. The clasts are not welded together, and the Upper Breccia Unit displays none of the welding features characteristically developed following the emplacement of hot ash flows.

In conclusion, the observations outlined here significantly constrain models for the emplacement of the breccias. Tentatively, we assume that the three breccia units are some form of mass-flow deposit, laid down in a subaqueous environment. However, the origin of the fragmentation that generated the clasts remains obscure.

Post-emplacement Alteration

All three breccia units show clear evidence of significant post-emplacement alteration. The two most obvious features resulting from this alteration are the color variation within the Upper Breccia Unit and the calcite veining of all three units. These two features are associated and, in the case of the upper unit, are related to large-scale chemical changes in the bulk composition.

Color changes are obvious only in the Upper Breccia Unit. The finer-grained matrix of this unit is predominantly dark yellowish brown (10YR 4/2) to moderate yellowish brown (10YR 5/4) in its upper part (Cores 149-899B-16R and -17R; Table 6). However, the recovered rocks from Core 149-899B-18R are darker (10YR 2/2) and gradually become dark green/gray or gray (N4) toward the base. Rocks from the lower parts of the unit (Cores 149-899B-20R through -26R) generally are dark green (5GY4/1) or greenish black (5G 2/1), with only short brownish sections (e.g., Sections 149-899B-20R-1 and -21R-2). While these color variations generally are gradational, only at 47 cm in Section 149-899B-25R-3 is there a sharp boundary between a medium gray and a medium light gray matrix. The sharpness of this boundary and the fact that it crosses a clast and displays no relationship to other primary features of the breccia demonstrate clearly the post-emplacement nature of the alteration.

Calcite alteration, perhaps reflecting a combination of veining and replacement, is more pervasive in the upper part of the Upper Breccia Unit (Cores 149-899B-16R and -17R; Figs. 19 and 20). Large-scale features that are clearly the result of replacement by calcite are absent, but in thin section, both vein filling and possible replacement fabrics are apparent. Calcite veins (Table 9; Fig. 19), broadly distributed in Cores 149-899B-18R through -25R, exhibit a slight tendency toward greater abundance in the central part of the Upper Breccia Unit. The larger veins (>1 cm wide) often occur as part of multivein complexes at the borders of boulder-sized serpentinite pieces, which are themselves more abundant in the central part of the Upper Breccia Unit (Fig. 13). These boulders may have generated a ductility contrast that facili-

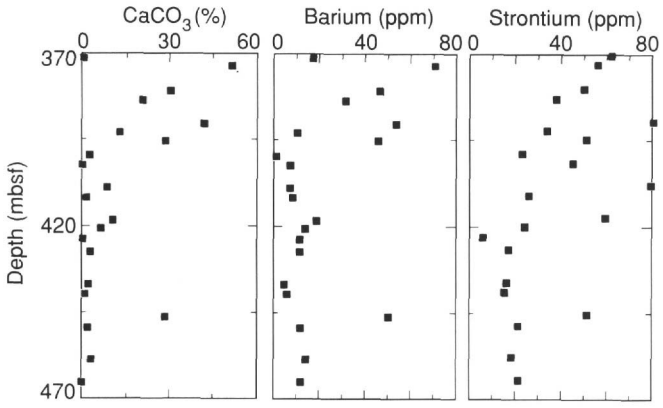

Figure 20. Whole-rock carbonate, Ba, and Sr concentration data vs. depth, Upper Breccia Unit, Subunit IV, Hole 899B.

tated veining. Some of these larger veins contain fibrous serpentine, which suggests that they have replaced or overprinted a previous serpentine-veining event (e.g., Interval 149-899B-18R-5, 58-62 cm). The larger veins show clear evidence of multiple stages of vein filling, and cross-cutting relationships can be observed in some intervals (e.g., Interval 149-899B-18R-5, 60-65 cm). Smaller veins (<1 mm), apparently spawned by the larger veins, are widely distributed throughout the upper part of the unit and typically form an anastomosing network.

The calcite veining (Fig. 19) clearly post-dates the emplacement of the Upper Breccia Unit and is among the youngest events modifying the Upper Breccia Unit, because veins clearly transect clast boundaries. Only very rare veins of a fine-grained brownish material were seen cutting the set of calcite veins (Interval 149-899B-16R-2, 66-78 cm).

Bulk chemical analysis of 21 samples from the Upper Breccia Unit (Table 8; Fig. 20) confirm that the upper part of the unit is indeed enriched in $CaCO_3$. This enrichment is particularly marked in samples from Cores 149-899B-16R and -17R. Below Core 149-899B-18R, calcite alteration is much more unevenly distributed, and only limited zones have been pervasively altered.

Data for Sr and Ba show that these two elements are also significantly enriched in the upper part of the Upper Breccia Unit, with the enrichment being clearly related to the calcite alteration (Table 8 and Fig. 20). Conversely, elements such as Ni and Cr, abundant in the unaltered breccia, have been depleted in the altered zone.

At this preliminary stage, the alteration has been ascribed to interaction with circulating seawater during the period immediately following the emplacement of the unit. This alteration follows a similar pattern to that observed in the upper part of the massive, serpentinized peridotite recovered from Hole 897C.

Basalts, Diabases, and Microgabbros

Basalts occur in close association with the sedimentary lithologies in Unit IV. Basalts are present as isolated pebble- to cobble-sized pieces; they are rounded pebble-sized pieces within claystone and calcareous claystone (Table 10). Most of the basalts have no vesicles. Other basalts have vesicles filled with a white, fine-grained chlorite or a pink mineral, probably calcite. Undeformed pieces of microgabbro (or coarse dolerite) are present (Intervals 149-899B-34R-1, 37-72 cm; -35R-1, 0-60 cm). These rocks have an intergranular texture with plagioclase laths (2.6 mm long) and euhedral altered olivine. Although mylonites occur in Interval 149-899B-34R-1, 0-37 cm, and although some of these may be mylonitized microgabbros, although the only analyzed sample is not, most of the fine-grained mafic igneous rocks from this site have not been deformed.

The first occurrence of basaltic rocks is in Section 149-899B-26R-1 (Fig. 21). This piece is distinctly brecciated and has been interpreted

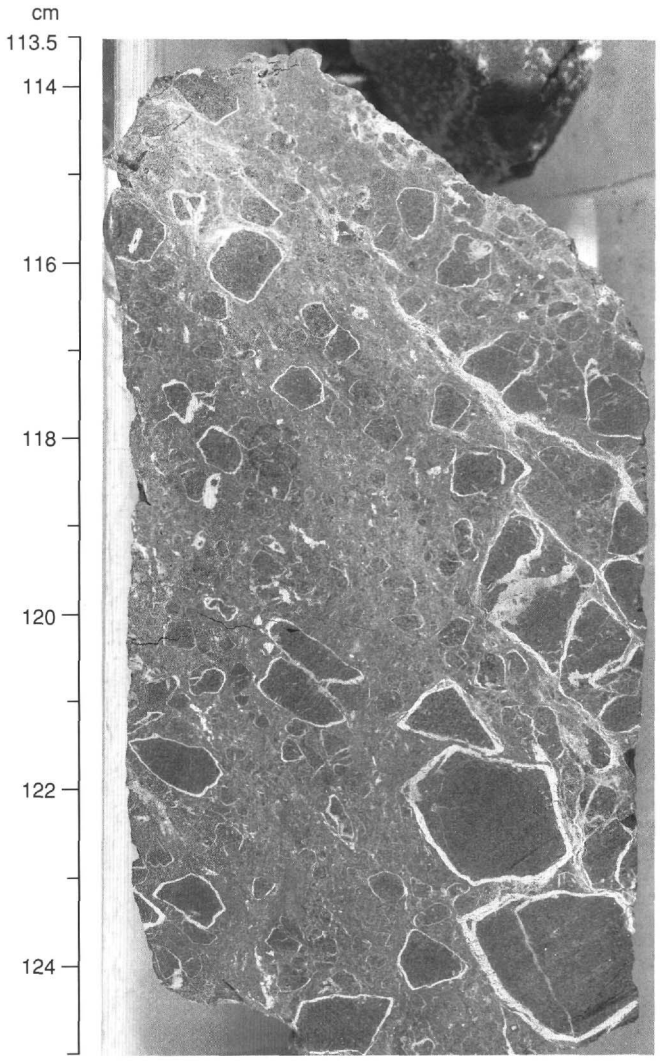

Figure 21. Basaltic breccia (?hyaloclastite) with individual clasts surrounded by light-colored vein material. Individual clasts consist of similar basaltic material without vesicles or phenocrysts. Alteration has destroyed most of the primary mineralogy (Subunit IVB, Hole 899B; Interval 149-899B-26R-1, 113.5-125 cm).

as an autobrecciated lava unrelated to the serpentinite breccia units. Dark and fine-grained fragments of basalt (up to 2 cm), outlined by thin white veins, are dispersed in a dark matrix having flow texture similar to that of the included fragments. The fragments are rimmed by chlorite (0.2-1 mm thick). The shape of the breccia fragments is not well defined, as the basalt has been highly altered. Nearly all of the plagioclase and glass have been replaced by chlorite and smectite. Similar basalts were found in Interval 149-899B-28R-2, 8-10 cm. The basalt recovered from Section 149-899B-27R-1, 19-20 cm, is porphyritic, with about 20% relatively unaltered plagioclase phenocrysts. Olivine phenocrysts, replaced by chlorite or serpentine, also are present. Two other basalt pieces exhibit variolitic texture (e.g., Interval 149-899B-31R-1, 9-14 cm). This mode of crystallization and the alteration of these rocks clearly suggest that these are pieces of submarine lavas.

Table 9. Distribution of calcite veins in the Upper Breccia Unit, Subunit IVA, Hole 899B.

Vein no.	Core, section, interval (cm)	Depth (mbsf)	Thickness (mm)	Comments
	149-899B-			
1	16R-1, 30–35	370.1	5	
2	16R-2, 17–22	371.3	3	
3	16R-2, 17–22	371.3	3	Veins 2 and 3 occur together in Piece 1.
4	16R-2, 70–72	371.8	2	2-mm calcite vein cut and offset by 1-mm goethite vein.
5	16R-2, 117–120	372.3	2	
6	16R-3, 23–25	372.6	3	
7	16R-4, 5–15	373.2	1	Network of veins at clast boundary.
8	16R-4, 65–70	373.8	1	
9	16R-4, 98–108	374.2	1	
10	16R-4, 113–117	374.3	2	
11	16R-4, 135–142	374.5	12	Thick vein at border of piece.
12	17R-1, 77–82	380.2	3	
13	17R-1, 128–129	380.7	7	
14	17R-2, 90–95	381.7	5	Calcite cutting earlier (?)serpentine vein.
15	17R-2, 128–130	382.1	10	At piece edge.
16	17R-2, 135–138	382.2	7	At piece edge.
17	17R-3, 26–30	382.6	2	
18	17R-3, 35–39	382.7	2	
19	17R-3, 83–87	383.1	6	At piece edge.
20	17R-3, 122–130	383.5	3	Irregular.
21	18R-1, 8–10	389.2	2	
22	18R-1, 14–16	389.2	2	
23	18R-1, 26–30	389.4	5	
24	18R-1, 30–32	389.4	12	
25	18R-1, 47–50	389.6	5	
26	18R-1, 59–61	389.7	5	
27	18R-1, 97–105	390.1	6	Irregular.
28	18R-2, 1–2	390.2	8	
29	18R-2, 2–10	390.2	30	
30	18R-2, 10–19	390.3	2	
31	18R-2, 22–45	390.4	2	Several small veins.
32	18R-2, 42–46	390.6	10	At piece edge.
33	18R-2, 61–65	390.8	2	
34	18R-2, 74–76	390.9	2	
35	18R-2, 82–89	391.0	2	
36	18R-2, 113–119	391.3	20	This large vein also cuts the next two lower pieces.
37	18R-2, 131–138	391.5	12	
38	18R-2, 137–138	391.6	4	
39	18R-2, 139–143	391.6	3	
40	18R-3, 76–81	392.4	2	
41	18R-3, 83–94	392.5	2	Several small veins.
42	18R-3, 128–132	392.9	2	
43	18R-3, 133–137	393.0	1	
44	18R-3, 142–147	393.1	2	
45	18R-4, 4–5	393.2	2	
46	18R-4, 7–9	393.2	2	
47	18R-4, 9–13	393.2	4	
48	18R-4, 13–15	393.3	2	
49	18R-4, 14–22	393.3	2	Very irregular.
50	18R-4, 63–64	393.8	2	
51	18R-4, 100–106	394.1	10	
52	18R-4, 109–111	394.2	8	Truncated at piece edge. Continues in Section 5(?).
53	18R-5, 2–7	394.3	2	
54	18R-5, 19–21	394.4	2	
55	18R-5, 23–26	394.5	2	
56	18R-5, 26–26	394.5	2	
57	18R-5, 33–37	394.6	3	Irregular.
58	18R-5, 37–48	394.6	3	
59	18R-5, 50–53	394.7	5	
60	18R-5, 58–64	394.8	30	Large complex vein.
61	18R-5, 72–73	395.0	3	
62	18R-5, 75–76	395.0	5	
63	18R-5, 75–85	395.0	2	Surrounds clast.
64	19R-1, 5–12	398.4	4	
65	19R-1, 22–28	398.5	2	
66	19R-1, 46–47	398.8	2	At piece edge.
67	19R-1, 124–126	399.5	2	Several small veins.
68	19R-1, 132–135	399.6	2	
69	19R-1, 138–140	399.7	2	
70	19R-2, 2–10	399.7	2	
71	19R-2, 25–27	400.0	2	
72	19R-2, 41–43	400.1	3	At piece edge.
73	19R-2, 87–97	400.6	20	Complex of many approximately parallel veins.
74	19R-2, 100–104	400.7	7	One large and several smaller veins. May be part of vein 73.
75	19R-2, 109–117	400.8	2	Several small veins.
76	19R-2, 132–135	401.0	15	Multivein complex.
77	19R-3, 2–10	401.2	2	
78	19R-3, 32–50	401.5	18	Complex of many veins.
79	19R-3, 57–59	401.7	4	Very irregular.
80	19R-3, 87–88	402.0	2	
81	19R-3, 88–89	402.0	3	
82	19R-3, 93–94	402.1	4	
83	19R-3, 95–96	402.1	2	
84	19R-3, 97–98	402.1	2	
85	19R-3, 100–102	402.2	3	Irregular.
86	19R-3, 102–103	402.2	2	Irregular.
87	19R-3, 104–108	402.2	16	Complex vein at edge of piece.

Table 9 (continued).

Vein no.	Core, section, interval (cm)	Depth (mbsf)	Thickness (mm)	Comments
88	19R-4, 0–2	402.2	2	
89	19R-4, 2–6	402.3	7	
90	19R-4, 6–8	402.3	25	Large zoned vein.
91	19R-4, 35–38	402.6	3	
92	19R-4, 41–44	402.7	3	
93	19R-4, 78–84	403.0	30	May be large irregulr patch, not a "vein."
94	19R-4, 84–90	403.1	30	May be part of vein 93.
95	19R-4, 93–96	403.2	9	
96	19R-4, 93–101	403.2	3	
97	19R-5, 7–16	403.7	3	
98	20R-1, 22–24	407.9	3	Parallels vein 99.
99	20R-1, 22–40	407.9	40	Complex zoned vein.
100	20R-1, 100–110	408.7	2	
101	20R-1, 113–114	408.8	2	
102	20R-1, 119–120	408.9	8	
103	20R-1, 121–126	408.9	6	
104	20R-2, 16–20	409.3	3	
105	20R-2, 75–80	409.9	2	
106	20R-2, 84–86	410.0	5	Vein at piece edge.
107	20R-2, 108–111	410.3	5	
108	20R-2, 126–127	410.4	2	
109	20R-3, 68–69	411.3	3	
110	20R-3, 111–112	411.7	5	
111	20R-4, 7–10	412.0	5	
112	20R-4, 27–40	412.2	2	
113	20R-4, 27–40	412.2	3	
114	20R-4, 45–46	412.4	4	
115	21R-1, 5–10	417.2	5	
116	21R-1, 5–11	417.2	7	
117	21R-1, 52–53	417.6	2	
118	21R-1, 54–55	417.6	7	
119	21R-1, 63–65	417.7	2	
120	21R-2, 0–5	418.2	10	Truncated at piece edge.
121	21R-2, 44–49	418.7	5	Vein complex at boulder-clast margin.
122	21R-3, 0–12	419.5	3	Vein complex.
123	21R-3, 35–50	419.8	5	Multiple vein, complex.
124	21R-3, 47–55	420.0	3	
125	21R-3, 84–85	420.3	2	
126	21R-3, 95–97	420.4	2	
127	21R-3, 96–97	420.4	2	
128	21R-3, 123–133	420.7	2	
129	21R-4, 10–15	421.1	2	
130	21R-4, 49–51	421.5	2	
131	21R-4, 90–96	421.9	2	In large pyroxenite block.
132	21R-4, 125–129	422.2	5	
133	21R-4, 130–133	422.3	3	
134	21R-5, 0–3	422.4	4	
135	21R-5, 49–56	422.9	5	
136	21R-5, 97–100	423.4	15	Vein complex on piece margin.
137	22R-1, 1–2	426.3	4	Piece edge.
138	22R-1, 27–32	426.6	2	In large serpentine vein.
139	22R-1, 34–38	426.6	2	
140	22R-1, 41–48	426.7	2	May be continuation of vein 139.
141	22R-1, 52–55	426.8	3	
142	22R-, 116–117	427.5	2	
143	22R-1, 137–140	427.7	2	
144	22R-2, 0–8	427.8	10	
145	22R-2, 10–23	427.9	8	May be continuous with vein 144 above.
146	22R-2, 70–74	428.5	2	
147	22R-2, 96–102	428.7	3	
148	22R-2, 108–113	428.8	2	
149	22R-2, 123–125	429.0	3	
150	23R-1, 15–17	435.8	2	
151	23R-1, 28–34	435.9	2	
152	23R-1, 49–54	436.1	3	
153	23R-1, 54–58	436.1	3	
154	23R-1, 71–76	436.3	2	
155	23R-2, 14–19	437.2	17	
156	23R-2, 19–38	437.2	40	Large vein at block boundary.
157	23R-3, 15–21	438.6	5	Complex vein.
158	23R-3, 130–133	439.8	2	
159	24R-1, 4–6	445.3	3	
160	24R-1, 57–60	445.9	3	
161	24R-1, 57–60	445.9	1	
162	24R-1, 60–63	445.9	15	
163	24R-1, 69–76	446.0	20	Vein complex.
164	24R-2, 7–10	446.9	11	
165	24R-, 117–122	448.0	2	
166	24R-3, 0–12	448.3	4	
167	24R-3, 12–20	448.4	2	
168	24R-3, 74–76	449.0	2	
169	24R-3, 86–93	449.1	11	
170	24R-3, 119–130	449.5	2	
171	25R-1, 7–10	454.8	2	
172	25R-1, 15–16	454.9	2	
173	25R-1, 67–80	455.4	2	
174	25R-1, 86–93	455.6	2	

Table 9 (continued).

Vein no.	Core, section, interval (cm)	Depth (mbsf)	Thickness (mm)	Comments
175	25R-1, 103–108	455.7	10	
176	25R-1, 109–114	455.8	2	
177	25R-2, 47–56	456.5	3	
178	25R-2, 70–74	456.7	2	
179	25R-2, 85–90	456.9	2	
180	25R-2, 85–90	456.9	3	
181	25R-2, 129–132	457.3	3	
182	25R-3, 16–20	457.6	2	
183	25R-3, 17–20	457.6	2	
184	25R-3, 26–27	457.7	5	
185	25R-3, 85–90	458.3	2	

Table 10. Occurrences of basalt in Unit IV, Hole 899B.

Core, section, interval (cm)	Comments
149-899B-	
26R-1, 90–93	Aphyric basalt with small round vesicles filled with pink calcite.
26R-1, 109–114	Aphyric basalt with small round vesicles filled with pink calcite.
27R-1, 11–18	Aphyric basalt with small spherical vesicles filled with white mineral.
27R-1, 18–33	Porphyritic basalt with 20% fresh plagioclase laths (3-8 mm). Small circular vesicles with a white mineral. Red iron stain.
27R-1, 33–40	Aphyric basalt with small irregular vesicles. Plagioclase and pyroxene are altered.
28R-2, 0–15	Aphyric basalt with relatively fresh plagioclase laths and olivine. Pyroxene is altered. No vesicles.
29R-1, 90–98	Aphyric basalt with weak plagioclase flow orientation. No vesicles and badly altered.
29R-1, 98–105	Amygdaloidal porphyritic basalt. Phenocrysts of plagioclase and olivine. Spherical vesicles filled with clays. Badly altered.
29R-1, 105–110	Diabase stained red from oxidation. Both plagioclase and pyroxene are badly altered.
29R-2, 7–12	Rounded aphyric basalt clast with an alteration rim and armored with a mud coating. Badly altered and free of vesicles.
29R-2, 12–16	Red oxidized aphyric basalt in clay/serpentine matrix. Badly altered throughout. Oxidized alteration rim. No vesicles.
29R-2, 18–22	Aphyric basalt with no vesicles and badly altered.
30R-1, 16–19	Diabase with 60% plagioclase laths and 40% pyroxene. Badly altered.
31R-1, 0–9	Aphyric basalt with very circular vesicles. No phenocrysts.
31R-1, 9–15	Variolitic basalt with radiating aggregates of plagioclase. Badly altered with no vesicles.
32R-1, 0–3	Feldspathic basalt.
33R-1, 7–12	Feldspathic basalt with 1% vesicles and acicular pyroxene. Badly altered clast in sediment.
33R-1, 17–20	Aphyric basalt with no vesicles and acicular pyroxene. Altered clast in sediment.
33R-1, 25–32	Diabase with 60% plagioclase and 40% pyroxene. Appears altered.
33R-1, 32–40	Aphyric basalt with circular filled vesicles. About 60% plagioclase laths and 40% pyroxene. Altered.
34R-1, 37–72	Diabase with 60% plagioclase and 40% pyroxene. Most minerals are altered.
35R-1, 0–61	Diabase with 60% plagioclase and 40% pyroxene. Contains serpentine veins cut by late red-brown breccia vein.
35R-1, 61–71	Epidotized microgabbro; 50% plagioclase and 50% altered mafic crystals. Altered to a greenish color and cut by thin calcite veins.
37R-1, 14–22	Diabase with 50% plagioclase and 50% pyroxene.

Table 11. Major elemental chemistry of three basalts and one diabase, Subunit IVB, Hole 899B.

Core, section, interval (cm)	Rock type	SiO_2	TiO_2	Al_2O_3	Fe_2O_3	MnO	MgO	CaO	Na_2O	K_2O	P_2O_5	Total	LOI
149-899B-													
27R-1, 12	Basalt	49.30	1.37	17.06	6.84	0.16	12.70	6.87	2.15	1.93	0.30	98.68	6.12
27R-12, 33	Basalt	48.93	2.01	14.24	9.76	0.22	16.38	1.96	2.64	2.12	0.37	98.63	6.30
28R-2, 10	Basalt	49.42	1.53	17.08	7.44	0.15	10.75	6.26	2.41	2.26	0.20	97.50	3.92
35R-1, 7	Diabase	50.27	0.92	19.54	8.42	0.14	11.72	1.33	0.77	5.67	0.09	98.87	7.44

Note: LOI = loss on ignition.

Only four samples in this unit (three basalts and one diabase) were analyzed for major elements (Table 11) and three for minor elements. The high loss-on-ignition indicates the highly altered nature of the analyzed rocks. The high magnesium content (16.4% MgO) of Sample 149-899B-27R-1, 33-40 cm, also may reflect alteration. All three basalts have high, but variable, values of K_2O, reflecting either alteration or a non-MORB-type composition, and the diabase (Sample 149-899B-35R-1, 7 cm) has a very high K_2O content (5.67%). The average nickel and chromium for two samples of basalt and microgabbro (Samples 149-899B-28R-2, 10-13 cm, and -35R-1, 7-11 cm; 154 and 230 ppm, respectively, for Ni and Cr) are normal for mafic rocks.

In summary, the basalts are extremely variable texturally, mineralogically, and compositionally, which precludes an interpretation that relates the pieces to a common origin. The variations among the basalts are consistent with the interpretation of these pieces as clasts.

Sedimentary Rocks in Unit IV

Four recurring sedimentary lithologies are present in cores beneath the Upper Breccia Unit (Fig. 11, backpocket figure; Table 12). These are intimately associated with the basalt pieces described above and also have been interspersed with the unbrecciated segments of

Table 12. Occurrence of sedimentary lithologies in Unit IV, Hole 899B.

Core, section, interval (cm)	Type	Lithology	Important constituents	Color	Age
26R -1, 82–87	1	Calcareous silty claystone	Nannofossils	N4	early Aptian
27R-1, 40–70	3	Calcareous claystone with cobble	Minor nannofossils, serpentine cobble	N3	Aptian
27R-1, 70–94	3	Clayey conglomerate	Serpentinite pebbles	N3 to N8	
27R-1, 94–102	*	Limestone with pebbles	Tr. nannofossils, serpentine pebbles	N8	
28R-1, Pc14	2	Claystone with pebbles	Pebbles: basalt and serpentinite	5Y 4/1	
28R-1, Pc14	1	Calcareous silty claystone	Nannofossils	N4	
28R-1, Pc17	2	Claystone		N4	
29R-1, Pc 3	2	Claystone		5G2/1	
29R-1, Pc 3	1	Calcareous claystone	Nannofossils	5G2/1	early Aptian
29R-1, 28–82	3	Clayey conglomerate	Serpentinite pebbles	5G 2/1	
29R-2, Pc 1	2	Claystone	Possibly armored pebble	5GY 4/1	
29R-2, 13–24	4	Serpentine sand? with pebbles	Basalt pebbles	N7	
29R-2, 24–32	*	Radiolarian chert (recrystallized)	Chalcedony veins	N7	
30R-1, Pc 2	2	Claystone		N4	
30R-2, 93–97	4	Serpentine sand?	Serpentinite granules	5G 2/1	
31R-2, 28–41	4	Serpentine sand? with cobbles	Cobbles of serpentinized peridotite	5G 2/1	
32R-1, Pc 8	2	Claystone		N4	Early Cretaceous
33R-1, Pc 2	1	Claystone with calcareous silt and pebbles	Basalt pebbles	N5	Early Cretaceous
33R-1, Pc 6	4	Serpentine sand? with pebbles	Basalt pebbles	5G 2/1	
35R-1, 79–96	4	Serpentine sand? with pebbles, cobble	Serpentinite cobble, basalt pebble	N3	
35R-1, 96–102	1	Calcareous claystone with pebbles	Basalt pebbles	N3	Barremian
35R-1, 102–123	*	Sandstone	Quartz and alkali feldspar	N6	
35R-1, 123–133	3	Claystone with cobbles?	Serpentinite, basalt cobbles?	N2	

Notes: Type: 1 = lithology "1" in text; Type: 2 = lithology "2" in text; Type:3 = lithology "3" in text; Type: 4 = lithology "4" in text; * = single occurrence.

serpentinite, serpentinized peridotite, mylonite, and gabbro. The sedimentary lithologies are as follows:

1. Calcareous claystones and calcareous silty claystones: carbonate, in the form of silt-sized fragments of subhedral monocrystalline and polycrystalline calcite, ranges from 20% to 40% in these rocks. Most of the ages determined for Unit IV (early Aptian to late Barremian; see "Biostratigraphy" section, this chapter) were obtained from these rocks. Two occurrences of this lithology contain basalt pebbles (e.g. Fig. 22, Interval 149-899B-35R-1, 96-102 cm). Drilling-induced mixing of the basalt pieces into the relatively unconsolidated clay may have occurred or, alternatively, the basalts may represent clasts native to the calcareous claystones.
2. Claystones: claystone with highly oriented clay minerals (Type 2, see definition in "Lithostratigraphy" section, "Site 897" chapter, this volume) is the most common sedimentary lithology in Unit IV. Some occurrences of this lithology also incorporate rounded fragments of basalt and/or serpentine.
3. Dark gray claystone and calcareous claystone with pebble- to cobble-sized serpentinite pieces: two, possibly three, occurrences of this lithology were observed. In this lithologic association, very dark (N3) claystone or calcareous claystone, with highly distorted laminations, contains masses of deformed and very soft serpentinite (Fig. 23). Intervals with pebble- to cobble-sized pieces of serpentinite with interstitial claystone (Intervals 149-899B-27R-1, 70-94 cm; -29R-1, 28-82 cm) may represent a coarser-grained end-member of this lithology (Fig. 24).
4. Masses composed of sand-sized serpentine: several intervals contain very unconsolidated serpentine that in smear slides appears to be made of sand-sized fragments (Fig. 25A). These fragments have a generally disturbed or foliated and sheared appearance in the core. Two occurrences of this lithology incorporate rounded basalt pieces and/or hard pieces of serpentinized peridotite, which resemble clasts (Figs. 25B and 22, Interval 149-899B-35R-1, 79-96 cm); however, drilling-induced mixing may have occurred here. The sedimentary nature of this lithology is problematic, but a general textural similarity can be seen to material documented as serpentine sediment (specifically, the "sheared phacoidal serpentine") in the arc-related complex of the Izu-Bonin/Mariana region (Fryer, Pearce, Stokking, et al., 1990).

Three other sedimentary lithologies occur only once each in Unit IV. One of these is a limestone (Interval 149-899B-27R-1, 94-103 cm) composed almost exclusively of loosely aggregated sand- and silt-sized, subhedral, monocrystalline and polycrystalline calcite. Poorly preserved nannofossils are present in minor amounts. Another lithology is that of a gray laminated siltstone with prominent soft-sediment faulting (e.g., Interval 149-899B-35R-1, 101-121 cm). This lithology is a striking compositional and textural contrast to the other sedimentary lithologies in Subunit IVB (Fig. 26). It is a subarkose (classification of Folk, 1980) and contains the only occurrence of greater-than-trace amounts of quartz and alkali feldspar below the base of Unit III. The third lithology is a black radiolarian(?) chert with veins filled by spherules of length-slow chalcedony (Interval 149-899B-29R-2, 24-32 cm; Fig. 25B). This chert is dark-colored because of a large amount (?10%) of opaque organic matter and pyrite. Allochems have been highly recrystallized, and their identification is problematic.

Comparison with Lithologic Unit IV at Site 897

At Site 897, no unit clearly analogous to the serpentinite breccia at Site 899 is well developed. Nevertheless, certain broad similarities can be identified between lithologic associations in Unit IV at the two sites (see "Site 897" chapter, this volume).

Except for the serpentinite breccias of Subunit IVA, all of the nonsedimentary lithologies observed in Unit IV at Site 899 are interpreted as clasts. Several lines of evidence support our contention that the basalt pieces, serpentinite, serpentinized peridotite, mylonite, gabbro, as well as some claystone, and the radiolarian chert represent sedimentary clasts of pebble to boulder size. The rounded shape of pieces within the claystones and apparent weathering rinds on some pieces support this interpretation. Several isolated rounded, pebble-sized clasts, most notably Section 149-899B-29R-2, Pieces 1 (claystone) and 2 (basalt with an apparent weathering rind; Fig. 26) are partially coated with a coherent layer of claystone that resembles armoring, which may have been acquired during repeated transport and deposition.

The intercalation of sedimentary lithologies with these intervals of nonsedimentary rock is the most obvious feature shared by sequences designated as Unit IV at Sites 897 and 899. The specific sedimentary lithologies present within Unit IV vary somewhat in their proportions, but several lithologies are common to both sites. Site 897 was characterized by a larger amount of calcareous material, including limestones. Ages obtained from nannofossils (late Hauterivian to late Aptian at Site 897, Barremian to early Aptian at Site 899) are similar at both sites and, in both cases, indicate a normally ordered sequence that gets younger upward. This supports the idea that the calcareous claystones, from which the ages were obtained, in some way may be

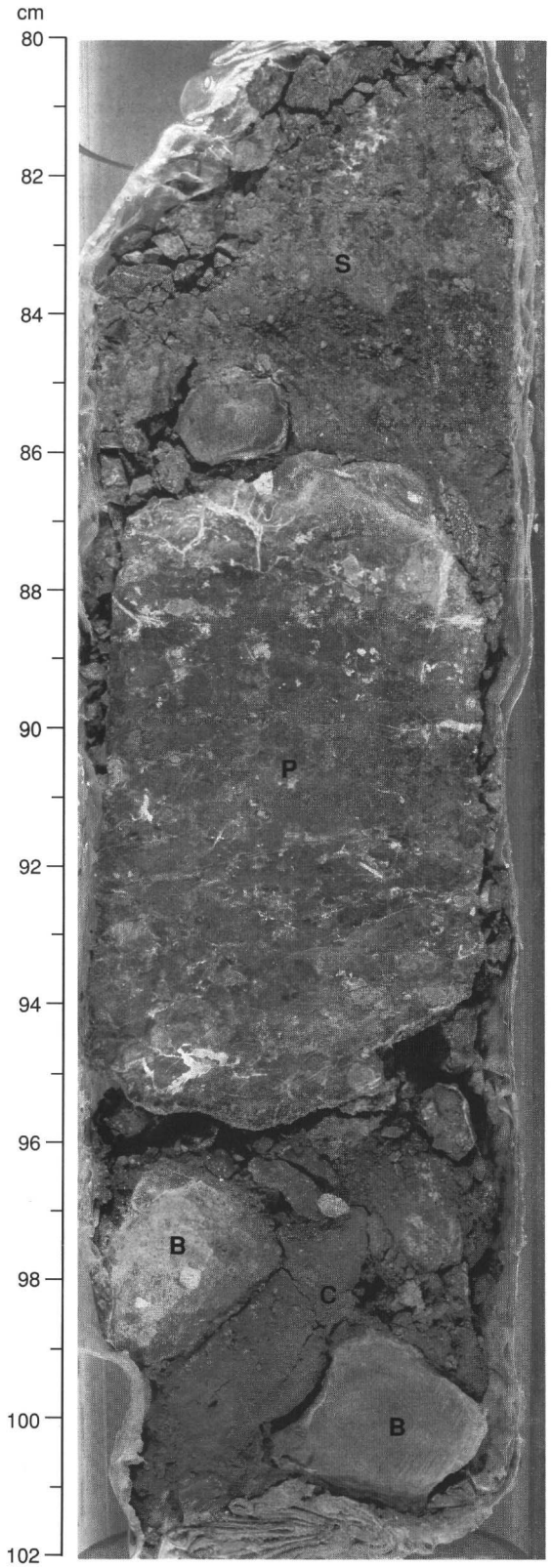

Figure 22. Diverse lithologies of Subunit IVB, Holes 899B. Soft, deformed sand-sized serpentine (S) and a cobble-size block of serpentinized peridotite (P) are seen in Interval 149-899B-35R-1, 80-96 cm. Calcareous claystone (C) with pebble of basalt (B)(?) (Interval 149-899B-35R-1, 96-102 cm) is the source of the deepest nannofossil date obtained at Site 899 (Barremian, see "Biostratigraphy" section, this chapter).

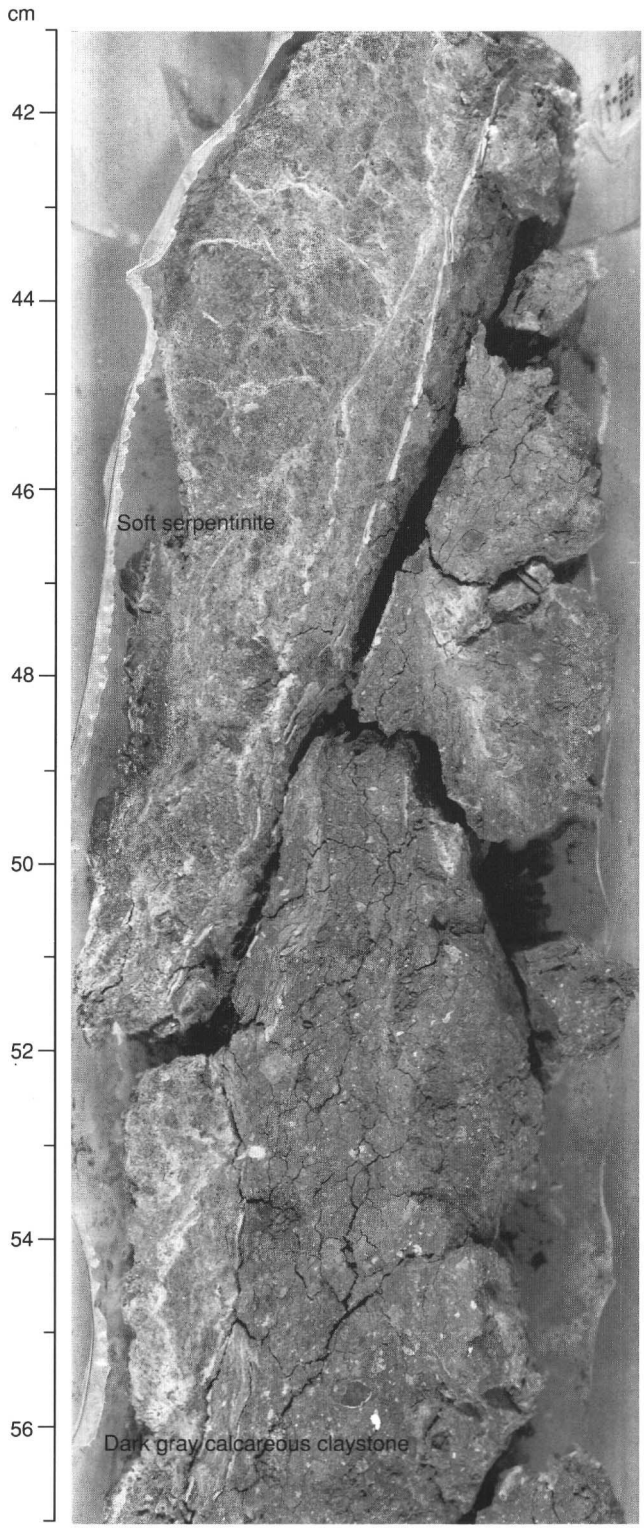

Figure 23. Highly deformed fragments of soft serpentinite in dark calcareous claystone. The serpentinite fragments contain light-colored veins that have been deformed and broken. (Described in text as sedimentary lithology "3"; Subunit IVA, Interval 149-899B-27R-1, 41-57 cm).

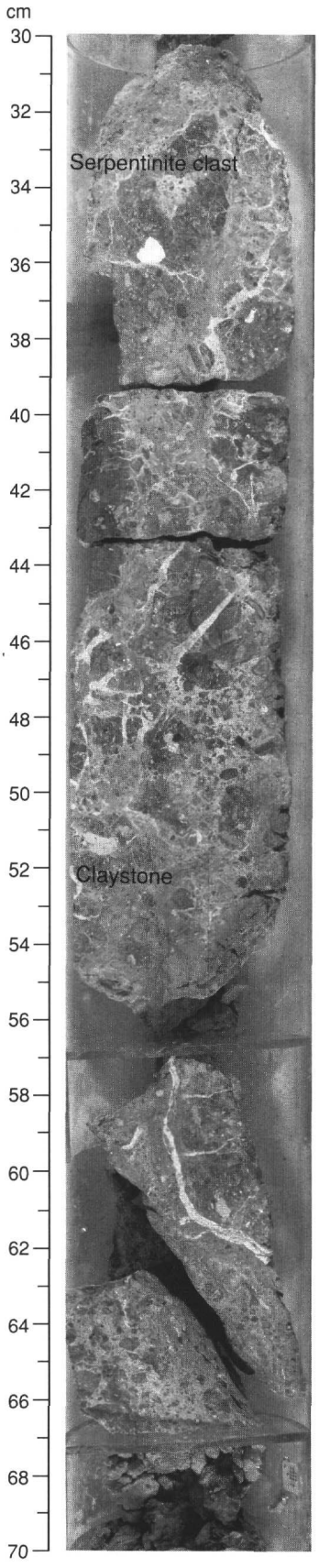

Figure 24. Semilithified, brecciated, and veined serpentinite fragments in a claystone matrix (Subunit IVB, Interval 149-899B-29R-1, 30-70 cm).

present in locally deposited sediments into which the clasts of nonsedimentary material were introduced.

Another recurrent sedimentary lithology in Unit IV is the highly deformed, dark gray, organic-rich mudstone associated with deformed serpentine masses. At Site 897, the Shipboard Scientific Party considered (see "Site 897" chapter, this volume) that this material might be the product of drilling disturbance. However, the distinctive organic content and age of this material strengthened the interpretation that it is sedimentary in origin.

The laminated, gray, subarkosic siltstone, which displays soft sediment deformation, also appears at both Sites 897 and 899. The great compositional contrast between this siltstone and the associated sediments supports the idea that it may represent a clast in a manner analogous to the basalt fragments. However, the laminations are subhorizontal, an orientation that is highly improbable for an allochthonous clast.

As with the breccia units, some variation of a mass flow origin is also proposed for the mixed assemblage of igneous and sedimentary lithologies that are found both intercalated between the breccia bodies in Unit IVA and in Unit IVB. Such an interpretation is drawn by analogy to Unit IV at Site 897 because of the similarities in lithologic types and associations observed in the Units IV between the two sites, exclusive of the serpentinite breccia (see "Site 897" chapter, this volume). Again, the presence of serpentinite and serpentinitized peridotite within an upward-facing sedimentary sequence would seem to indicate exposure of mantle-derived rocks to submarine weathering and transport, beginning at least as early as Barremian.

BIOSTRATIGRAPHY

Sediments recovered from the two holes cored at Site 899 provide a discontinuous record from upper Pliocene through Lower Cretaceous. Calcareous nannofossils generally are abundant to very abundant in all the Cenozoic sedimentary sequences and rare to abundant in the Early Cretaceous age sediments. Planktonic foraminifers generally are common to abundant in Hole 899A; however, samples from the deeper Hole 899B were barren or contained few planktonic foraminifers.

Calcareous Nannofossils

The two holes drilled at Site 899, located in the eastern part of the Iberia Abyssal Plain in a water depth of 5291 m, penetrated 562.5 m of sediment. Hole 899A was cored in the interval from 81.5 to 235.5 mbsf, with a total recovery of 51.45 m of sediment, whereas Hole 899B was cored in the interval from 230.5 to 562.5 mbsf, with a recovery of 173.41 m. The calcareous nannofossils define four stratigraphic successions within the Cenozoic sequence; one from the lower Pliocene (Zone NN16 of Martini, 1971) to the lower Pliocene (Zone NN15), a second from the uppermost Miocene (base Zone NN12) to the upper Miocene (Zone NN10), a third from the middle Miocene (NN7) to the lower Oligocene (NP23), and a fourth restricted to the upper Eocene (NP20). A major hiatus representing most of the Paleogene lies within Core 149-899B-15R. Below this level, recovered sediments are Cretaceous in age. Very thin intervals of Lower Cretaceous sediments occur in Cores 149-899B-26R to -37R; these are intercalated with a breccia composed mostly of serpentinized peridotite. This Lower Cretaceous interval corresponds to lithostratigraphic Subunit IVB (see "Lithostratigraphy and Petrology" section, this chapter).

The abundance and preservation of calcareous nannofossils at Site 899 correspond well with the major lithostratigraphic units. Sediments from Unit I (Cores 149-899A-1R to -6R) contain generally very abundant and well-preserved calcareous nannofossils. Unit II (Cores 149-899A-6R to -15R) contains abundant, moderately well-preserved calcareous nannofossils, with some intervals that are barren or contain poorly preserved calcareous nannofossils. Sediments

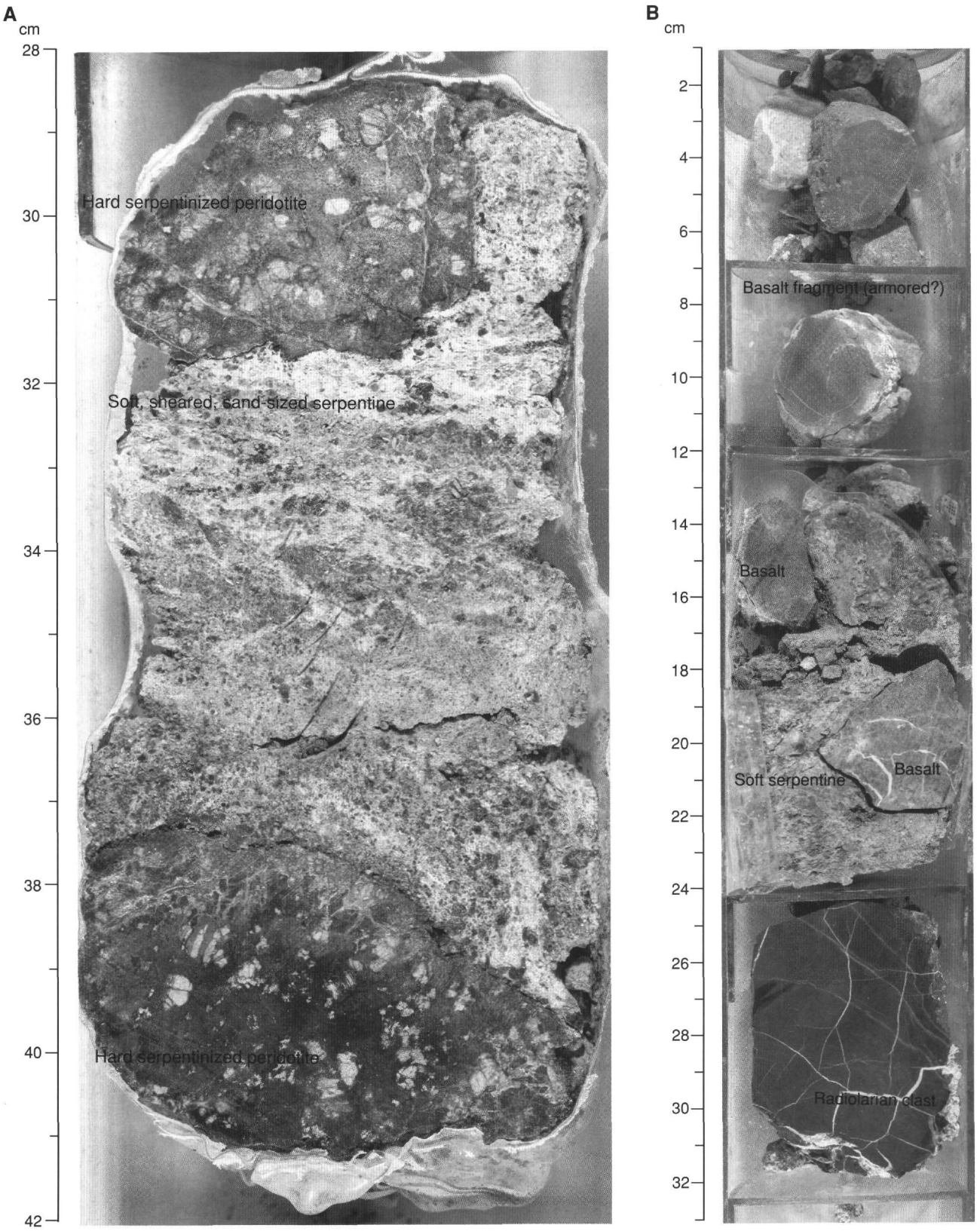

Figure 25. Examples of soft, granular serpentine masses (Subunit IVB, Hole 899B). **A.** Interval 149-899B-31R-2, 28-42 cm; two fragments of lithified serpentinite separated by unconsolidated sand-sized serpentinite with irregular laminations. The laminations are oriented in a manner consistent with compactional deformation of the softer material between the more lithified clasts. **B**. Interval 149-899B-29R-2, 1-33 cm; soft, sand-sized serpentine containing two rounded basalt pieces (arrows). Basalt at 7-12 cm may be armored with detrital clay. The dark rock in the lower portion of the pictured interval (24-32 cm) is a highly recrystallized radiolarian(?) chert with chalcedony-filled veins. Masses of pyrite are found on the back side of the chert clast.

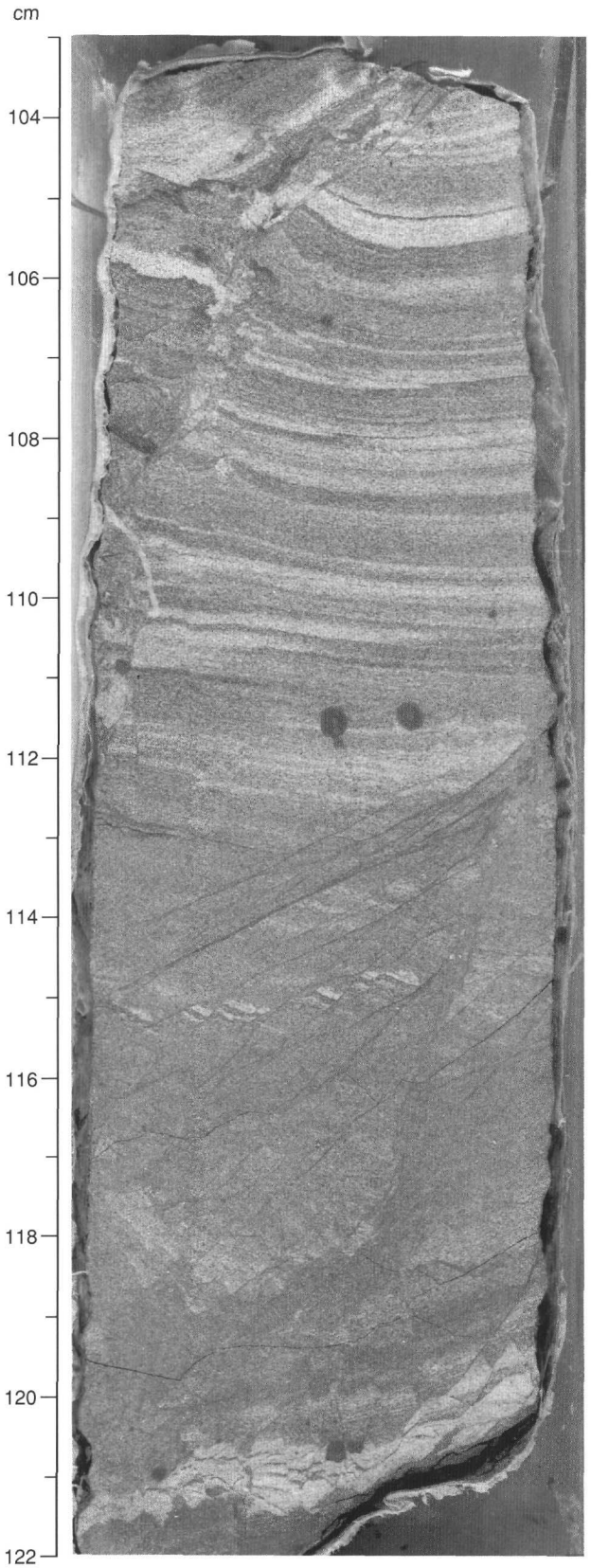

Figure 26. Laminated quartzose siltstone with fractures (Subunit IVB, Interval 149-899B-35R-1, 103-122 cm).

recovered from the top of Unit III to the upper part of Subunit IVA (Intervals 149-899B-15R to -25R) are barren of nannofossils. Finally, the lower part of Subunit IVA (Core 149-899B-26R through Section 149-899B-28R-1) and the breccia from Subunit IVB (Sections 149-899B-28R-1 to 37R-1) contain samples having few, poorly to moderately preserved, calcareous nannofossils, but also contain rare samples having abundant and well-preserved nannofossils. We applied the zonation of Martini (1971) and Sissingh (1977); in most cases, using the primary zonal markers. However, secondary markers, whose biostratigraphic ranges have been recently indicated by Rio et al. (1990) or have been summarized by Perch-Nielsen (1985), were used in a number of instances where abundant reworked specimens occurred or where the primary zonal markers were not present. The biostratigraphy for Site 899 has been summarized in Figure 27.

Hole 899A

Pliocene

Intervals 149-899A-1R-2, 44 cm, to -4R-2, 115 cm, contain rare specimens of *Discoaster pentaradiatus, Discoaster surculus,* and *Discoaster brouweri,* which suggests a late Pliocene age within Zone NN16. Sample 149-899A-3R-CC has very rare *Sphenolithus neoabies.* Samples 149-899A-4R-CC, 44 cm, to -5R-3, 49 cm, yielded very abundant *Discoaster pentaradiatus* and *Reticulofenestra ampla,* which indicates the lower part of Zone NN16. Samples 149-899A-5R-CC and -6R-1, 86 cm, were placed in Zone NN15 on the basis of few *Reticulofenestra pseudoumbilica,* common *Discoaster tamalis,* and common *Discoaster asymmetricus.*

Miocene

In Sample 149-899A-6R-CC, the occurrence of *Triquetrorhabdulus rugosus* and *Amaurolithus delicatus* and the absence of *Discoaster quinqueramus* indicate the uppermost Miocene (Zone NN12). The Pliocene/Miocene boundary was correlated with the highest occurrence (HO) of *Triquetrorhabdulus rugosus,* which occurs in the lower part of Zone NN12. However, according to the foraminiferal data (see below), the age of Sample 149-899A-6R-CC may be slightly younger and has been assigned to the upper part of Zone NN12, which represents the lowermost Pliocene. An early Pliocene hiatus within Core 149-899A-6R has been estimated to represent at least 1.50 Ma from the HO of *Triquetrorhabdulus rugosus* to the lowest occurrence (LO) of *Discoaster tamalis.* Intervals 149-899A-7R-1, 52 cm, to -8R-CC contain few *Amaurolithus delicatus* and *Discoaster quinqueramus,* which indicates Subzone NN11b. *Amaurolithus primus* markers were observed in Sample 149-899A-7R-1, 52 cm, at the top of Zone NN11b. Sample 149-899A-9R-3, 71 cm, contains common *Sphenolithus abies* and rare *Sphenolithus verensis,* but lacks *Discoaster loeblichii* and can be assigned to Subzone NN11a. Rare *Discoaster loeblichii* occur in Sample 149-899A-9R-CC and indicate the upper part of Zone NN10. Samples 149-899A-10R-l, 58cm, and -10R-CC contain few *Discoaster prepentaradiatus* and rare *Discoaster neohamatus,* but lack *Discoaster hamatus.* This interval was assigned to the lower part of Zone NN10. Samples 149-899A-11R-1, 118cm, and -11R-CC contain very rare *Discoaster deflandrei,* rare *Cyclicargolithus floridanus, Discoaster exilis, D. kugleri,* and *D. moorei,* and few *Triquetrorhabdulus rugosus.* This assemblage indicates the lower part of Zone NN7 and also that a major unconformity lies between the middle Miocene Zone NN7 and the upper Miocene Zone NN10. On the basis of the presence of *Cyclicargolithus floridanus* in Sample 149-899A-11R-1, 118 cm, and the absence of *Discoaster hamatus* in Sample 149-899A-10R-CC, the unconformity may represent an age of at least 2.9 Ma. The LO of *Calcidiscus macintyrei* (≥10.0 µm, circular) was in Sample 149-899A-11R-1, 118 cm. Intervals 149-899A-13R-CC, 7 cm, to -13R-CC were assigned to Zone NN6, as indicated by the presence of rare *Triquetrorhabdulus rugosus* and *Calcidiscus premacintyrei* and common *Cyclicargolithus flori-*

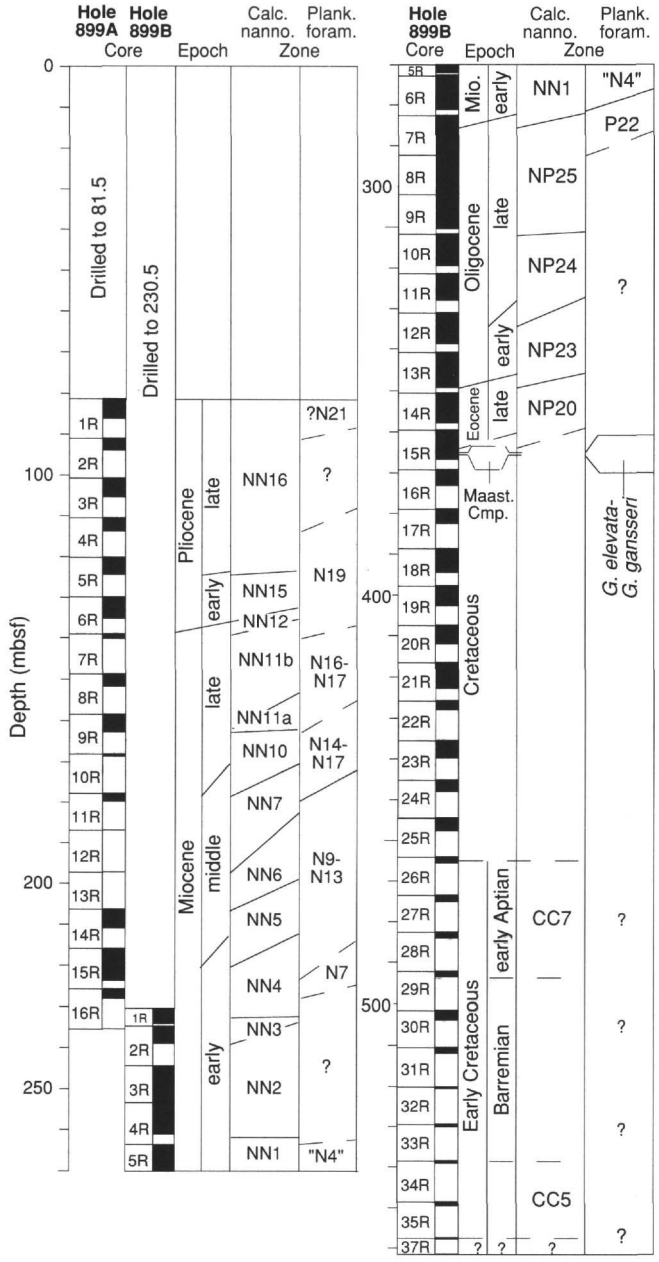

Figure 27. Summary of planktonic microfossil zones from Site 899. Epoch/Stage: Maast.-Cmp. = Maastrichtian to Campanian. Planktonic foraminifers zone: *G. elevata—G. gansseri* = *Globotruncanita elevata* to *Gansserina gansseri* zones. Calcareous nannofossil zonations are from Martini (1971) for the Cenozoic and from Sissingh (1977) for the Mesozoic.

danus. *Sphenolithus heteromorphus* occurs in Sample 149-899A-14R-CC, which places this sample in Zone NN5. Intervals 149-899A-15R-3, 125 cm, to -16R-CC were placed in the lower Miocene Zone NN4 on the basis of the presence of few *Sphenolithus heteromorphus* (Sample 149-899A-15R-3, 140 cm), rare *Sphenolithus dissimilis* and *Helicosphaera ampliaperta,* rare to few *Calcidiscus leptoporus,* sporadic occurrence of *Calcidiscus premacintyrei,* and abundant *Discoaster deflandrei.* Rare Cretaceous, rare lower Miocene, and very abundant Eocene reworked specimens occur repeatedly throughout this interval. The resedimented sequences deposited during the early Miocene may correspond to an increase during this time of contour current sedimentation (lithostratigraphic Subunit IIB; see "Lithostratigraphy and Petrology" section, this chapter).

Hole 899B

Miocene

Sample 149-899B-1R-3, 1 cm, contains rare *Calcidiscus premacintyrei, Discoaster moorei,* and *Discoaster variabilis,* and few *Calcidiscus leptoporus.* This assemblage has been assigned to the lower Miocene Zone NN4 and has an assemblage of calcareous nannofossils similar to that in Core 149-899A-16R. Sample 149-899B-1R-3, 36 cm, contains *Sphenolithus belemnos* and Sample 149-899B-2R-2, 36 cm, contains *Sphenolithus dissimilis, Discoaster druggii,* and *Calcidiscus leptoporus,* but lacks *Triquetrorhabdulus carinatus.* This interval can be assigned to the lower Miocene Zone NN3. Intervals 149-899B-2R-CC to -4R-6, 18 cm, can be assigned to the lower Miocene Zone NN2 by the presence of *Triquetrorhabdulus carinatus.* The underlying sequence, from Samples 149-899B-4R-CC to -6R-CC, yielded various assemblages corresponding to Zone NN1. *Helicosphaera recta* occurs in Sample 149-899B-4R-CC, and *Sphenolithus ciperoensis* has its HO in Sample 149-899B-5R-6, 16 cm. Rare *Cyclicargolithus abisectus,* few *Clausicoccus fenestratus* and *Zygrhablithus bijugatus,* and common *Reticulofenestra bisecta* also indicate Zone NN1 but, due to reworked material, no biostratigraphic events have been defined.

Oligocene

Oligocene assemblages were observed from Samples 149-899B-7R-2, 79 cm, to -13R-4, 62 cm, and represent continuous deposition from Zones NP23 to NP25. The assemblages observed are similar to those observed at Sites 897 and 898. Samples 149-899B-7R-2,79 cm, to -9R-CC contain rare *Pontosphaera enormis,* few *Helicosphaera recta,* common *Sphenolithus ciperoensis, Cyclicargolithus abisectus,* and *Reticulofenestra bisecta,* indicating the upper Oligocene Zone NP25. The HO of *Sphenolithus distentus, Sphenolithus predistentus,* and *Helicosphaera compacta* is in Sample 149-899B-10R-1, 83 cm, and this defines the top of Zone NP24. The interval from here to Sample 149-899B-11R-4, 134 cm, is also from Zone NP24. Intervals 149-899B-12R-2, 141 cm, and -13R-4, 63 cm, were assigned to Zone NP23 on the basis of the presence of *Sphenolithus predistentus* and the absence of *Sphenolithus ciperoensis.* The LO of *Sphenolithus distentus* and *Coronocyclus nitescens* is recorded in Sample 149-899B-13R-2, 127 cm. Zones NP22 and NP21 were not observed between Samples 149-899B-13R-2, 127 cm (Zone NP23), and -13R-CC (NP20). According to the sediment accumulation rate during this period (about 9 m/m.y.) and according to the biostratigraphic time scale (see Table 1 in "Explanatory Notes" chapter, this volume), an unconformity lies between the HO of *Sphenolithus distentus* (33.1 Ma) and the LO of *Discoaster saipanensis* (35.6 Ma) and represents 2.5 Ma of missing sediment. The Eocene/Oligocene boundary (35.4 Ma) must be located just above Sample 149-899B-13R-CC.

Eocene

Intervals 149-899B-13R-CC to -15R-1, 4 cm, were assigned to Zone NP19/20. Sample 149-899B-13R-CC contains rare *Discoaster saipanensis, Discoaster barbadiensis,* and *Cyclococcolithus formosus,* and few *Reticulofenestra hillae* and *Reticulofenestra umbilica.* Sample 149-899B-15R-1, 4 cm, contains *Isthmolithus recurvus* and can be assigned an age not older than zone NP19/20. Below this level, no more fossiliferous calcareous claystones were observed in the Cenozoic sequence.

Cretaceous

Drilling in Hole 899B recovered a sequence from Upper Cretaceous to Lower Cretaceous from Sample 149-899B-15R-3, 147-149 cm, to Core 149-899B-37R. From Section 149-899B-15R-1 (upper Eocene) to Sample 149-899B-16R-4, 21 cm no calcareous nannofos-

sils were observed, but a Cretaceous age was indicated by the planktonic foraminifers for Sample 149-899B-15R-3, 147 cm, which was barren of calcareous nannofossils. From Sample 149-899B-16R-4, 21 cm, to -26R-1, 85 cm, only serpentinized peridotite was recovered.

The first datable lithology in Subunit IVA occurs in Sample 149-899B-26R-1, 85 cm. This sample and Sample 149-899B-29R-1, 22 cm, were assigned to the Aptian Zone CC7 on the basis of *Rucinolithus irregularis, Micrantholithus hoschulzii,* and *Micrantholithus obtusus*. Sample 149-899B-27R-1, 65 cm, and Section 149-899B-28R-1 contain moderately well-preserved calcareous nannofossils, which may yield good ages after more detailed analyses.

The lowermost sample of Hole 899B (149-899B-35R-1, 99 cm) in Subunit IVB having calcareous claystone yielded a common and well-preserved assemblage. This sample was assigned to the lower Barremian, as indicated by rare *Rucinolithus terebrodentarius, Markalius ellipticus, Calcicalathina oblongata, Tranolithus pseudoangustus, Calcicalathina* aff. *C. oblongata, Micrantholithus hoschulzii, Micrantholithus obtusus,* few *Microstaurus chiastus, Reinhardtites praesisyphus, Nannoconus globulus, Nannoconus ligius, Nannoconus steinmanii,* and common *Nannoconus* spp. and by the absence of *Rucinolithus irregularis*. Also present in this sample were rare *Cruciellipsis cuvillieri, Seetonia colligata,* and *Zeugrhabdotus erectus,* which may indicate a late Hauterivian age, but the presence of a specimen of *Conusphaera mexicana minor,* indicated the presence of reworked sediments. According to Bralower et al. (1989), *Conusphaera mexicana minor* has a stratigraphic range restricted to the Tithonian. This interpretation is also supported by the composition of this sample, a claystone with reworked basalt clasts (see Table 12 and the "Lithostratigraphy and Petrology" section, this chapter), and by the highly deformed nature of this interval. Other samples from Subunit IVB (149-899B-32R-1, 5 cm; -33R-1, 13 cm) contain few and poorly preserved calcareous nannofossils that exhibit severe dissolution.

Foraminifers

Planktonic foraminifers in core-catcher samples from Holes 899A and 899B were examined to establish preliminary ages for the sediments. The number of planktonic foraminifers was generally low, with more planktonic foraminifers present in Hole 899A than in Hole 899B. Many of the samples were barren or yielded a low-diversity planktonic foraminiferal assemblage having moderate preservation (Table 13). Similar patterns were observed in the benthic foraminiferal assemblages.

Hole 899A

Sample 149-899A-1R-CC is characterized by the presence of relatively common *Globorotalia inflata* and the absence of *Globorotalia truncatulinoides* and *Globorotalia tosaensis*. This sample has been tentatively assigned to Zone N21, which is of late Pliocene age. Samples 149-899A-2R-CC and -3R-CC contain no zonal markers. Samples 149-899A-4R-CC and -5R-CC are characterized by the presence of *Globorotalia puncticulata* and the absence of *Globorotalia inflata* and *Globorotalia margaritae margaritae,* indicating that they can be assigned to the upper part of Zone N19, which is of late early to early late Pliocene age. Sample 149-899A-6R-CC contains *Globorotalia merotumida* and *Globorotalia crassaformis crassaformis* and can be assigned to the early part of Zone N19, which is of early Pliocene age. This sample also contains *Globorotalia margaritae margaritae, Globigerina nepenthes,* and *Sphaeroidinellopsis seminulina*. Abyssal and reworked shallow-water benthic foraminifers were present in all these samples.

Samples 149-899A-7R-CC and -8R-CC are characterized by the presence of *Neogloboquadrina pachyderma* and *Globigerina nepenthes* and the absence of *Globorotalia crassaformis* s.l., indicating that these two samples can be assigned to Zones N16/N17, which are of late Miocene age. Although Zone N18 was not identified, calcareous nannofossil evidence does not support an unconformity between Samples 149-899A-6R-CC and -7R-CC. Sample 149-899A-9R-CC contains only *Globigerina nepenthes,* which has a long range from Zone N14 to the early part of Zone N19. As Zone N17 had already been reached in Sample 149-899A-7R-CC, this sample was interpreted to be somewhere in Zones N14 to N17, which are of late middle to late Miocene age. Sample 149-899A-10R-CC contains *Globorotalia nepenthes, Globorotalia conoidea, Globoquadrina dehiscens,* and *Sphaeroidinellopsis disjuncta* and can also be placed in Zones N14 to N17. Few abyssal benthic foraminifers were present in these samples.

Samples 149-899A-11R-CC and -13R-CC have an assemblage similar to that in Sample 149-899A-10R-CC. These samples also contain *Globorotalia mayeri,* but *Globigerina nepenthes* is absent. This interval can be assigned to Zones N9 to N13, which are of middle Miocene age. Sample 149-899A-14R-CC is characterized by the presence of *Globorotalia scitula scitula* and the absence of *Globigerina nepenthes* and also can be placed in Zones N9 to N13. The presence of only thick-shelled planktonic foraminifers from Samples 149-899A-7R-CC to -13R-CC points to a high degree of dissolution in this interval. Radiolarians and silicoflagellates also were common in Intervals 149-899A-11R-CC to -14R-CC.

Sample 149-899A-15R-CC is characterized by the presence of *Catapsydrax stainforthi* and absence of *Catapsydrax dissimilis*. It can be assigned to the N7 zone, which is of late early Miocene age. Also present in this sample are *Globorotalia altispira altispira, G. altispira globosa, Globorotalia mayeri* and *Globorotalia siakensis*. Although Zone N8 was not identified in the core-catcher samples, calcareous nannofossil evidence does not support an unconformity between Samples 149-899A-14R-CC and -15R-CC. Sample 149-899A-16R-CC is barren of planktonic foraminifers.

Hole 899B

Samples 149-899B-1R-CC and -4R-CC are barren of planktonic foraminifers. Samples 149-899B-2R-CC and -3R-CC contain very rare planktonic foraminifers, none of which can be used as a zonal marker. Sample 149-899B-5R-CC is marked by the presence of *Globorotalia kugleri* and *Globigerinoides* spp. *Globorotalia kugleri* defines the "N4" zone, which is of latest Oligocene to early Miocene age. Sample 149-899B-6R-CC does not contain *G. kugleri,* but *Globigerinoides* spp. are still present. This sample belongs to the upper part of Zone P22, which is of late Oligocene age. Radiolarians and silicoflagellates also are common in these samples.

Samples 149-899B-7R-CC, -8R-CC, -10R-CC, -11R-CC, -12R-CC, -13R-CC, -14R-CC, and 15R-CC are barren of planktonic foraminifers. Sample 149-899B-9R-CC contains very rare planktonic foraminifers, none of which is a zonal marker. Samples 149-899B-13R-CC and -14R-CC contain only arenaceous benthic foraminifers *(Bathysiphon* spp., *Glomospira charoides, Glomospira* spp., *Cyclammina* spp., *Haplophragmoides* spp., and *Recurvoides* spp.) and ichthyoliths.

Sample 149-899A-15R-3, 147-149 cm, contains *Globotruncana orientalis* and *Globotruncana lineana,* indicating that it belongs between the *Globotruncanita elevata* Zone and the lower part of the *Gansserina gansseri* Zone, which are of Campanian to early Maastrichtian age (Robaszynski et al., 1984). Other species found in this sample are *Archeoglobigerina cretacea, Hedbergella holmdenensis,* and *Marginotruncana marginata.*

PALEOMAGNETISM

At Holes 899A and 899B, magnetic measurements using the pass-through cryogenic magnetometer were performed on all archive halves of cores, and the magnetic susceptibility of all cores was measured at 3-cm intervals. Sections of sediment were progressively demagnetized at 10-cm intervals using peak fields of 10 or 15 mT, as

Table 13. Distribution of planktonic and some benthic foraminifers in Holes 899A and 899B.

Age	Zone	Hole	Core	Abundance	Preservation	*Globigerinoides conglobatus*	*G. extremus*	*G. ruber alba*	*Globorotalia crassaformis crassaformis*	*Globorotalia inflata*	*G. scitula scitula*	*Neogloboquadrina acostaensis*	*N. pachyderma*	*Orbulina universa*	*Globorotalia crassula*	*Orbulina suturalis*	*Globorotalia punticulata*	*Globigerina nepenthes*	*Globigerinita naparimaensis*	*Globigerinoides obliquus*	*Globigerinoides sacculifer*	*Globigerinoides trilobus*	*Globorotalia margaritae margaritae*	*G. merotumida*	*Globorotalia ronda*	*Sphaeroidinellopsis seminulina*	*Orbulina bilobata*	*Globoquadrina venezuelana*	*Globoquadrina dehiscens*	*Sphaeroidinellopsis disjuncta*	*Globorotalia conoidea*	*Globorotalia mayeri*	*Globorotalia menardii* s.l.	*Cassigerinella chipolleensis*	*Globigerina woodi*	*Neogloboquadrina continuosa*	*Globoquadrina baroemoenensis*	*Globoquadrina altispira altispira*	*G. altispira globosa*	*Globorotalia obesa*	*Globorotalia siakensis*	*Catapsydrax stainforthi*	*Globigerinoides subquadratus*	*Catapsydrax dissimilis*	*C. unicavus*	*Globoquadrina praedehiscens*	*Globigerinoides* spp	*Globorotalia kugleri*	*Globorotalia nana/continuosa* transition	*Globotruncana lineana*	*G. orientalis*	*Archeoglobigerina cretacea*	*Hedbergella holmdensis*	*Marginotruncana marginata*
Pliocene	?N21	899A	1R	A	G	R	F	F	R	C	R	R	F	C																																					
	?		2R	R	M							R	R																																					
			3R	C	M							F	C	R																																				
	N19		4R	A	M				C		R	R	F	F	R	R																																	
			5R	A	M				F			R	F	F	R		R																																
			6R	A	M		R		F		R	R	F	R				R	R	R	R	R	R	R	R	R																							
l. Mio.	N16–N17		7R	C	M								F	R				R								R	R																						
			8R	C	M								R					R								R																						
m.–l. Mio.	N14–N17		9R	F	M													F																															
			10R	C	M													F									R	R	R	R																		
m. Mio.	N9–N13		11R	F	M																						F	R	R	R	R																	
			12R	X																																												
			13R	C	P											R										R	R		R		F	R	R														
			14R	C	M						R							R	R													R		R	R	R										
e. Mio	N7		15R	A	M																F	F					R	F						R	F	R	R	R	F	C	R	R					
?			16R	B																																												
	?	899B	1R	B																																												
			2R	R	M																											R								R								
			3R	R	M																											R																
			4R	B																																												
e. Mio.	"N4"		5R	F	M																						R					R			R				F		R	R	R	R	R				
l. Oli.	P22		6R	A	M																						R					F										R		R		F				
?			7R	B																																													
			8R	B																																													
			*9R	R	P																																												
	?		10R	B																																													
			11R	B																																													
			12R	B																																													
			13R	B																																													
			14R	B																																													
Cp.–Ma.	*Gl.–Ga.*		15R-3	F	M																																										R	R	R	R	R
?	?		15R-CC	B																																													

Notes: Age: Cp.-Ma. = Campanian to early Maastrichtian; l. Oli. = late Oligocene; e. Mio. = early Miocene; m. Mio. = middle Miocene; m.-l. Mio. = middle to late Miocene; l. Mio. = late Miocene. Zone: *Gl.-Ga.* = between *Globotruncanita elevata* and *Gansserina gansseri* zones. A "* " in the "Core" column indicates that the core-catcher sample contained only juvenile planktonic foraminifers or no marker species. Abundance: A = abundant; C = common; F = few; B = barren; X = no core recovery. Preservation: G = good; M = moderate; P = poor.

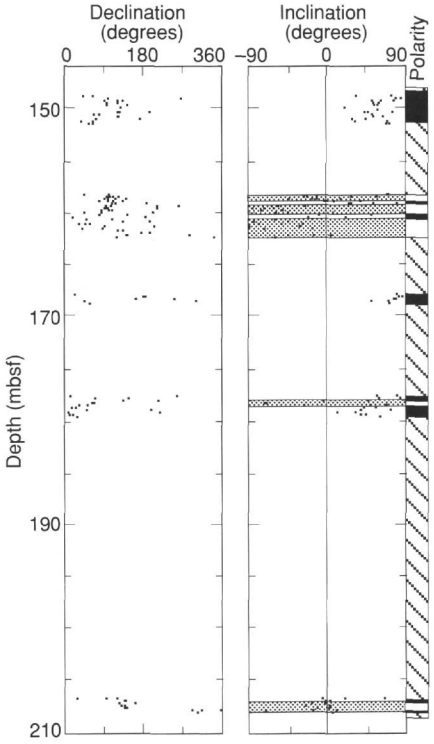

Figure 28. Magnetic declination and inclination for Cores 149-899A-8R to -14R (after AF demagnetization at 15 mT). Zones in black (white) correspond to normal (reversed) polarity. Cross-hatched zones represent no recovery. Gray areas outline reversed polarity intervals.

well as sections of the serpentinite breccias at 2- to 5-cm intervals with a peak field of 15 mT. Thirty-six discrete samples taken from the working halves of cores from the two holes were progressively alternating-field (AF) and thermally demagnetized to verify the magnetostratigraphic results from the cryogenic magnetometer.

Magnetostratigraphy of the Sedimentary Section

Hole 899A

As drilling at Hole 899A started with drill pipe that had not been used for a relatively long time, many of the cores from Hole 899A exhibit strong signs of drilling-induced remagnetization, as evidenced by the ubiquitous normal polarity and almost vertical inclinations in the NRM measurements. Fortunately, AF demagnetization to 15 mT can generally remove this strongly induced, but relatively "soft," overprint and isolate the stable component of magnetization. At Hole 899 A, core recovery averaged only 33%, and the first four cores were highly disturbed by drilling. Pass-through cryogenic magnetometer measurements identified five magnetic reversals from 160.0 to 210.0 mbsf (Fig. 28). According to the shipboard biostratigraphic age determinations (see "Biostratigraphy" section, this chapter), sediments at about 162.0 mbsf may be 8.3 Ma old (late Miocene). This suggests that the shift from normal to reversed polarity at 160.5 mbsf may fall within the C4A Chron (8.91-8.02 Ma). An exact polarity chron assignment, however, is impossible at this time because of the absence of adequate age control. Below 210 mbsf, sediments are too weakly magnetized to be measured reliably.

Hole 899B

The magnetic intensity of sediments from Hole 899B was consistently very weak, essentially the same magnitude as the noise level of the cryogenic magnetometer and the sample holder. A weak, and magnetically "soft", reversed remanent magnetization was observed in Core 149-899B-6R (273.4-281.5 mbsf), but will have to await shore-based work for confirmation. Between 282 and 320 mbsf, the NRM intensities decrease to only 0.1 mA/m, and the measurements of magnetic directions become noisy and inconsistent. Discrete sample demagnetizations show no stable remanence. Therefore, it was not possible to determine the polarity of sediments recovered from this interval on board the ship. From 323 to 360 mbsf, the NRM intensities increase by an order of magnitude. The inclinations after AF demagnetization suggest a period of predominantly normal polarity. Currently, the poor recovery in Hole 898A and weakly magnetized sediments in Hole 899B do not permit us to construct a magnetostratigraphy.

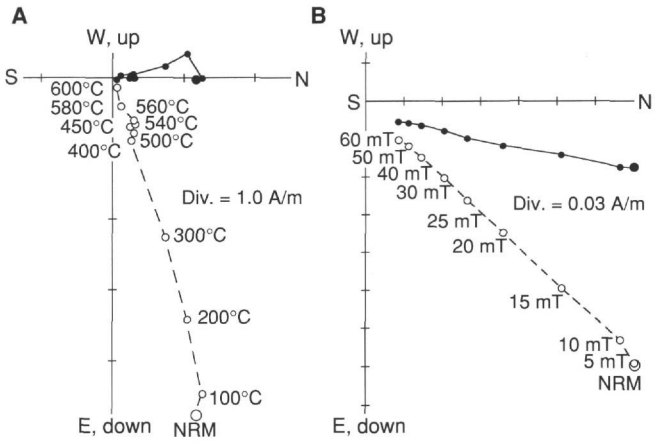

Figure 29. Representative vector end-point diagram showing the results of AF and thermal demagnetizations for discrete Samples 149-899B-19R-3, 66-68 cm **(A)** and -21R-4, 77-79 cm **(B)**. Open and solid circles represent vector end points projected onto the vertical and horizontal planes, respectively.

Paleomagnetic Observations from Lithologic Unit IV

From 369.9 to 482.9 mbsf in Unit IV (see "Lithostratigraphy and Petrology" section, this chapter), magnetic remanence in both pass-through and discrete sample measurements is apparently very stable. Eight samples were AF-demagnetized using peak fields ranging from 40 to 90 mT, depending on the coercivity of the sample. In addition, 14 samples were thermally demagnetized up to 600°C. A stable component of magnetization usually can be identified by both techniques (Fig. 29). We were surprised that, with the exception of small pieces of core, this interval shows a stable normal field direction. Although a normal polarity remagnetization might conceivably explain this feature, we deem this unlikely based on the magnetic behavior of cores from below this interval and on the preliminary shipboard biostratigraphic ages. Biostratigraphic ages suggest that cores below 364.6 mbsf are of pre-Latest Cretaceous age, and preliminary paleomagnetic results from Core 149-899B-28R (484.2 mbsf) show negative inclinations (reversed polarity?). Hence, the rocks from 369.8 to 482.9 mbsf may have acquired remanent magnetization during the Cretaceous Long Normal Superchron (83-124 Ma). However, the relatively highly oxidized material in this interval indicates the magnetization in these rocks may be complex and renders any polarity evaluation suspect. The age and origin of the magnetic signal in this interval are not well understood at this time.

Below 482.9 mbsf, paleomagnetic results that are useful for magnetostratigraphic studies were obtained only from some of the discrete samples taken from long continuous pieces of cores. As shown in Figure 30, thermal demagnetization of Samples 149-899B-28R-1, 86-88 cm, and -30R-2, 8-10 cm, removed a "soft" component, probably of viscous origin, at low to intermediate temperatures (200°-400°C). After further demagnetization up to 585°-600°C, the stable

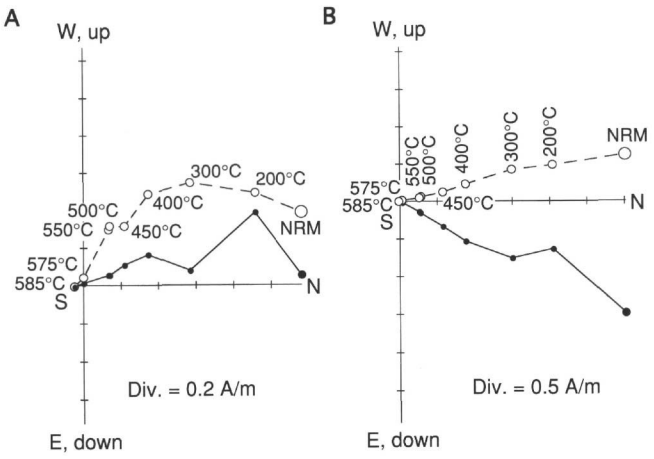

Figure 30. Representative vector end-point diagram showing the results of thermal demagnetization of discrete Samples 149-899B-28R-1, 86-88 cm (**A**), and -30R-2, 8-10 cm (**B**). Open and solid circles represent vector end points projected onto the vertical and horizontal planes, respectively.

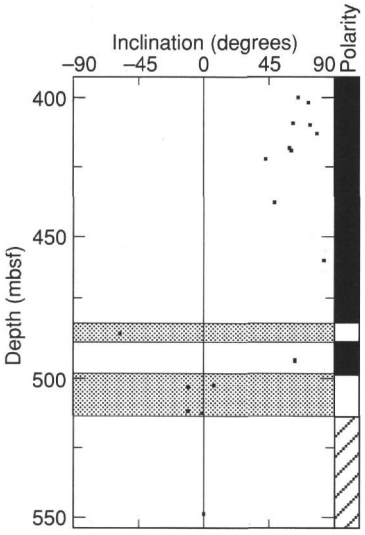

Figure 31. Plot of magnetic inclinations of thermally demagnetized discrete samples as a function of sub-bottom depth from 400 to 550 mbsf in Hole 899B. Gray areas outline reversed polarity intervals. The tentative interpretation of the polarity is shown on the right; zones in black (white) correspond to normal (reversed) polarity; cross-hachured zones represent uncertain polarity intervals.

component of magnetization was revealed. The unblocking temperatures and coercivities indicate that the dominant magnetic mineral in these samples is magnetite.

There appear to be two polarity reversals between 484.2 and 549.9 mbsf (Fig. 31), as suggested by the inclination changes in some thermally demagnetized discrete serpentinite samples from the mass flow deposits of Subunit IIIB (see "Lithostratigraphy and Petrology" section, this chapter). We do not yet know when they occurred.

Magnetic Susceptibility

Figure 32 shows the downhole profiles of magnetic susceptibility for Holes 899A and 899B. In Unit I (see "Lithostratigraphy and Petrology" section, this chapter), the magnetic susceptibilities are about 3×10^{-4} SI units, similar to those observed at Sites 898 and 897.

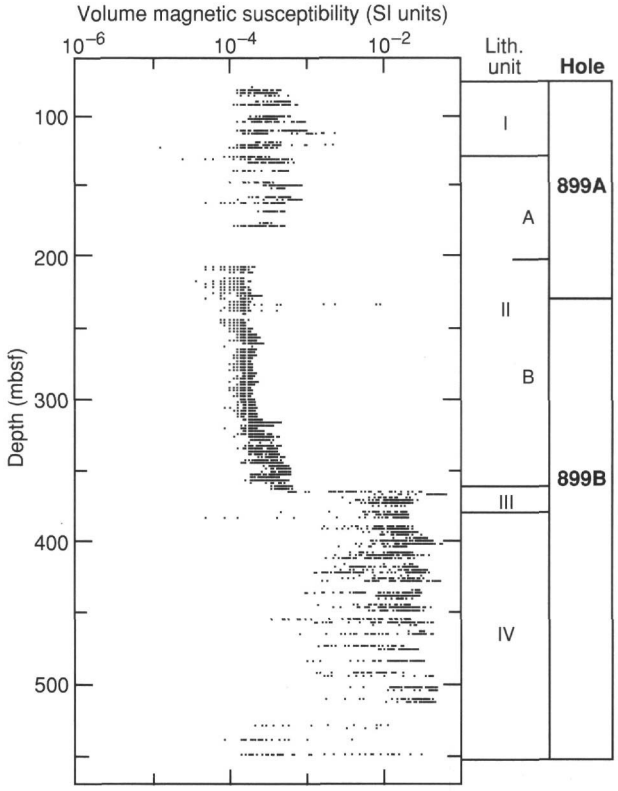

Figure 32. Downhole profile of magnetic susceptibility in Holes 899A and 899B.

Several susceptibility maxima were observed within this unit, most of which correspond to the terrigenous sands at the bases of turbidite sequences. The magnetic susceptibility of the pelagic sediments from 230 to 360 mbsf (Cores 149-899B-1R to -14R, in Unit II) was low, averaging about 1×10^{-4} SI units, which is fully consistent with the observed weak NRM intensities from these cores.

A sharp increase in susceptibility occurs around 364 mbsf (Section 149-899B-15R-3), which corresponds to the boundary between Subunits IIIA and IIIB (see "Lithostratigraphy and Petrology" section, this chapter). A similar pattern was observed at Holes 897C and 897D. Whole-core susceptibility measurements for Hole 899B vary in a similar fashion to the NRM signal. The magnetic susceptibility of Units III and IV averages about 1×10^{-4} SI units, which is about two orders of magnitude higher than those of overlying Unit II (Fig. 32).

STRUCTURAL GEOLOGY

Introduction

Site 899, located over a basement high 18.5 km east-southeast of Site 897, presented a significantly more disturbed sedimentary section than the equivalent units at Site 897. The acoustic basement at Site 899, capped by unusual serpentinite breccia units (see "Lithostratigraphy and Petrology" section, this chapter), also displays an abundance of structural features that provide some insight into the formation, emplacement, and post-emplacement history of this unit.

Sediments

The relative abundance of deformation features within the upper lithostratigraphic Units I, II, and III at Site 899 contrasts with the relative scarcity of structures in the equivalent units at Site 897. Post-depositional features observed at Site 899 include dipping beds, folded and contorted sediments, and microfaults. The distribution of deformation structures with depth is apparently not systematic, but

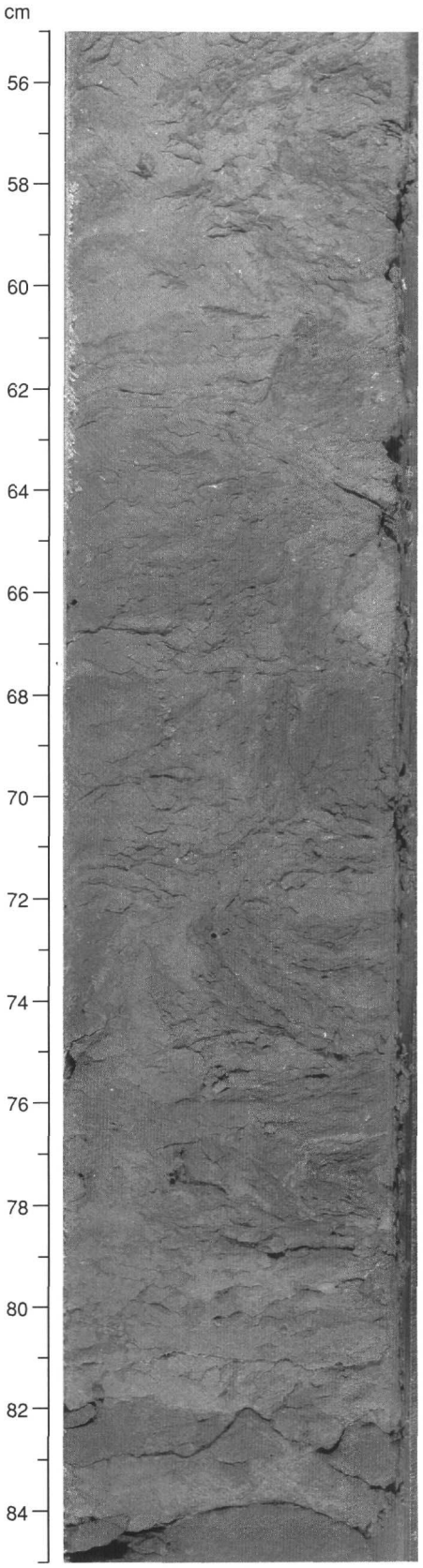

Figure 33. Disrupted sediments at Interval 149-899B-5R-3, 55-85 cm.

observations were limited by core recovery and by the absence of marker horizons that display offset and disturbance.

Cores recovered between the seafloor and 229 mbsf in Hole 899A did not display any clear deformation structures, with the rare exception of bedding dips up to 10° (e.g., Core 149A-899A-14R). The absence of structures may result from their destruction by drilling disturbance, but it also suggests a tectonically quiet post-depositional history during the last 18 m.y.

Structural features were evident within sediments from Hole 899B. In the upper part of the cored interval of Hole 899B (Cores 149-899B-1R to -7R; 230.5-292.7 mbsf), the most common features were zones of highly disturbed sediment, which occurred at a frequency of about one per core. These were characterized by a lack of stratification (in contrast to the adjacent sediments), contortion of color variations, and fissility in the clay-rich sediments (Interval 149-899B-5R-3, 55-85 cm; Fig. 33). Because the consolidation state of these sediments was similar to that of the adjacent undisturbed sediments, we discount drilling disturbance as an explanation. These features could be distinguished from soft-sediment deformation by the high fissility of the core, suggesting that the disturbance post-dated burial. Bedding dips up to 10° also were observed in the upper part of the cored interval of Hole 899B, particularly in the structurally disturbed cores (e.g., Interval 149-899B-7R-7, 6-8 cm).

Microfaults occurred within several cores and were defined most clearly by offsets in color boundaries associated with burrows and depositional cycles (e.g., Interval 149-899B-10R-4, 43-49 cm; Fig. 34). Although several microfaults were observed in the upper cores of Hole 899B, they were best developed below 283 mbsf (Core 149-899B-7R and deeper). The sense of displacement was not always apparent, but both normal and reverse senses of motion were observed, with a maximum measurable displacement of 2 to 2.5 cm.

Acoustic Basement Rocks

The top of Core 149-899B-16R marks the top of a new structural domain composed dominantly of serpentinized peridotite breccias in lithostratigraphic Unit IV. This enigmatic unit displays characteristics of both sedimentary and igneous rocks, and descriptions of lithology and "stratigraphy" are given elsewhere (see "Lithostratigraphy and Petrology" section, this chapter). Several structural aspects of this

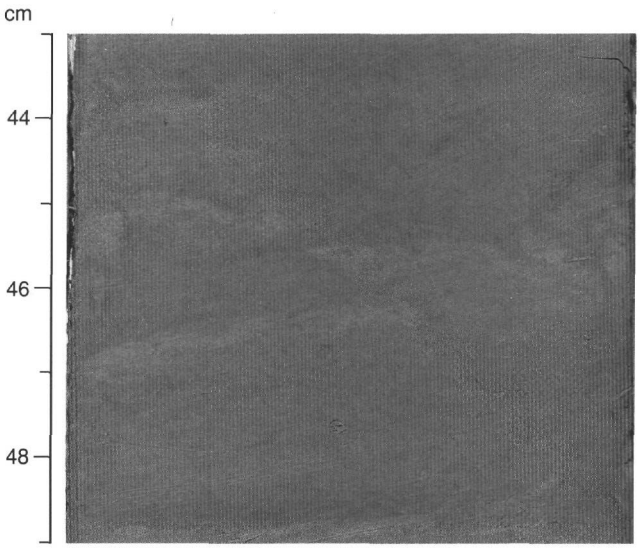

Figure 34. Microfault offsetting a burrow in a reverse sense at Interval 149-899B-10R-4, 43-49 cm.

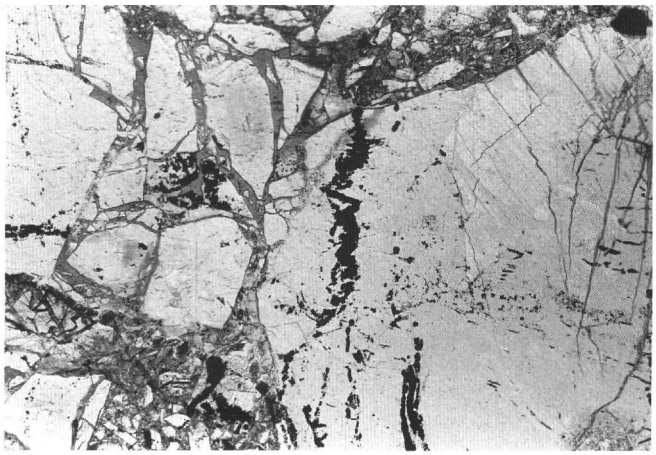

Figure 35. Fractured clasts in Sample 149-899B-21R-1, 12 cm, showing the process of brecciation. Photomicrograph under plane-polarized light; the size of the clasts in the middle part of the photo is on the order of 1 cm across.

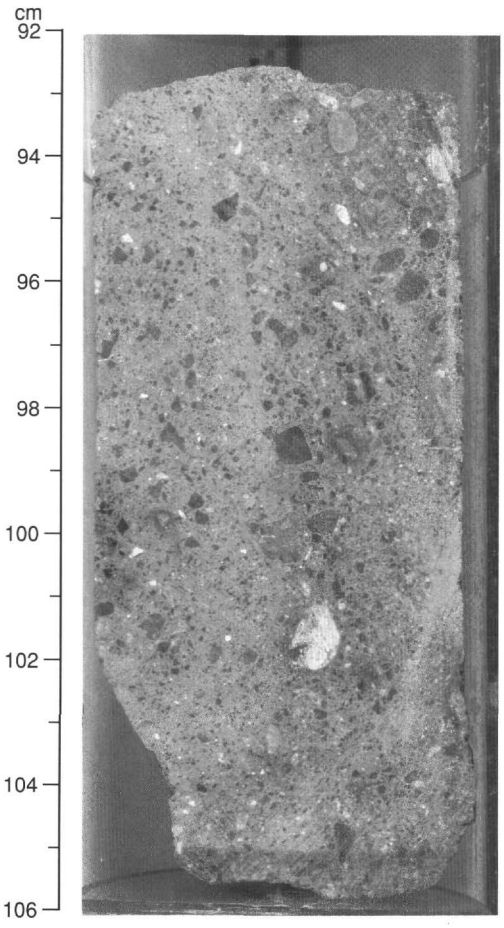

Figure 36. Grain-size zoning in the matrix at Interval 149-899B-23R-2, 92-106 cm.

unit merit discussion, as they may bear on the origin of the breccias, as well as on emplacement and post-emplacement history. These include textural observations of syn-emplacement brittle and ductile deformation of the clasts and matrix, interactions between the breccia units and the underlying sediments and cobbles, and post-emplacement brittle fracture expressed by veining. In addition, evidence exists for pre-emplacement deformation of clasts within and below the breccia units.

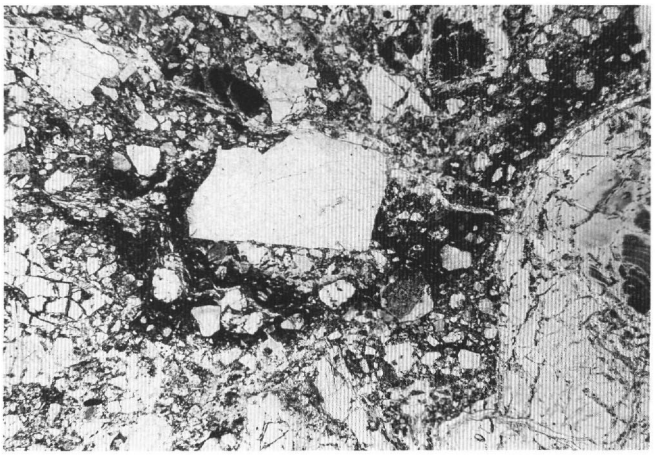

Figure 37. Fragmented grains within an apparently ductile matrix at Interval 149-899B-21R-3, 67-70 cm, defining a "flow fabric" around a clast. A calcite vein can be seen to cross the structure at the upper right. Photomicrograph under plane-polarized light, the size of the largest clast in the middle part of the photo is on the order of 1 cm across.

Structural Fabric of the Breccias

The breccia units consist of angular fragments dominated by serpentinized peridotite, with a continuous size distribution in hand specimen and thin section (see "Lithostratigraphy and Petrology" section, this chapter). Aside from the occurrence of large (>1 m) clasts, the breccia units are homogeneous and nearly structureless. However, subtle fabrics are present within the matrix that help to constrain the mode of origin and emplacement of this unit.

The shape and distribution of the clasts within the breccias record a history dominated by brittle fracture. Clasts are angular, particularly the finer grains, and show pervasive fracturing. Boundaries between clasts and matrix are sharp and often characterized by a reduction in the matrix grain size. Disaggregated grains having fragment trails were observed at both hand-specimen and thin-section scales (Interval 149-899B-26R-1, 50-64 cm; Fig. 18). Some clasts show two symmetric trails that wrap around the clast (Interval 149-899B-24R-3, 88-93 cm). This type of geometry demonstrates a rotational deformation that occurred in a shear regime. The process by which fragmentation took place apparently is frozen in Sample 149-899B-21R-1, 12 cm (Fig. 35), where two grains impinge, fracturing the smaller one. The preservation of fragment trails and the close association of lithologically similar grains suggest that the process of fragmentation was active during the last stages of emplacement.

Matrix textures generally were homogeneous and poorly sorted; however, rare occurrences of grain-size zoning were evident in some intervals (e.g., Interval 149-899B-23R-2, 92-106 cm; Fig. 36).

The texture of the matrix is dominated by brittle features. However, local "flow" fabrics are expressed as narrow shear zones composed of fine, fragmented, and rotated grains (e.g., Sample 149-899B-21R-3, 67 cm; Fig. 37), and occasionally are localized at grain boundaries (e.g., Sample 149-899B-21R-4, 43 cm; Fig. 38). In Interval 149-899B-26R-1, 22-45 cm, a vertical planar fabric has been bent into broad open folds (Fig. 39). These structural features suggest that the matrix flowed, an apparent inconsistency within the well mixed, dominantly brittle fabric that dominates the fabric in the breccia units. Examination of thin sections suggests that the grain fragments may lie within a "ductile" clay-rich matrix, possibly derived from the breakdown of serpentine. The flow fabrics are not uniformly distributed, but appear to occur preferentially near the bases of the inter-

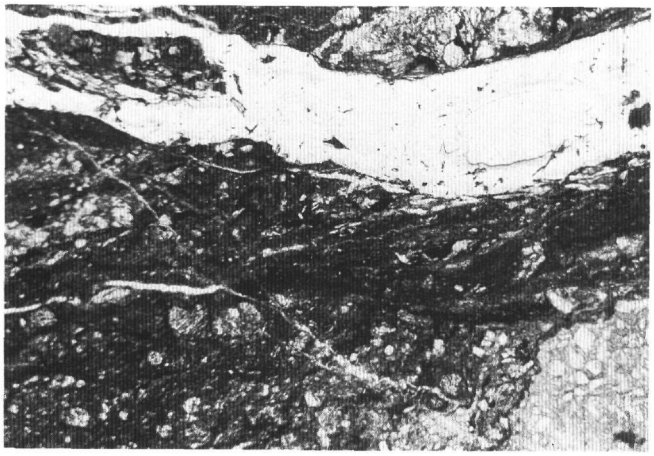

Figure 38. Localized shear zone displaying grain-size reduction, C-S fabric and rotated clasts at the boundary of a fragmented clast (Sample 149-899B-21R-4, 43 cm). Photomicrograph under cross-polarized light, the width of the vein in the upper part of the photo is on the order of 1 cm across.

preted breccia units, apparently near breccia/sediment contacts (see "Lithostratigraphy and Petrology" section, this chapter).

A clear penetrative deformation of the breccia was observed infrequently. A subhorizontal planar fabric near the top of the breccia unit (Sample 149-899B-16R-1, 128 cm) is associated with rotated clasts, alignment of elongate clasts, and a 2-cm-thick shear zone of high intensity deformation (Fig. 40). In Interval 149-899B-28R-1, 110-130 cm two parallel subhorizontal shear zones were observed; a 3-cm-thick shear zone occurs at the boundary of a serpentinized peridotite clast, affecting both matrix and clast, and another 2-cm-thick zone occurs in the clast, deflecting the previous serpentinite foliation (Fig. 41).

Basement Rock/Sediment Contacts

The breccias and other basement rocks recovered from Hole 899B are intercalated with sediments (see "Lithostratigraphy and Petrology" section, this chapter). In rare intervals, the sediment/breccia contact can be directly observed. An excellent example lies in Interval 149-899B-29R-1, 30-70 cm, where blocks of the breccia unit appear to have been fractured and injected by clay-rich mud (Fig. 24). The breccia fragments are intersected by calcite veins, which are apparently continuous with the mud. Our preliminary observations were not adequate for determining (1) if this contact is a normal depositional or weathering boundary or (2) if it represents the disaggregation of the breccia resulting from injection of the mud.

Below the breccia units, intervals consisting of mixed blocks of serpentinized peridotite, microgabbro, basalt, and sediment are thought to represent accumulations of allochthonous blocks. Some evidence exists for deformation within the discontinuous sediment intervals. A silty claystone at Interval 149-899B-30R-1, 5-15 cm, shows millimeter-scale mineralized microfaults, along which burrow marks have been folded and displaced in a normal sense. Meso-scale faults, having offsets of less than 1 cm, were observed within a thin laminated gray sandstone unlike any other lithology at this site (Interval 149-899B-35R-1, 103-122 cm; Fig. 26). This unit resembles siltstones that were recovered at Site 897, where similar microfaults were observed (see "Site 897" chapter, this volume). In Interval 149-899B-27R-1, 41-57 cm, the juxtaposition and textures of altered serpentinized peridotite and claystone suggest shear deformation in both lithologies (Fig. 23). The lithologies and the structural relationships are similar to those described for the Barremian sediments recovered at Site 897 (see "Site 897" chapter, this volume), suggest-

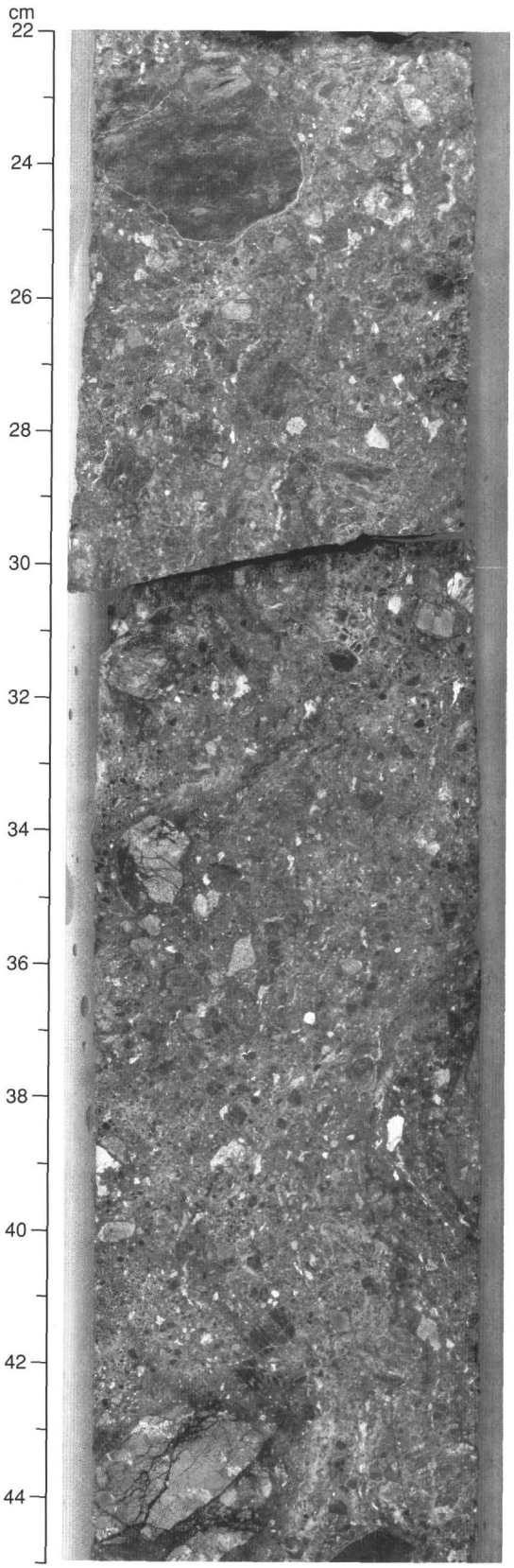

Figure 39. Folded planar fabric observed in the matrix at Interval 149-899B-26R-1, 22-45 cm.

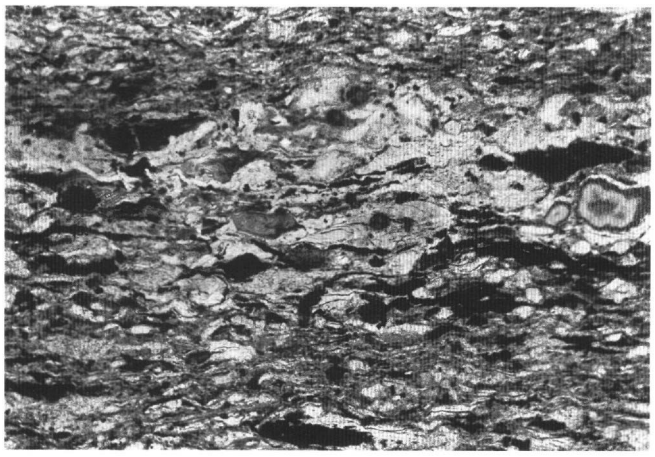

Figure 40. Shear zone in the upper part of the Upper Breccia Unit (Sample 149-899B-16R-1, 121 cm), including elongated and rotated clasts. Photomicrograph under polarized light, the size of the rotated clasts is on the order of 1 mm across.

ing that the two features may have similar histories. These contact zones also involve sand-sized soft serpentine that contains mafic or ultramafic clasts (see "Lithostratigraphy and Petrology" section, this chapter), which have been sheared and folded.

Deformation Within Clasts and Blocks

Except for some relatively fresh pyroxenite and pyroxene-rich peridotite clasts having a primary coarse-grained texture, most of the serpentinized peridotite clasts in Unit IV display evidence for serpentinite recrystallization that pre-dates the formation of the breccias. Except in some of the clasts, this recrystallization has overprinted previous deformation. Figure 42 displays a small clast of serpentinite that is highly sheared (Sample 149-899B-20R-3, 51 cm). The serpentine recrystallization is contemporaneous with intense fracturing that led to the development of veins of dark serpentine and an opaque mineral (magnetite?). This episode of veining was clearly pre-emplacement, as the veins are truncated at the clast boundaries. Rare calcite veins confined to the clasts also were observed, but the relative timing of the calcite and serpentine phases was not immediately evident.

Below the breccia units, near the bottom of Hole 899B (Interval 149-899B-34R-1, 6-37 cm), several pieces of mylonitized microgabbro were recovered. The largest piece displays a vertical foliation associated with a C-S fabric (Fig. 43). A vein parallel to the foliation shows clear evidence of intense shearing. The low recovery of this lithology, and the association with undeformed microgabbro in Interval 149-899B-34R-1, 38-73 cm, suggests that this fabric occurs within an allochthonous block. Cores 149-899B-36W, and -37R also contain some highly sheared chlorite schists of uncertain origin that are associated with microgabbro and basaltic pieces.

Post-Emplacement Deformation

The breccia units and the underlying crystalline rocks are highly veined, which reflects a history of post-emplacement deformation. Two major vein mineralogies were identified: (1) serpentine generally confined within clasts and (2) calcite throughout both matrix and clasts. A third type of vein filled by material having a clastic texture was recognized only near the top of the breccia units and at depth in Core 149-899B-35R.

The serpentine veins were dominantly observed within clasts, particularly of serpentinized peridotite (e.g., Interval 149-899B-22R-

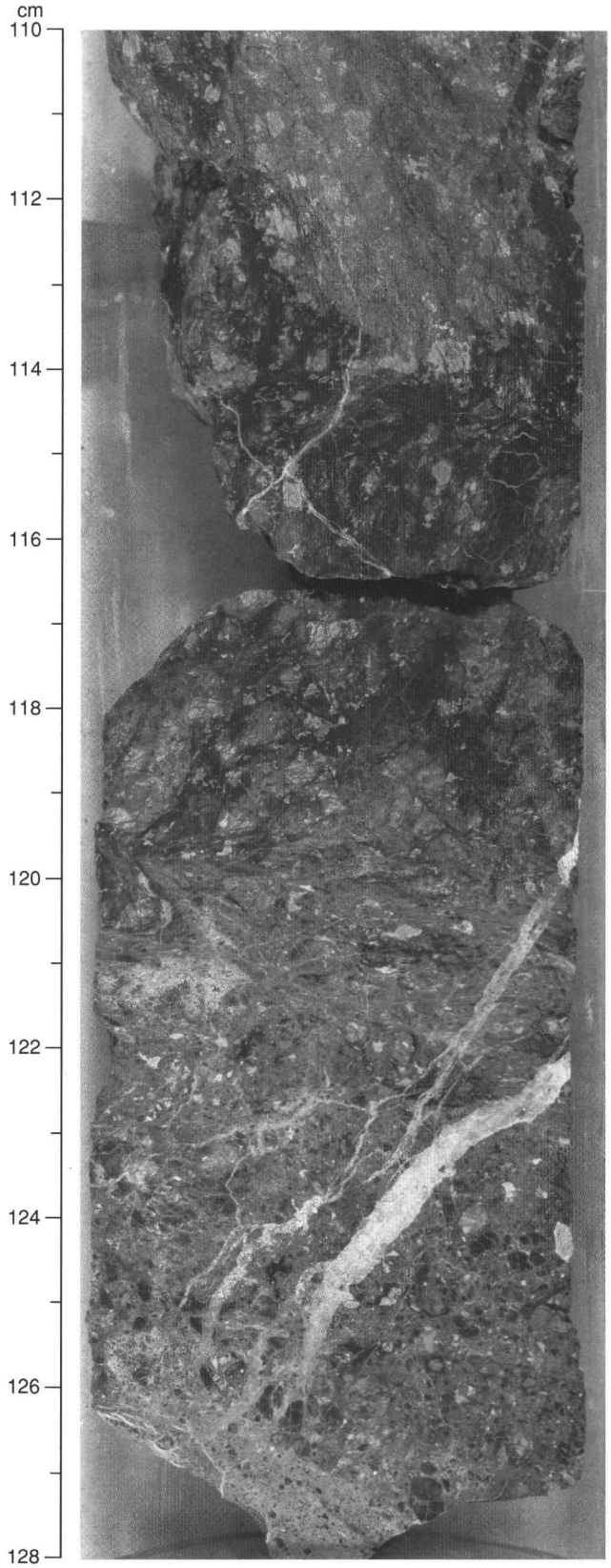

Figure 41. Two parallel shear zones in both matrix and serpentinized peridotite block in Interval 149-899B-28R-1, 110-128 cm.

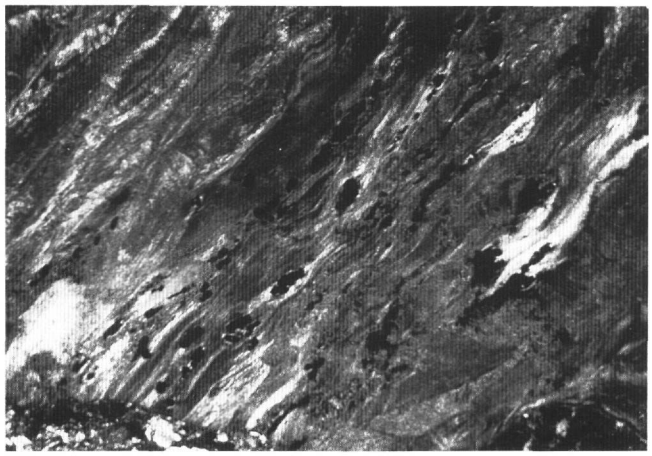

Figure 42. Highly sheared clast of serpentinite in Sample 149-899B-20R-3, 52 cm. This deformation pre-dates the breccia formation. Photomicrograph under polarized light, the size of the opaque minerals is on the order of 1 mm across.

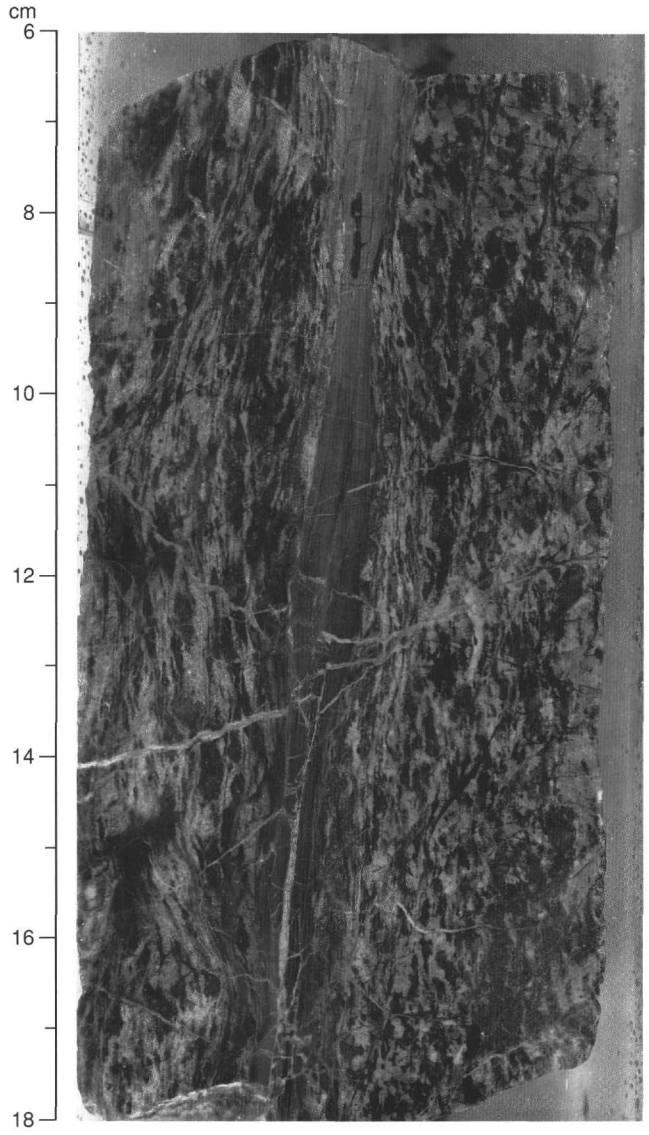

Figure 43. Mylonitized microgabbro in Interval 149-899B-34R-1, 6-18 cm.

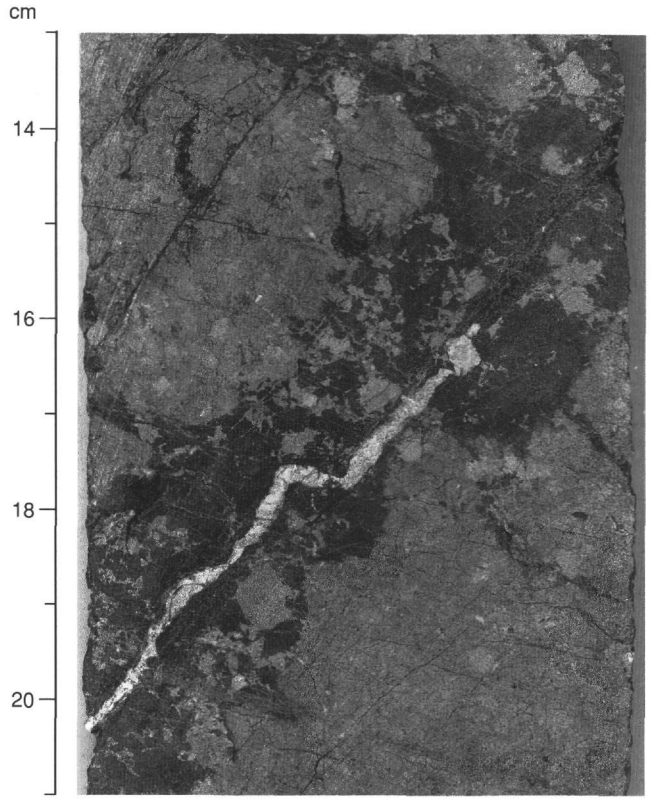

Figure 44. Serpentine and calcite veins within a clast of serpentinized peridotite at Interval 149-899B-20R-2, 13-21 cm.

2, 32-40 cm; Fig. 44). Most of these appeared to be primary features associated with late-stage, low-temperature fracturing of the serpentinized peridotite. However, several medium-to-dark green serpentine veins were observed to traverse the matrix and to transect clast boundaries (Interval 149-899B-20R-2, 40-50 cm). These enigmatic veins are rare and generally have been overprinted by calcite veins, but suggest that an early episode of brittle fracturing of the breccia unit may have occurred.

Calcite veins of various thicknesses are distributed unevenly throughout the breccia units (see discussion in "Lithostratigraphy and Petrology" section, this chapter) and correlate closely with the degree of calcitization of the unit. Large, sheeted, calcite vein complexes tend to be localized along the boundaries of large clasts within the breccias and exhibit multiple stages of crystallization. In some cases (e.g., Interval 149-899B-18R-5, 55-70 cm), calcite appears to have crystallized along preexisting veins composed of white serpentine, occasionally overgrowing (or replacing) the primary mineral (Fig. 45). Elsewhere, calcite is associated with green serpentine veins, some of which propagate through the matrix (Interval 149-899B-18R-2, 0-20 cm). Secondary veins spawned by the larger calcite veins can be observed to crosscut the pre-existing vein filling. This generation of calcite veins was observed to crosscut the fine intraclast serpentine veins and to transect clast boundaries and clearly was formed after lithification of the breccia units. These veins may have accommodated minor displacement, as suggested by offset fractured clasts (e.g., Interval 149-899B-21R-4, 39-2 cm; Fig. 46).

Calcite veins also were observed below the breccia units within crystalline clasts (e.g., Core 149-899B-31R; Interval 149-899B-35R-1, 25-32 cm) and, rarely, in association with sediments. The contact between sheared claystone and sheared, soft serpentine (Interval 149-899B-27R-1, 41-57 cm; Fig. 23) is marked by a thin calcite vein. The boundary between fluidized sediment and breccia at Interval 149-

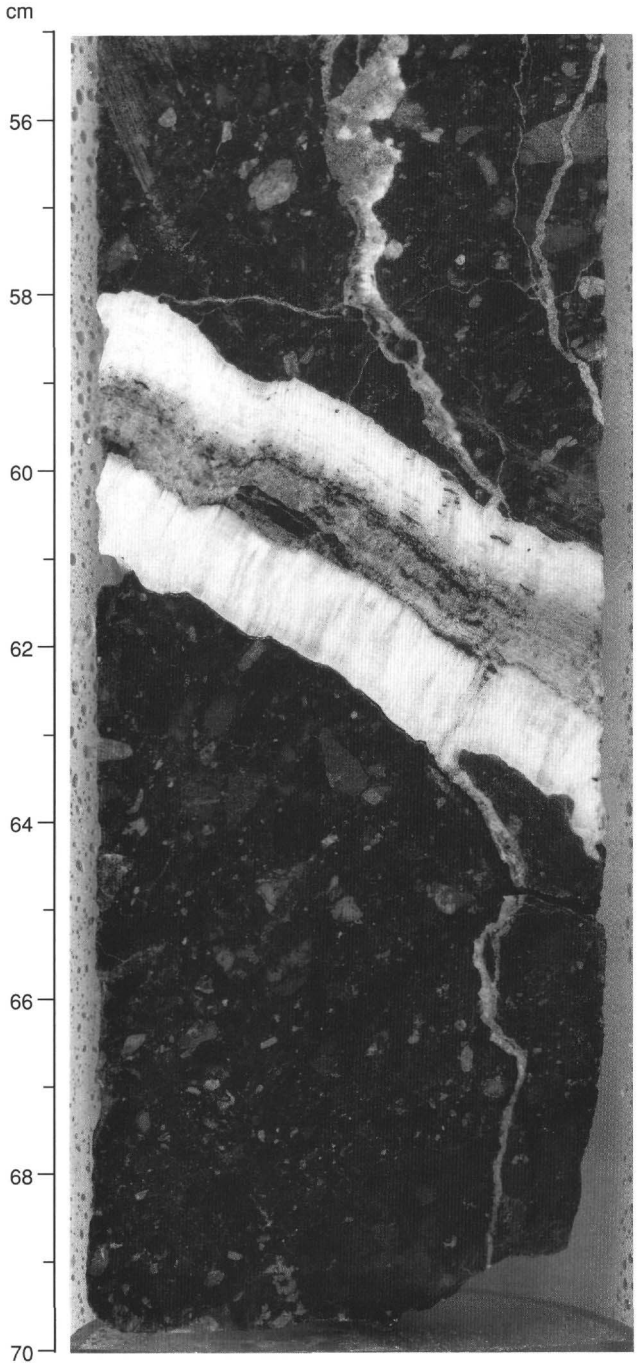

Figure 45. Calcite vein showing multiple stages of crystallization along a preexisting vein of white serpentine at Interval 149-899B-18R-5, 55-70 cm. Late-stage calcite veins spawned by the main vein crosscut earlier generations.

899B-29R-1, 30-70 cm, displays a vein that apparently is continuous with the apparently fluidized sediment, and cuts across the fractured breccia (Fig. 24). The absence of calcite veins elsewhere in the Unit IV sediments is significant, as this may constrain the relative timing of emplacement of the different lithologies observed within Unit IV. The last type of vein is filled with a fine material having granular texture. This type occurs rarely near the top of Unit IV (Sections 149-899B-16R-1 and -2) and at the very bottom of the hole in an apparently allochthonous block of diabase (Interval 149-899B-35R-1, 26-39 cm; Fig. 47). This vein type was observed to crosscut calcite veins, resulting in slight displacement (Fig. 46) or fragmentation (Fig. 48) of the preexisting vein. The significance of this vein is not yet clear.

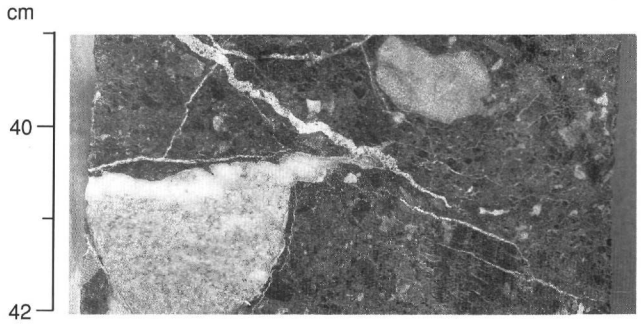

Figure 46. Clast offset along a calcite vein at Interval 149-899B-21R-4, 39-42 cm.

Discussion

The deformation history of Unit IV is partly preserved within the primary texture of the brecciated units, as well as in the post-emplacement fracturing and veining of the rock. The angularity of the fragments and clasts within the breccia units, the in-situ fragmentation and grain trails within the matrix, and the scarcity of ductile deformation within the matrix all point to a dominant ongoing brittle process during emplacement. The presence of solitary and symmetric tails on fractured clasts points to the translation and rotation of grains during breccia emplacement. The overall texture of the matrix might be described as "cataclastic" in the broadest sense, as it is characterized by brittle fracture and grain-size reduction. In tectonic settings, this fabric indicates shear deformation under low normal stress conditions, typically resulting from high fluid pressures.

The rare occurrences of grain flow within an apparently ductile medium (e.g., Interval 149-899B-26R-1, 22-45 cm) and ductile shear zones (Interval 149-899B-28R-1, 110-128 cm) point to local heterogeneities in rheology, possibly correlated with local variations in fluid pressure, composition, or degree of alteration.

The degree of deformation and alteration in the sediments intercalated with the breccias, and to a lesser degree in the crystalline rocks, may also be used to constrain the history and mode of emplacement of the breccias. A variety of sedimentary lithologies occurs over relatively short intervals, yet none shows clear evidence for significant shear deformation comparable to that evident in the breccia formation. Moreover, the mineralogy of the sediments suggests that they have not been thermally altered. This demonstrates that the relatively high-temperature mylonitization evident within several isolated crystalline blocks occurred prior to the breccia formation. Although some contacts between the breccias and sediment do suggest a small degree of mixing between them, the sedimentary units do not appear to have been brecciated. These observations point to relatively low-temperature conditions during emplacement, with only minor shear at the breccia/sediment boundaries. However, the sand-sized soft serpentine is clearly deformed, and critical intervals may have been missed because of limited core recovery, which restricted these interpretations.

Finally, the sequence of events in which the breccia units were deformed can be deduced from the superposition of textures and from the sediment ages. The primary textures of clasts within the breccias indicate serpentine recrystallization and a low-grade metamorphic event that mostly overprinted any prior deformation. However, before these two events, some evidence exists for the basement having undergone a structural evolution comparable to that interpreted for the basement rocks at Site 897 (see "Site 897" chapter, this volume). Subsequent brittle deformation and grain fragmentation accompanying the formation of the breccias have resulted in grain-size reduction

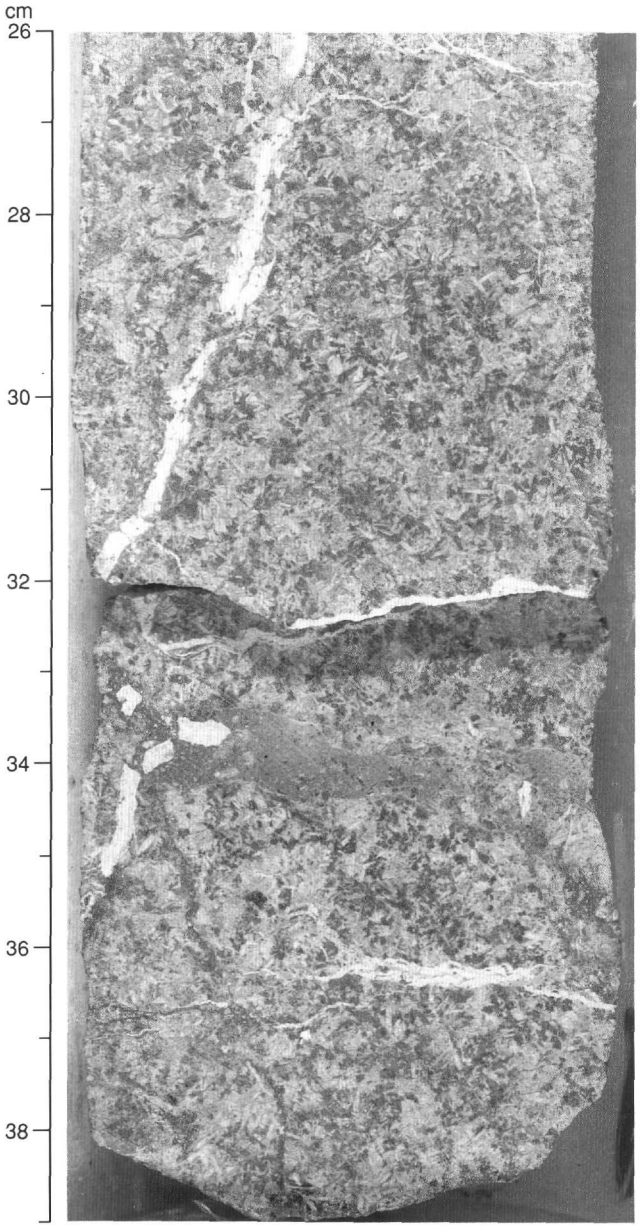

Figure 47. Vein with clastic texture in diabase near base of Hole 899B (Interval 149-899B-35R-1, 26-39 cm), showing fragmentation of preexisting calcite vein.

and nearly complete lithologic mixing. The ensemble was fractured and veined at least once following lithification. In addition, there is a notable lack of veins within the sediments which may indicate that the fracturing and veining in the breccia may have predated the juxtaposition of the breccia and sediments. Alternatively, the lack of veins in the sediments may indicate more about the source of the vein fluids or the ease with which the two units fractured, than about the timing of emplacement. The ages of the sediments suggest an age no older than Barremian for emplacement of the serpentinized peridotite in Core 149-899B-34R and no older than early Aptian for emplacement of the Upper Breccia Unit (see "Lithostratigraphy and Petrology" section, this chapter). This is consistent with emplacement during the last stages of rifting along the western Iberia margin.

ORGANIC GEOCHEMISTRY

Concentrations of calcium carbonate and organic carbon were measured in samples obtained regularly from Holes 899A and 899B.

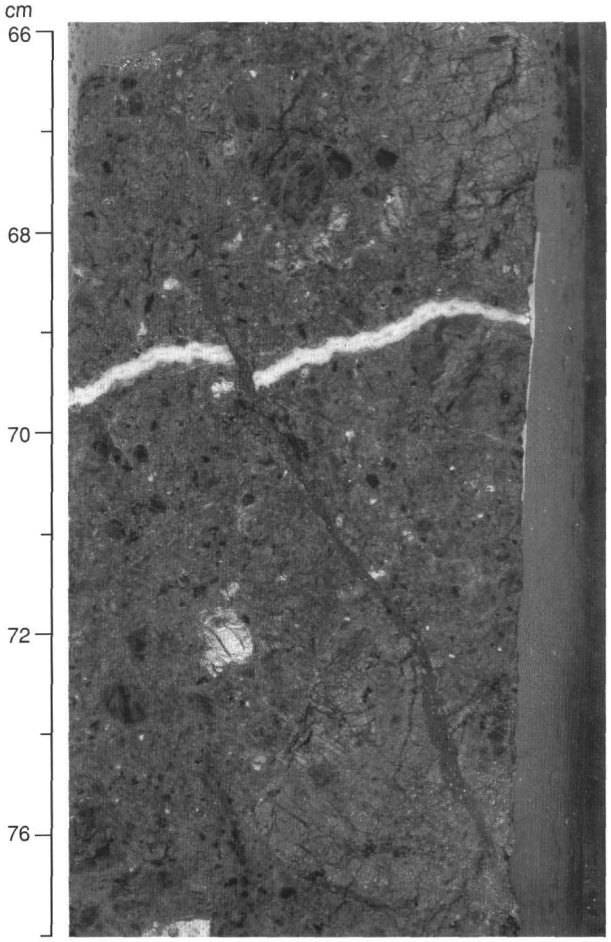

Figure 48. Vein with clastic texture crosscutting and offsetting preexisting calcite vein at Interval 149-899B-16R-2, 66-77 cm.

Atomic C/N ratios of organic matter were employed to determine the type of organic matter contained within the sediments. Routine monitoring of headspace gas contents, done for drilling safety, yielded information that is interesting to contrast with results from Sites 897 and 898.

Concentrations of Inorganic and Organic Carbon

In sediments from Site 899, concentrations of carbonate carbon vary between a high of 9.3% to essentially 0% (Table 14), equivalent to 77% to 0% $CaCO_3$, respectively, assuming that all of the carbonate is present as pure calcite. The variability in carbonate content reflects a history of generally low biological productivity and deposition of hemipelagic sediments below the CCD, combined with delivery of carbonate-rich turbiditic sediments initially deposited in shallower waters.

Concentrations of organic carbon were measured on a subset of sediment samples from the upper part of Hole 899A, plus one sample from near the bottom of Hole 899B. The absence of significant amounts of headspace methane in Site 899 sediments suggested that organic carbon concentrations would be low and, therefore, few organic carbon measurements were performed. Indeed, concentrations are low in nearly all of the Site 899 samples (Table 14). Lithologic Unit I, a sequence dominated by late to early Pliocene turbidites, averages 0.3% organic carbon. This average is approximately the same as the average of 0.2% calculated from DSDP Legs 1 through 31 by McIver (1975). The equivalent lithologic unit at Sites 897 and 898 contained 0.5% to 0.6% organic carbon (see "Site 897" and "Site

Table 14. Concentrations of inorganic carbon in sediments and rocks from Holes 899A and 899B.

Core, section, interval (cm)	Depth (mbsf)	Inorg. C (%)	$CaCO_3$ (%)	Lithologic unit
149-899A-				
1R-1, 48–49	81.98	2.4	20.3	Unit I: nannofossil ooze, silty clay, and fine sand
1R-1, 73–74	82.23	0.3	2.7	
1R-1, 84–85	82.34	2.7	22.4	
1R-1, 112–113	82.62	5.3	44.1	
1R-2, 20–21	83.20	8.1	67.2	
2R-1, 48–49	91.58	2.9	24.1	
2R-1, 69–70	91.79	1.8	15.3	
2R-2, 16–17	92.76	4.6	38.6	
3R-1, 33–34	101.13	0.7	5.7	
3R-2, 92–93	103.22	3.9	32.7	
3R-2, 146–147	103.76	2.4	19.9	
3R-3, 110–111	104.90	6.8	56.4	
4R-1, 107–108	111.47	1.0	8.7	
4R-1, 118–119	111.58	0.6	4.7	
4R-2, 48–49	112.38	1.0	7.9	
4R-2, 115–117	113.05	9.3	77.2	
5R-2, 101–102	122.61	5.8	48.1	
6R-2, 53–54	131.73	2.9	24.3	
6R-2, 113–114	132.33	4.9	40.5	Subunit IIA: nannofossil claystone, siltstone, and sandstone
6R-3, 4–5	132.59	8.3	69.0	
6R-4, 25–26	134.30	1.5	12.4	
6R-4, 60–61	134.65	3.3	27.2	
7R-1, 34–35	139.34	1.2	9.6	
7R-1, 48–49	139.48	4.5	37.6	
7R-1, 60–61	139.60	4.7	39.2	
8R-2, 65–66	150.85	4.6	38.2	
9R-1, 1 7–18	158.47	0.9	7.7	
9R-3, 13–14	161.43	8.0	66.2	
9R-3, 67–68	161.97	8.3	69.4	
10R-1, 60–61	168.60	3.2	26.5	
11R-2, 12–13	179.22	5.0	41.9	
13R-CC, 4–5	197.04	3.5	29.5	
14R-2, 69–70	208.79	5.2	43.4	
15R-2, 2–3	217.82	8.7	72.5	Subunit IIB: nannofossil chalk, silty claystone, and sandstone
15R-2, 9–10	217.89	6.5	53.9	
15R-2, 48–49	218.28	5.4	45.0	
15R-3, 2–3	219.32	3.7	30.6	
15R-3, 5–6	219.35	0.8	6.6	
16R-1, 11–12	226.01	5.5	45.9	
16R-1, 49–50	226.39	2.8	23.7	
16R-1, 97–98	226.87	0.2	1.5	
16R-2, 46–47	227.86	0.2	1.3	
149-899B-				
1R-1, 55–56	231.05	0.5	4.3	
1R-2, 70–71	232.70	0.4	2.9	
2R-1, 28–29	235.08	0.2	1.7	
2R-1, 46–47	235.26	3.6	29.6	
2R-2, 84–85	237.14	4.5	37.7	
3R-1, 49–50	244.89	3.0	24.7	
3R-2, 117–118	247.07	2.2	18.1	
3R-3, 46–47	247.86	1.4	11.6	
3R-4, 48–49	249.38	3.5	29.5	
4R-1, 34–35	254.34	0.3	2.6	
4R-2, 61–62	256.11	1.6	13.2	
4R-2, 86–87	256.36	3.6	29.6	
4R-5, 19–20	260.19	1.6	13.6	
5R-4, 129–130	269.49	2.0	16.9	
6R-1, 66–67	274.06	1.9	16.2	
6R-1, 114–115	274.54	3.1	26.1	
6R-2, 77–78	275.67	5.5	45.4	
6R-3, 143–144	277.83	0.3	2.5	
6R-6, 23–24	281.13	0.3	2.7	
7R-6, 68–69	291.18	0.3	2.4	
7R-7, 26–27	292.26	0.6	5.3	
8R-2, 46–47	294.56	1.9	15.8	
8R-3, 122–123	296.82	2.6	21.5	
8R-4, 3–4	297.13	0.2	1.5	
9R-2, 110–111	304.90	2.6	21.4	
9R-3, 48–49	305.78	2.5	20.6	
9R-3, 84–85	306.14	2.7	22.2	
9R-4, 62–63	307.42	4.5	37.8	
10R-1, 57–58	312.57	0.2	1.4	
10R-1, 82–83	312.82	5.6	47.0	
10R-4, 146–147	317.96	0.2	1.4	
11R-1, 82–83	322.42	3.2	26.7	
11R-1, 116–117	322.76	3.2	26.4	
11R-1, 139–140	322.99	0.2	1.9	
11R-2, 33–34	323.43	3.2	26.8	
12R-1, 55–56	331.75	0.3	2.2	
12R-2, 21–22	332.91	0.1	0.7	
12R-2, 140–141	334.10	5.4	45.2	
13R-1, 55–56	341.45	1.9	15.5	
13R-2, 26–27	342.66	0.3	2.8	
13R-2, 122–123	343.62	3.4	28.6	
13R-5, 76–77	347.66	0.1	0.4	
14R-1, 54–55	351.14	1.0	8.0	
14R-4, 106–107	356.16	3.8	31.4	
14R-5, 101–102	357.61	0.5	4.4	
15R-1, 30–31	360.50	0.1	0.7	Subunit IIIA: claystone
15R-2, 70–71	362.40	0.1	0.7	
15R-3, 53–54	363.73	0.1	0.8	

Note: Concentrations of calcium carbonate were estimated from the inorganic carbon values, assuming all of the inorganic carbon is present as $CaCO_3$.

898" chapters, this volume). The two principal sources of organic matter in oceanic sediments are marine algal production and land plant detritus supplied by rivers and winds. Algal organic matter is typically oxidized and largely recycled during and shortly after settling to the seafloor (e.g., Suess, 1980; Emerson and Hedges, 1988). The land-derived organic matter that is delivered to deep-sea sediments is generally the less reactive material that survives the transport to the ocean. The organic carbon found in Unit I at Site 899 evidently had been substantially oxidized prior to sedimentation and, consequently, is not very reactive.

Characterization of Organic Matter Source

Organic C/N ratios were measured in selected Site 899 samples to determine the source of the organic matter. Algal organic matter generally has C/N ratios of between 5 and 10, whereas organic matter derived from land plants has values between 20 and 100 (e.g., Emerson and Hedges, 1988; Meyers, in press). Variable C/N ratios of samples from Unit I and the uppermost part of Unit II (Table 15) indicate that some samples have a predominantly marine source for their organic matter, whereas other samples contain mostly terrigenous organic matter. The C/N values of some samples are low (<5). These values probably are an artifact of the low carbon contents, combined with the tendency of clay minerals to absorb ammonium ions that were generated during the degradation of organic matter (Müller, 1977). Consequently, the C/N ratios in samples especially low in organic carbon are not accurate indicators of organic matter source.

The sample selected from near the bottom of Unit III (149-899B-15R-2, 70-71 cm) was a red brown Eocene claystone that contained burrows filled with black claystone. The organic carbon content of this sample is 0.31%, and the organic C/N ratio is 6.2 (Table 15). The black infilling material evidently is rich in marine organic matter that has been diluted by the red brown claystone matrix in this sample.

Headspace Gases

Concentrations of headspace methane were low throughout Site 899 (Table 16). These low concentrations contrast with the high levels of biogenic methane found in the upper, turbiditic units at Sites 897 and 898 (see "Site 897" and "Site 898" chapters, this volume). It is possible that the uncored upper 80 m of sediment at Site 899 contained elevated headspace gas concentrations, but this remains unknown. The generally low amounts of organic matter, and its inferred inert character in sediments recovered from Site 899, evidently preclude methanogenesis. Shallower sediments may have similarly been low in organic matter and, therefore, low in methane concentrations. In addition, Claypool and Kvenvolden (1983) observed that the presence of interstitial sulfate inhibits methanogenesis in marine sediments, and sulfate concentrations were high throughout the recovered Site 899 sediments (see "Inorganic Geochemistry" section, this chapter).

INORGANIC GEOCHEMISTRY

Twelve interstitial-water samples were collected at Site 899 from 84.4 to 346.7 mbsf. Whole-round samples were collected from the

Table 15. Concentrations of organic carbon and C/N ratios of selected samples from Site 899.

Core, section, interval (cm)	Depth (mbsf)	Tot. C (%)	Inorg. C (%)	Org. C (%)	Nitrogen (%)	Sulfur (%)	Org. C/N	Org. C/S
149-899A-								
1R-1, 48–49	81.98	3.51	2.44	1.07	0.08	0.00	13.4	
1R-1, 73–74	82.23	0.37	0.33	0.04	0.02	0.18	2.0	0.2
1R-1, 84–85	82.34	2.81	2.69	0.12	0.01	0.10	12.0	1.2
1R-1, 112–113	82.62	5.52	5.29	0.23	0.04	0.00	5.7	
1R-2, 20–21	83.20	8.18	8.07	0.11	0.01	0.00	11.0	
2R-1, 48–49	91.58	3.13	2.89	0.24	0.05	0.05	4.8	4.8
2R-1, 69–70	91.79	2.15	1.84	0.30	0.06	0.04	5.0	7.5
2R-2, 16–17	92.76	4.66	4.63	0.03	0.02	0.02	1.0	1.0
3R-1, 33–34	101.13	0.68	0.69	0.00	0.01	0.03	0.0	0.0
3R-2, 92–93	103.22	4.13	3.93	0.20	0.04	0.00	5.0	
3R-2, 146–147	103.76	2.53	2.39	0.14	0.03	0.02	4.6	7.0
3R-3, 110–111	104.90	6.90	6.77	0.13	0.03	0.00	4.3	
4R-1, 118–119	111.58	1.15	0.57	0.58	0.03	0.02	19.0	29.0
4R-2, 48–49	112.38	1.19	0.95	0.24	0.05	0.03	4.8	8.0
4R-2, 115–117	113.05	9.40	9.27	0.13	0.02	0.02	6.5	6.5
5R-2, 101–102	122.61	5.96	5.78	0.18	0.03	0.02	6.0	9.0
6R-2, 53–54	131.73	2.96	2.92	0.04	0.03	0.02	1.0	2.0
6R-2, 113–114	132.33	5.01	4.86	0.15	0.03	0.01	5.0	15.0
6R-3, 4–5	132.59	8.37	8.28	0.09	0.02	0.04	4.0	2.0
6R-4, 25–26	134.30	2.85	1.49	1.36	0.04	0.05	34.0	27.2
6R-4, 60–61	134.65	3.24	3.26	0.00	0.04	0.02	0.0	0.0
149-899B-								
15R-2, 70–71	362.40	0.40	0.09	0.31	0.05	0.13	6.2	2.4

Note: Organic carbon concentrations were estimated from the difference between total carbon and inorganic carbon values. C/N weight ratios were calculated from concentrations of organic carbon and total nitrogen, respectively.

Table 16. Results of gas chromatography and analyses of headspace gas from Holes 899A and 899B.

Core, section, interval (cm)	Depth (mbsf)	C_1
149-899A-		
1R-3, 0–5	84.50	5
2R-2, 0–5	92.60	5
3R-3, 0–5	103.80	4
4R-2, 0–5	111.90	5
5R-3, 0–5	123.10	5
6R-3, 0–5	132.55	5
7R-1, 10–15	139.10	4
8R-2, 0–5	150.20	4
9R-2, 0–5	159.80	4
10R-1, 0–5	168.00	5
11R-2, 0–5	179.10	4
13R-CC, 3–7	197.03	4
14R-3, 0–5	209.60	5
15R-5, 0–5	222.30	4
16R-2, 0–5	227.40	5
149-899B-		
1R-1, 145–150	231.95	4
2R-3, 0–5	237.80	4
3R-6, 0–5	251.90	4
4R-2, 0–5	255.50	4
5R-4, 0–5	268.20	4
6R-5, 0–5	279.40	4
7R-6, 0–5	290.50	4
8R-6, 0–5	300.10	4
9R-5, 0–5	308.30	4
10R-4, 145–150	317.95	4
11R-3, 0–5	324.60	4
12R-4, 0–5	335.70	4
13R-5, 0–5	346.90	4
14R-4, 0–5	355.10	4
15R-3, 0–5	363.20	4

Note: Concentrations of methane (C_1) are given in parts per million and are at the limit of detection. Heavier gases were not measureable in Site 899 headspace samples.

first two cores and from every third core thereafter. Interstitial-water samples spanned lithostratigraphic Unit I through Subunit IIB. Results from the shipboard interstitial-water analyses are presented in Table 17.

The concentration of sulfate remains nearly constant (between 18.5 and 19.9 mM) from 84.4 to 255.3 mbsf, where concentrations begin to decrease slightly to a minimum of 15.5 mM in the deepest sample (Fig. 49A). Sulfate has been depleted with respect to seawater, indicating that sulfate reduction probably occurred in the shallower sediments. The absence of a negative gradient in the upper cores indicates that the zone of sulfate reduction was not sampled (i.e., it lay at a shallower depth).

Values of alkalinity remain nearly constant between 84.4 and 123.0 mbsf and increase to a maximum of 9.4 mM at 227.3 mbsf (Fig. 49B). This increase in alkalinity results from anaerobic organic carbon degradation (Gieskes, 1974, 1983). Alkalinity decreases below 227.3 mbsf to about 7 mM at 290.3 mbsf.

The concentration of ammonia generally decreases with depth from a value of ~500 µM at 84.4 mbsf to 157 µM at 346.7 mbsf (Fig. 49C). Fluctuations in the profile indicate alternating zones of production and removal. Ammonia concentrations are elevated with respect to oxic seawater in the first interval sampled; thus, the observed negative gradient below 84.4 mbsf suggests that a zone of ammonia production was present above the shallowest interval sampled at this site.

Concentrations of dissolved iron increase from 43 µM at 84.4 mbsf to a maximum of 164 µM at 123.0 mbsf (Fig. 49D). Below the maximum, concentrations of iron decrease to nearly zero between 179.0 and 255.3 mbsf, but show a slight increase at 290.3 mbsf.

Concentrations of dissolved manganese generally increase downhole (with the exception of the sample from Section 149-899A-14R-2 at 209.5 mbsf) from 4 µM at 84.4 mbsf to 45 µM at 290.3 mbsf (Fig. 50A).

Concentrations of calcium increase with depth from values near those for present-day bottom water at 84.4 mbsf to 26.8 mM at 346.7 mbsf (Fig. 50B). Concentration of magnesium remains near bottom-water values (54-57 mM) from 84.4 to 178.9 mbsf (Fig. 50C). Below 178.9 mbsf, concentration of magnesium decreases to about 44 mM at 232.0 mbsf and remains low to 346.7 mbsf.

Concentrations of potassium generally decrease downhole, from a maximum of 9.9 mM at 92.6 mbsf to a minimum of 4.3 mM at 346.7 mbsf, with some narrow zones of release and removal indicated by fluctuations in the profile (Fig. 50D).

Concentrations of silica increase with depth to a maximum value of greater than 1200 µM at 209.4 mbsf. Alternating zones of release and removal have produced another peak at 290.3 mbsf (Fig. 51). Concentrations of silica decrease below 290.3 mbsf to about 580 µM in the bottom two samples (318.7-346.7 mbsf).

Table 17. Interstitial-water data for Site 899.

Core, section, interval (cm)	Depth (mbsf)	Silica (μM)	Ammonia (μM)	Iron (μM)	Manganese (μM)	Sulfate (mM)	Alkalinity (mM)	Chloride (mM)	Calcium (mM)	Magnesium (mM)	Sodium (mM)	Potassium (mM)
149-899A-												
1R-1, 143–150	84.4	246	501	43	4.3	19.9	5.02	570	10.0	53.9	503	9
2R-1, 145–150	92.6	168	507	68	2.7	19.1	4.83	568	10.3	54.3	540	10
5R-1, 143–150	123.0	274	444	164	9.1	18.9	4.80	567	12.3	54.8	544	9
8R-1, 143–150	150.1	339	232			19.3		563	14.9	57.3	537	6
11R-1, 135–150	178.9	449	387	4	32.9	19.1	7.34	569	19.3	54.2	545	7
14R-2, 135–150	209.4	1209	198		10.0	18.5	8.82	559	21.9	50.3	586	8
16R-1, 140–150	227.3	1060	209	0	35.8	19.1	9.38	565	25.0	51.2	582	8
149-899B-												
1R-2, 0–15	232.0	887	326	1	37.4	19.8	9.26	524	22.4	43.9	486	6
4R-1, 130–150	255.3	993	372	2	39.1	19.5	7.79	532	23.1	42.6	492	7
7R-5, 130–150	290.3	1122	258	8	44.7	18.2	6.90	531	24.0	41.4	503	7
10R-5, 70–79	318.7	578	196			17.2		511	26.7	43.5	471	4
13R-4, 130–150	346.7	576	157			15.5		517	26.8	41.8	480	4

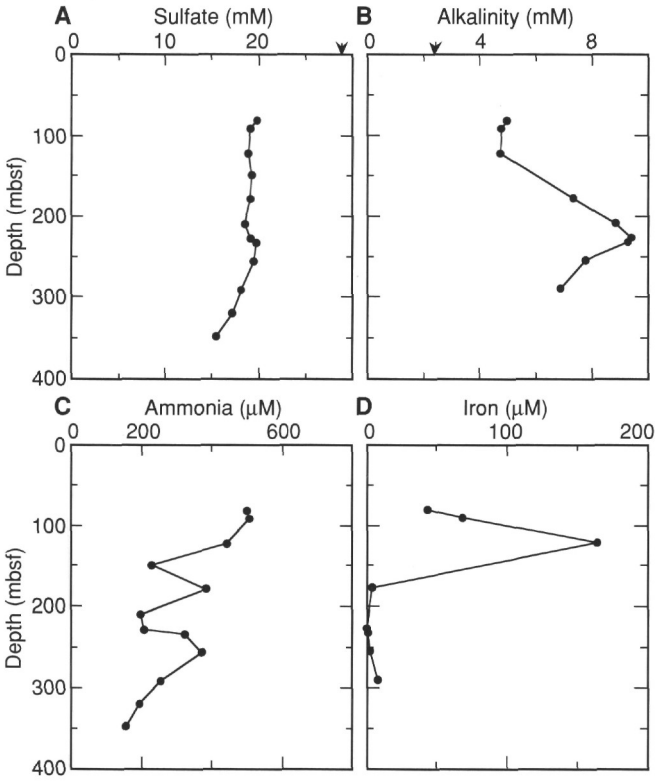

Figure 49. Interstitial-water profiles for Site 899. Arrows indicate typical bottom-water values. **A**. Sulfate. **B**. Alkalinity. **C**. Ammonia. **D**. Iron.

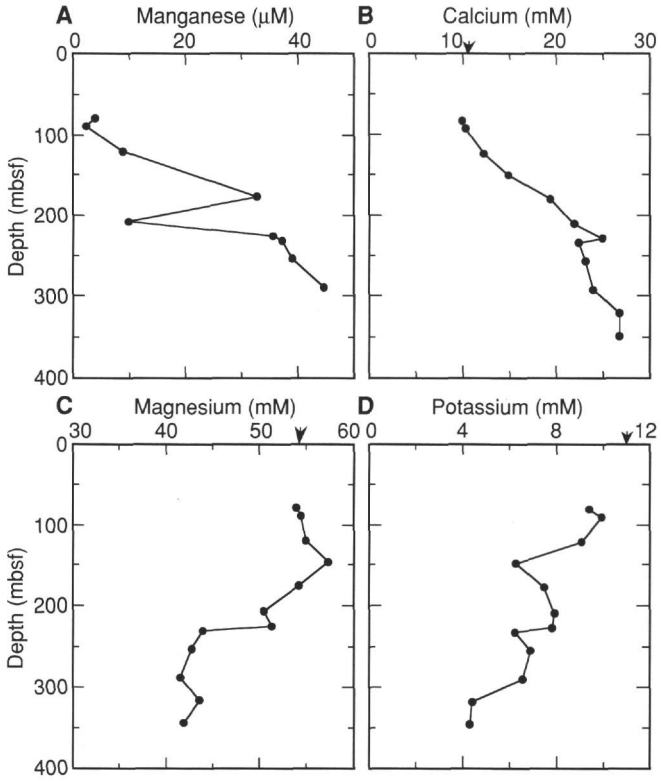

Figure 50. Interstitial-water profiles for Site 899. Arrows indicate typical bottom-water value. **A**. Manganese. **B**. Calcium. **C**. Magnesium. **D**. Potassium.

Concentrations of chloride show a slight enrichment with respect to bottom water from 84.4 to 227.3 mbsf, but show slight depletion with respect to bottom water between 232.0 and 346.7 mbsf (Table 17).

Concentrations of sodium increase from the interval sampled at 84.4 mbsf to a broad maximum between 209.4 and 227.3 mbsf (Table 17). Concentrations of sodium decrease below 227.3 mbsf to values near those of typical bottom-water concentrations.

PHYSICAL PROPERTIES

Introduction

Measurements of whole core taken at Site 899 included magnetic susceptibility, Gamma-Ray Attenuation Porosity Evaluator (GRAPE) bulk density, and thermal conductivity. Compressional-wave velocities were measured in split cores with the Digital Sound Velocimeter (DSV) in unlithified sediments and in discrete samples with the Hamilton Frame Velocimeter in consolidated sediments and crystalline rock. Undrained shear-strength was measured in split sediment cores, and electrical resistivity was measured in split sediment cores and drilled "minicores" from crystalline rock. Index properties were calculated from wet and dry masses and wet and dry volumes.

Index Properties

Index properties were determined using gravimetric methods (Table 18; Fig. 52). The estimated uncertainties for density and porosity are ±0.02 g/cm^3 and ±2%, respectively. Bulk and grain densities and porosity show great variability downhole. Offsets and changes in slope can be correlated with distinct changes in lithology. Gravimetrically determined bulk densities increase from a low of 1.5 g/cm^3 at the top of the cored interval of Hole 899A (81.5 mbsf) to about 1.9 g/cm^3 at a depth of 170 mbsf, with a corresponding decrease in

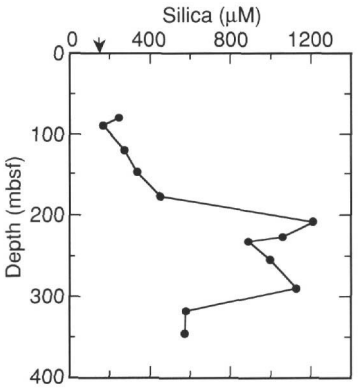

Figure 51. Interstitial-water profile of silica for Site 899. Arrow indicates typical bottom-water value.

porosity from about 70% to 50%. Grain densities over this range are uniform and average 2.8 g/cm^3.

Between 170 and 230 mbsf, bulk densities and porosities are scattered. A zone of high bulk densities and low porosities between 200 and 240 mbsf, at the base of Hole 899 A, lies below the contact between lithostratigraphic Subunits IIA and IIB. Grain density through this zone is uniform.

Just below 230 mbsf the bulk densities are lower, and the porosities higher, than in Unit I. Bulk density then increases from about 1.85 g/cm^3 at 230 mbsf to 2.15 g/cm^3 at 370 mbsf (bottom of Unit III), while porosity decreases from 50% to 40%. Grain densities maintain an average value near 2.8 g/cm^3 over this range.

Feldspathic sandstones at the base of Unit III yield relatively low bulk densities and high porosities. Grain densities are unusually high in these sediments samples, which may contain ferruginous minerals and basaltic clasts.

The boundary between lithostratigraphic Units III and IV (369.9 mbsf) is marked by abrupt changes in all index properties (Fig. 52). Porosity decreases sharply from 40% to 0%-10% at a depth of 390 mbsf, and grain density decreases to about 2.58 g/cm^3. Bulk density dominantly reflects the decrease in porosity; it approaches and sometimes exceeds the calculated grain density at this depth (this probably indicates the range of measurement error at 0% porosity). The downhole trend in grain density appears to correlate with the degree of calcitization of the serpentinized peridotite breccia unit that makes up Unit IV, reflecting differences in the densities of calcite (2.72 to 2.9 g/cm^3) and serpentine (2.55 g/cm^3).

GRAPE Measurements

Bulk densities were also estimated from whole-core GRAPE measurements taken in all sections recovered from Holes 899A and 899B. In the sedimentary section, the maximum GRAPE densities within an interval of about 10 m give the best estimate of the corresponding gravimetrically determined bulk density (Boyce, 1973; Gealy, 1971).

The visually estimated maximum densities are indicated by the curve in Figure 52. In the upper sedimentary section, between 81.5 and 131.6 mbsf, the average estimated density is 1.9 g/cm^3. Below 131.7 mbsf, which coincides with the boundary between lithostratigraphic Unit I and Subunit IIA(see "Lithostratigraphy and Petrology" section, this chapter), the bulk density decreases abruptly to an average of 1.8 g/cm^3 and remains fairly constant down to a depth of about 180 mbsf. Between 200 and 365 mbsf, a net increase in bulk density from 1.8 to 2.0 g/cm^3 can be seen. Below 365 mbsf, the cores are highly fractured and do not fill the core liner, which prevented us from applying an adequate volumetric correction (see "Explanatory Notes" chapter, this volume). This is reflected in the large scatter observed in the data points.

Electrical Resistivity

Electrical resistivity was measured at intervals of 0.5 to 0.75 m in all split cores from the sedimentary section and in drilled minicores in the breccia and other hard rocks. Formation factors were calculated for the interval down to 370 mbsf.

An average formation factor of 3.5 characterizes the upper sedimentary section between 80 and 130 mbsf (Fig. 52). The latter depth

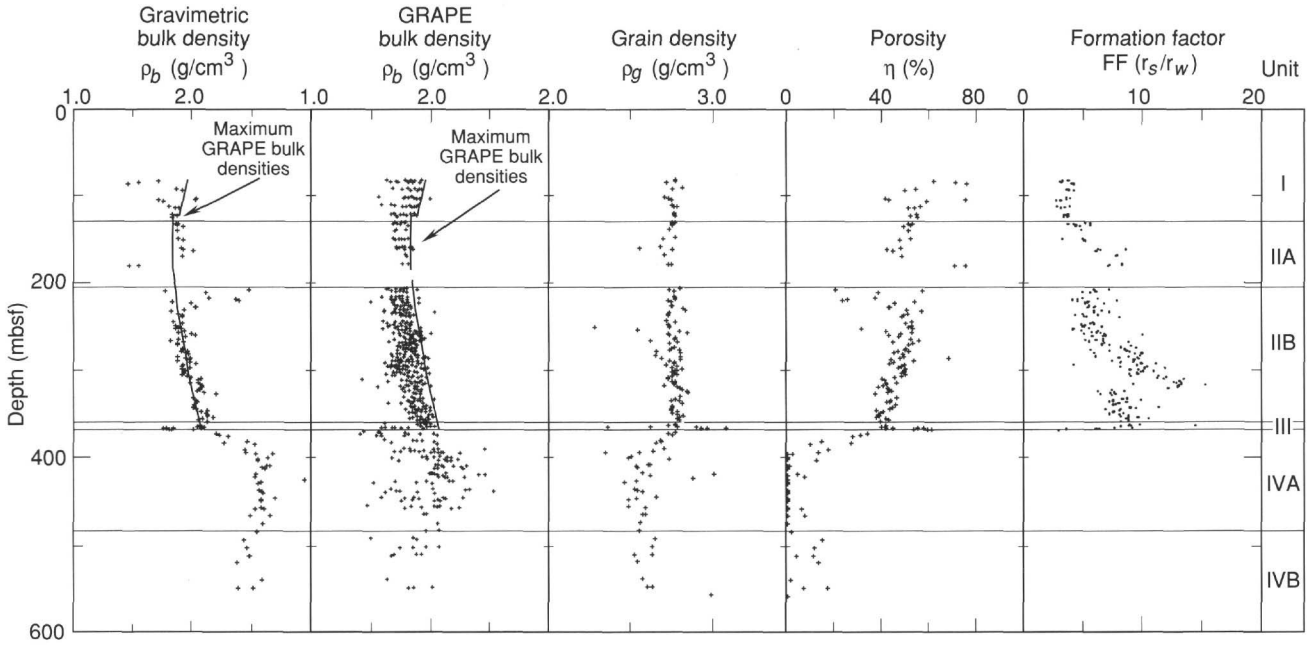

Figure 52. Gravimetrically determined and GRAPE-estimated bulk densities, grain density, porosity, and formation factor measurements in cores from Holes 899A and 899B. Electrical resistivity measurements in basement rocks are shown in Figure 53. The lines on the bulk density graphs are the visually determined maximum GRAPE bulk density.

Table 18. Index properties data for Site 899.

Core, section, interval (cm)	Depth (mbsf)	Sample wet mass (g)	Sample wet vol. (cm^3)	Sample dry mass (g)	Sample dry vol. (cm^3)	Bulk density (g/cm^3)	Grain density (g/cm^3)	Porosity (%)	Water content (% dry mass)
149-899A-									
1R-1, 113–114	82.63	8.66	5.06	6.64	2.38	1.71	2.80	61.26	31.88
1R-2, 70–71	83.70	8.78	5.70	7.17	2.57	1.54	2.80	70.89	23.47
1R-3, 74–75	85.24	8.93	6.17	8.73	3.18	1.45	2.74	75.44	2.38
2R-1, 60–61	91.70	8.57	4.61	6.28	2.22	1.86	2.84	54.01	38.27
2R-2, 90–92	93.50	8.59	4.49	6.67	2.40	1.91	2.78	49.53	30.13
3R-1, 70–71	101.50	13.70	6.74	8.60	3.17	2.03	2.73	40.78	62.78
3R-2, 89–90	103.19	13.65	7.97	10.54	2.83	1.71	3.76	74.77	30.90
3R-3, 28–29	104.08	13.50	6.70	10.58	3.86	2.02	2.75	42.49	28.88
3R-3, 100–101	104.80	13.63	7.81	10.83	3.92	1.75	2.77	58.69	27.05
4R-1, 66–68	111.06	14.20	7.89	9.57	3.45	1.80	2.78	55.97	51.05
4R-2, 51–53	112.41	13.71	7.25	9.79	3.52	1.89	2.79	50.97	42.09
4R-2, 98–100	112.88	11.17	6.04	7.68	2.75	1.85	2.81	53.69	47.91
5R-1, 94–95	121.04	13.01	7.11	8.91	3.21	1.83	2.79	54.30	48.51
5R-2, 116–118	122.76	10.03	5.36	6.86	2.47	1.87	2.79	51.95	48.69
5R-3, 54–56	123.64	14.75	8.07	10.17	3.65	1.83	2.80	54.71	47.44
6R-1, 104–106	130.74	12.12	6.44	8.51	3.07	1.88	2.78	51.19	44.63
6R-2, 96–97	132.16	13.26	7.11	9.29	3.33	1.86	2.80	52.63	44.97
6R-3, 81–82	133.36	12.66	6.78	8.80	3.18	1.87	2.78	51.93	46.17
6R-4, 28–29	134.33	13.27	6.92	9.57	3.46	1.92	2.78	49.00	40.63
7R-1, 70–72	139.70	12.08	6.44	8.55	3.10	1.87	2.76	51.12	43.44
8R-1, 44–46	149.14	13.75	7.31	9.71	3.48	1.88	2.80	51.76	43.78
8R-2, 45–47	150.65	14.35	7.48	10.33	3.81	1.92	2.72	47.25	40.92
9R-1, 43–44	158.73	14.01	7.35	10.03	3.72	1.90	2.70	47.47	41.72
9R-2, 43–45	160.23	11.49	5.97	8.32	3.24	1.92	2.57	41.88	40.06
9R-3, 45–47	161.75	12.99	6.49	9.76	3.52	2.00	2.78	44.35	34.70
10R-1, 33–34	168.33	12.84	6.71	9.26	3.40	1.91	2.73	47.95	40.63
11R-2, 28–29	179.38	10.90	7.09	10.37	3.77	1.54	2.75	70.30	5.30
11R-CC, 05–06	179.69	8.73	5.97	8.42	3.04	1.46	2.77	74.94	3.82
14R-1, 104–105	207.64	10.34	4.19	5.65	2.01	2.47	2.83	20.11	88.72
14R-2, 61–63	208.71	12.66	7.15	9.59	3.48	1.77	2.76	57.08	33.57
14R-3, 78–80	210.38	10.47	4.95	6.66	2.40	2.11	2.79	38.13	60.54
15R-1, 61–64	216.91	10.62	4.95	6.65	2.39	2.14	2.79	36.67	63.28
15R-2, 100–101	218.80	10.35	4.39	5.60	2.01	2.36	2.80	25.13	90.65
15R-3, 77–78	220.07	10.33	4.33	5.20	1.88	2.39	2.80	23.01	105.96
15R-4, 65–66	221.45	10.59	5.79	7.25	2.64	1.83	2.75	53.53	48.56
15R-5, 80–81	223.10	10.51	5.29	6.90	2.50	1.99	2.77	44.97	55.30
16R-1, 124–127	227.14	10.49	5.18	6.45	2.34	2.03	2.78	42.76	66.40
16R-2, 59–61	227.99	10.54	5.23	6.65	2.41	2.02	2.77	43.31	61.91
149-899B-									
1R-1, 47–48	230.97	9.60	4.98	6.89	2.43	1.93	2.85	50.41	41.33
1R-2, 64–67	232.64	9.51	5.22	6.38	2.24	1.82	2.86	56.61	51.74
2R-1, 60–61	235.40	9.12	4.84	6.40	2.32	1.88	2.76	50.65	44.76
2R-2, 43–46	236.73	10.60	5.56	7.62	2.78	1.91	2.75	48.86	41.10
2R-3, 97–98	238.77	7.80	4.08	5.46	2.00	1.91	2.75	48.31	45.09
3R-1, 68–69	245.08	9.10	4.94	6.27	2.29	1.84	2.74	52.53	47.59
3R-2, 69–70	246.59	9.37	4.89	6.77	2.42	1.91	2.80	49.93	40.37
3R-3, 132–133	248.72	10.47	5.67	7.24	2.65	1.85	2.75	52.16	46.97
3R-4, 134–137	250.24	10.51	5.60	7.44	2.70	1.88	2.76	51.01	43.42
3R-5, 130–131	251.70	8.43	4.43	5.97	2.60	1.90	2.29	30.92	43.33
3R-6, 80–81	252.70	10.31	5.57	7.12	2.58	1.85	2.76	52.59	47.21
4R-1, 50–51	254.50	8.31	4.31	5.91	2.31	1.93	2.56	41.27	42.73
4R-2, 127–130	256.77	10.71	5.70	7.46	2.66	1.88	2.82	52.32	45.87
4R-3, 70–71	257.70	7.75	3.90	5.56	1.95	1.99	2.87	47.67	41.43
4R-4, 76–77	259.26	9.74	4.83	7.30	2.66	2.02	2.75	42.60	35.09
4R-5, 72–73	260.72	12.87	6.62	9.48	3.45	1.94	2.76	46.90	37.55
5R-1, 50–51	264.20	11.51	6.13	8.10	2.91	1.88	2.80	51.82	44.29
5R-2, 90–92	266.10	14.43	7.95	9.92	3.57	1.81	2.79	55.18	47.89
5R-3, 94–95	267.64	8.85	4.60	6.29	2.39	1.92	2.64	44.31	42.81
5R-4, 66–67	268.86	8.21	4.39	5.59	2.00	1.87	2.81	52.61	49.42
5R-5, 143–146	271.13	11.32	6.05	8.00	2.91	1.87	2.76	51.17	43.67
6R-1, 138–139	274.78	11.59	6.06	8.25	2.97	1.91	2.79	49.65	42.59
6R-2, 133–134	276.23	13.03	6.83	9.45	3.42	1.91	2.77	49.45	39.81
6R-3, 140–141	277.80	14.86	7.61	11.05	4.01	1.95	2.76	46.60	36.19
6R-4, 120–122	279.10	12.74	6.70	9.02	3.21	1.90	2.82	51.15	43.41
6R-5, 110–111	280.50	15.45	7.97	11.33	4.24	1.94	2.68	44.76	38.20
6R-6, 17–19	281.07	10.91	5.58	7.92	2.81	1.96	2.83	48.45	39.67
7R-1, 140–142	284.40	16.53	8.86	11.71	4.39	1.87	2.67	49.02	43.30
7R-2, 132–133	285.82	8.07	4.08	5.84	2.07	1.98	2.83	47.27	40.16
7R-3, 13–14	286.13	14.43	7.46	10.57	2.78	1.94	3.84	67.68	38.35
7R-4, 39–40	287.89	15.66	7.94	11.84	4.38	1.97	2.71	43.74	33.83
7R-5, 52–53	289.52	15.88	8.50	11.16	3.96	1.87	2.83	53.23	44.53
7R-6, 86–87	291.36	14.96	7.54	11.31	4.11	1.98	2.76	44.66	33.83
7R-7, 42–43	292.42	11.18	5.50	8.60	3.09	2.03	2.79	42.90	31.44
8R-1, 45–46	293.05	11.36	5.91	8.10	2.91	1.92	2.79	49.23	42.32
8R-2, 131–132	295.41	13.06	6.82	9.39	3.44	1.91	2.74	48.03	41.10
8R-3, 71–72	296.31	11.25	5.69	8.34	2.97	1.98	2.81	46.81	36.63
8R-4, 81–82	297.91	14.97	7.84	10.80	3.89	1.91	2.78	49.73	40.58
8R-5, 114–115	299.74	11.39	5.86	8.26	2.92	1.94	2.84	49.35	39.84
8R-6, 125–127	301.35	9.68	5.02	6.85	2.46	1.93	2.80	48.99	43.44
8R-7, 59–61	302.19	13.72	7.11	9.94	3.55	1.93	2.81	49.27	39.97
9R-1, 42–43	302.72	12.42	6.44	8.93	3.23	1.93	2.78	48.34	41.10
9R-2, 78–79	304.58	12.71	6.67	9.01	3.25	1.91	2.79	49.90	43.21
9R-3, 125–126	306.55	13.13	6.75	9.61	3.44	1.95	2.81	48.24	38.45
9R-4, 111–112	307.91	16.44	8.26	12.48	4.49	1.99	2.78	45.18	33.27
9R-5, 123–124	309.53	14.68	7.10	11.53	4.20	2.07	2.75	39.60	28.59

Table 18 (continued).

Core, section, interval (cm)	Depth (mbsf)	Sample wet mass (g)	Sample wet vol. (cm^3)	Sample dry mass (g)	Sample dry vol. (cm^3)	Bulk density (g/cm^3)	Grain density (g/cm^3)	Porosity (%)	Water content (% dry mass)
9R-6, 43–45	310.23	15.82	7.72	12.32	4.48	2.05	2.75	40.80	29.74
10R-1, 128–130	313.28	12.61	6.35	9.43	3.37	1.98	2.80	46.02	35.38
10R-2, 116–118	314.66	13.72	6.68	10.67	3.85	2.05	2.78	41.30	29.95
10R-3, 96–98	315.96	13.54	6.58	10.52	3.76	2.06	2.80	41.97	30.07
10R-4, 121–122	317.71	15.22	7.32	12.06	4.34	2.08	2.79	40.11	27.41
10R-5, 43–44	318.43	14.75	7.10	11.67	4.29	2.08	2.73	38.12	27.61
10R-6, 59–60	319.49	14.26	6.94	11.10	3.97	2.06	2.81	42.10	29.81
11R-1, 79–80	322.39	8.53	4.13	6.59	2.33	2.06	2.83	42.50	30.84
11R-2, 74–77	323.84	11.40	5.59	8.72	3.08	2.04	2.84	44.10	32.20
11R-3, 45–46	325.05	9.77	4.66	7.54	2.63	2.10	2.87	42.05	30.98
11R-4, 80–81	326.90	7.68	3.49	6.13	2.13	2.20	2.88	36.73	26.45
12R-1, 47–48	331.67	10.71	5.35	8.07	2.85	2.00	2.83	46.13	34.32
12R-2, 64–65	333.34	10.52	5.19	7.92	2.83	2.03	2.80	43.72	34.41
12R-3, 69–70	334.89	9.29	4.55	6.99	2.49	2.04	2.82	43.24	34.50
12R-4, 52–55	336.22	14.62	7.18	11.23	4.07	2.04	2.77	41.93	31.62
12R-5, 70–71	337.90	13.57	6.75	10.35	3.65	2.01	2.84	45.80	32.60
13R-1, 79–80	341.69	11.68	5.83	8.82	3.18	2.00	2.78	44.30	34.01
13R-2, 60–61	343.00	13.76	6.79	10.53	3.79	2.03	2.78	43.09	32.14
13R-3, 57–58	344.47	8.54	4.03	6.66	2.41	2.12	2.77	37.26	29.54
13R-4, 102–105	346.42	11.09	5.36	8.51	3.08	2.07	2.77	40.12	31.79
13R-5, 50–51	347.40	9.71	4.59	7.62	2.72	2.11	2.81	38.84	28.73
13R-6, 79–80	349.19	9.68	4.57	7.62	2.74	2.12	2.78	37.93	28.30
14R-1, 65–66	351.25	9.14	4.31	7.15	2.55	2.12	2.81	38.63	29.15
14R-2, 96–97	353.06	8.43	3.89	6.65	2.34	2.17	2.85	37.35	28.00
14R-3, 29–30	353.89	11.54	5.55	9.22	3.27	2.08	2.82	41.43	26.31
14R-4, 29–32	355.39	11.33	5.53	8.65	3.09	2.05	2.81	42.58	32.47
14R-5, 69–70	357.29	7.18	3.39	5.51	1.96	2.12	2.82	39.09	31.76
15R-1, 105–107	361.25	12.14	5.90	9.70	3.48	2.06	2.80	41.62	26.32
15R-2, 105–107	362.75	13.93	6.65	11.04	3.96	2.10	2.80	39.54	27.40
15R-3, 109–110	364.29	11.69	5.64	9.08	3.24	2.07	2.81	41.31	30.09
15R-3, 75–77	363.95	12.39	6.07	9.68	3.53	2.04	2.75	41.02	29.31
15R-4, 12–14	364.82	11.45	6.22	7.47	2.56	1.84	2.93	57.26	56.32
15R-4, 125–125	365.95	13.44	6.71	9.95	3.21	2.00	3.12	53.21	36.82
15R-4, 37–38	365.07	8.32	4.76	5.56	2.12	1.75	2.64	54.99	52.36
15R-4, 57–58	365.27	11.49	6.46	8.43	3.55	1.78	2.37	44.18	38.11
15R-5, 75–78	366.95	11.24	6.19	7.23	2.46	1.82	2.96	59.06	58.65
15R-5, 105–107	367.25	10.55	5.87	6.67	2.24	1.80	3.00	60.81	61.54
16R-1, 76–78	370.56	18.58	8.44	11.29	4.06	2.20	2.80	33.58	68.52
16R-3, 73–75	373.12	24.56	11.05	20.99	7.65	2.22	2.75	30.46	17.73
16R-4, 118–121	374.36	21.47	9.32	19.02	6.85	2.30	2.78	27.12	13.41
17R-1, 82–84	380.22	17.54	7.13	15.81	5.87	2.46	2.70	14.09	11.38
17R-2, 50–52	381.33	25.01	11.07	22.33	8.26	2.26	2.71	26.56	12.49
17R-3, 73–76	383.03	26.90	10.68	25.22	9.41	2.52	2.68	9.81	6.92
18R-1, 74–76	389.84	24.60	10.09	22.87	8.37	2.44	2.73	17.31	7.86
18R-3, 70–72	392.35	22.47	9.18	21.03	7.91	2.45	2.66	12.97	7.11
18R-4, 82–85	393.95	29.50	11.66	28.63	11.16	2.53	2.57	2.32	3.15
18R-5, 73–75	394.97	23.93	8.95	23.52	9.95	2.67	2.36	-23.13	1.81
19R-1, 78–81	399.08	26.85	10.21	26.15	10.37	2.63	2.52	-7.20	2.78
19R-2, 64–66	400.35	23.93	9.39	23.13	9.25	2.55	2.50	-3.22	3.59
19R-3, 80–82	401.95	27.78	10.89	27.33	9.90	2.55	2.76	12.09	1.71
20R-1, 79–82	408.49	31.20	11.79	30.32	11.51	2.65	2.63	-0.72	3.01
20R-1, 89–91	408.59	26.48	10.09	25.99	9.86	2.62	2.64	0.73	1.96
20R-2, 77–79	409.95	24.34	9.44	23.76	9.31	2.58	2.55	-1.70	2.53
20R-3, 74–76	411.33	23.68	9.09	23.25	9.08	2.61	2.56	-2.88	1.92
21R-1, 70–73	417.80	25.49	10.08	24.37	9.40	2.53	2.59	4.11	4.77
21R-2, 57–60	418.81	30.43	9.97	30.31	9.96	3.05	3.04	-0.44	0.41
21R-3, 72–75	420.20	24.05	9.54	23.02	8.73	2.52	2.64	7.23	4.64
22R-1, 59–62	426.89	26.49	10.31	25.71	10.09	2.57	2.55	-1.37	3.15
22R-2, 80–83	428.56	27.61	10.81	26.26	10.59	2.55	2.48	-5.08	5.34
21R-5, 78–81	423.20	27.75	9.45	27.44	9.43	2.94	2.91	-1.39	1.17
23R-1, 74–76	436.34	23.33	9.13	22.68	8.94	2.56	2.54	-1.19	2.97
23R-2, 127–129	438.28	22.52	8.72	21.84	8.53	2.58	2.56	-1.42	3.23
23R-3, 66–72	439.14	16.55	6.38	16.13	6.24	2.59	2.59	-0.56	2.70
24R-1, 64–67	445.94	21.71	8.06	20.84	7.78	2.69	2.68	-0.85	4.33
24R-2, 50–53	447.30	25.62	9.98	24.94	9.80	2.57	2.55	-1.44	2.83
24R-3, 75–78	449.01	17.62	6.86	16.88	6.76	2.57	2.50	-4.82	4.55
25R-1, 82–85	455.52	22.56	8.78	21.93	8.78	2.57	2.50	-4.85	2.98
25R-2, 101–104	457.03	20.25	8.04	18.79	7.19	2.52	2.61	6.03	8.07
25R-3, 73–76	458.20	25.45	9.78	24.49	9.40	2.60	2.61	0.23	4.07
26R-1, 65–68	464.85	25.87	9.78	25.15	9.62	2.65	2.61	-1.91	2.97
26R-2, 33–36	465.97	24.46	9.86	23.21	8.95	2.48	2.59	7.22	5.59
27R-1, 142–145	475.02	23.39	9.04	22.74	8.83	2.59	2.58	-0.75	2.97
28R-1, 74–77	483.64	22.98	9.03	22.24	8.65	2.54	2.57	1.72	3.45
29R-1, 77–82	492.87	22.32	9.19	20.41	7.64	2.43	2.67	14.83	9.73
30R-2, 11–14	502.90	21.59	8.76	20.32	7.67	2.46	2.65	11.42	6.49
31R-1, 75–78	511.25	23.69	9.58	22.29	8.41	2.47	2.65	10.98	6.52
31R-1, 111–114	511.61	27.42	11.04	26.00	10.23	2.48	2.54	3.85	5.67
32R-1, 28–33	520.28	14.89	6.29	14.00	5.46	2.37	2.56	12.83	6.60
34R-1, 31–34	539.21	26.89	10.44	25.51	9.84	2.58	2.59	1.12	5.62
35R-1, 21–24	548.61	28.29	11.87	26.10	9.84	2.38	2.65	16.60	8.72
35R-1, 60–64	549.00	27.57	10.98	25.85	9.87	2.51	2.62	6.84	6.91
37R-1, 8–13	557.68	31.51	10.15	31.30	10.37	3.10	3.02	-4.31	0.70

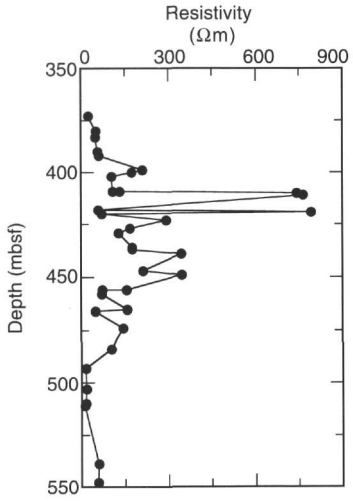

Figure 53. Electrical resistivity measurements in cores of basement rocks from Hole 899B.

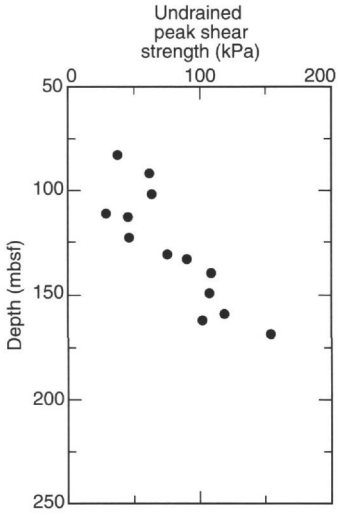

Figure 54. Undrained shear strength measurements in sediment cores from Hole 899A.

corresponds to the boundary between lithostratigraphic Unit I and Subunit IIA(see "Lithostratigraphy and Petrology" section, this chapter). Below this, the formation factor increases downhole to an average of 8 at 180 mbsf. Between 200 and 270 mbsf, values exhibit a larger scatter around a mean of 5.5; this is followed by a steep increase from 8 to 13 in the interval between 270 and 320 mbsf. In the lowermost sedimentary section, the formation factor is scattered around a mean of 8.

Above 400 mbsf as well as below 490 mbsf, electrical resistivity in the brecciated and crystalline rocks of Unit IV (Fig. 53) is relatively low (Cores 149-899B-19R and -28R), with values that range from 10 to 125 Ωm. Between these two zones, electrical resistivities from 150 to 350 Ωm were observed, with three local maxima of about 775 Ωm between 410 and 420 mbsf. Two of these values were measured in large clasts of serpentinized peridotite, rather than breccia, and the third minicore was transected by a large calcite vein.

Undrained Shear Strength

Undrained shear strength was measured in Cores 149-899A-lR to -10R (Fig. 54). Peak shear strength shows a general downhole increase from about 40 kPa at 80 mbsf to about 160 Kpa at 170 mbsf. Variations in peak strength values (e.g., Cores 149-899A-1R through -5R) probably are controlled by lithologic variations.

Acoustic Velocity

Discrete acoustic velocity was measured in sediment samples from each core recovered from Holes 899A and 899B, except for the wash core (Table 19). The DSV was used for Cores 149-899A-1R to -9R (82-159 mbsf) to measure the vertical velocity. The Hamilton Frame Velocimeter was used to measure velocities in sediment samples taken from Cores 149-899A-9R to -899B-15R (159-364 mbsf). Velocities in these samples were measured in three mutually orthogonal directions (see "Explanatory Notes" chapter, this volume). Compressional-wave velocity in crystalline rock from Cores 149-899B-16R to -35R (373-548 mbsf) was measured in minicores in the horizontal direction (H_y) with the Hamilton Frame Velocimeter. Repeated measurements of selected samples and calibration standards suggest an accuracy of 2% to 3% for the velocity measurements.

Discrete acoustic velocity measurements in the sedimentary section show a general increase with depth, from about 1600 m/s at 82 mbsf to 1750 m/s at 364 mbsf (Fig. 55). The vertical velocity shows

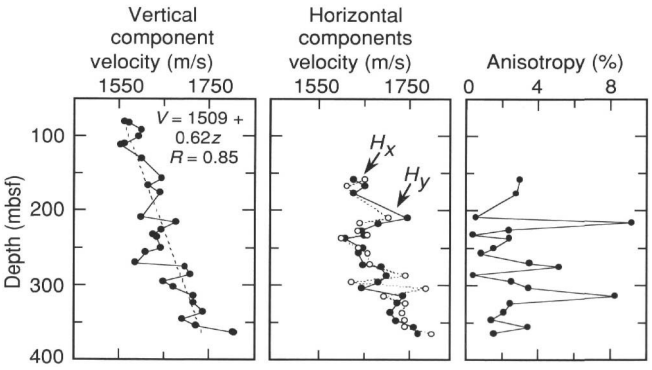

Figure 55. Hamilton Frame velocity and computed anisotropy for the sedimentary sequence in Holes 899A and 899B. The vertical velocity was measured along the axis of the core. Horizontal velocities were measured perpendicular to the core axis (H_x) and normal to the split face of the core (H_y). The downhole increase in the vertical velocity shows a linear trend (dashed line) with a correlation coefficient (R) of 0.85.

a reasonably linear trend having a slope of 0.62 s^{-1}, with a correlation coefficient of 0.85. The horizontal velocities show similar downhole variations. Acoustic anisotropy is generally less than 4%, which is less than the estimated error.

Compressional-wave velocities in Unit IV range from 3000 to 6800 m/s (Fig. 56). Velocities of less than 4000 m/s occur within brown serpentinized breccia at depths of less than 390 mbsf (Cores 149-899B-16R to -18R), and beneath the breccia at depths greater than 490 mbsf (Cores 149-899B-29R to -35R). Samples from intervening depths in Cores 149-899B-19R to -26R mostly have velocities greater than 4400 m/s. The single velocity greater than 6800 m/s in Figure 56 is from a sample in which a 2-cm-wide calcite vein ran along the axis of the minicore.

Magnetic Susceptibility

Magnetic susceptibility was measured at intervals of 3 to 5 cm in all cores collected at Site 899. The results are discussed in the "Paleomagnetism" section (this chapter).

Table 19. Discrete acoustic velocity measurements in cores from Holes 899A and 899B.

Core, section, interval (cm)	Depth (mbsf)	Velocity (m/s)		
		V	H_x	H_y
149-899A-				
1R-1, 110–117	82.63	1573		
1R-2, 43–50	81.97	1564		
2R-2, 43–50	93.07	1600		
3R-1, 100–107	101.80	1593		
4R-1, 62–69	111.02	1563		
4R-2, 82–89	112.72	1554		
5R-2, 120–127	122.80	1455		
6R-1, 101–108	130.71	1602		
9R-1, 37–44	158.67	1645		
9R-1, 42–44	158.72	1610	1660	1638
10R-1,,34–36	168.35	1615	1623	1661
11R-1, 60–61	178.20	1642	1632	1636
14R-3, 78–81	210.39	1600	1714	1755
15R-1, 61–63	216.92	1677	1651	1691
16R-1, 124–127	227.15	1644	1648	1651
149-899B-				
1R-2, 64–67	232.66	1628	1668	1663
2R-2, 43–46	236.75	1634	1609	1617
3R-4, 134–137	250.25	1643	1647	1657
4R-2, 127–130	256.78	1610	1668	1647
5R-5, 143–146	271.14	1588	1673	1659
6R-1, 136–138	274.76	1698	1691	1697
7R-2, 133–135	285.83	1709	1753	1710
8R-2, 132–134	295.42	1649	1633	1691
9R-1, 40–42	302.70	1672	1798	1656
10R-2, 98–100	314.48	1715	1705	1748
11R-2, 74–77	323.85	1716	1753	1736
12R-4, 52–55	336.23	1738	1744	1718
13R-4, 102–105	346.43	1691	1750	1733
14R-4, 29–32	355.40	1722	1750	1770
15R-3, 110–112	364.30	1807	1809	1780
16R-3, 73–75	373.13	3794		
16R-4, 118–121	374.37	3558		
17R-1, 82–84	380.22	3533		
17R-2, 50–52	382.80	3185		
17R-3, 73–76	383.03	3732		
18R-1, 74–76	389.84	3985		
18R-3, 70–72	392.35	3832		
18R-4, 83–85	393.96	4234		
18R-5, 73–75	394.97	4893		
19R-1, 78–91	399.09	4870		
19R-2, 64–66	400.35	4508		
19R-3, 80–82	401.96	4971		
20R-1, 79–82	408.50	5113		
20R-1, 89–91	408.59	4952		
20R-2, 77–79	409.95	5182		
20R-3, 74–76	411.33	5196		
21R-1, 70–73	417.80	4625		
21R-2, 57–60	418.81	6843		
21R-3, 72–75	420.20	4629		
21R-5, 78–81	423.00	5700		
22R-1, 59–62	426.89	4560		
22R-2, 80–83	429.00	4540		
23R-1, 74–76	436.00	4571		
23R-2, 127–129	437.00	4980		
23R-3, 66–72	439.00	4937		
24R-2, 50–53	447.00	4795		
24R-3, 75–78	449.00	4622		
25R-1, 82–85	456.00	5421		
25R-2, 101–104	456.00	4204		
25R-3, 73–76	458.00	4484		
26R-1, 65–68	465.00	4724		
26R-2, 33–36	466.00	4178		
27R-1, 142–145	474.00	4896		
28R-1, 74–77	484.00	4608		
29R-1, 77–82	493.00	3473		
30R-2, 11–14	503.00	3694		
31R-1, 75–78	510.00	3020		
31R-1, 111–114	511.00	3755		
34R-1, 31–34	539.00	4077		
35R-1, 60–64	548.00	4298		

Thermal Conductivity

Thermal conductivity was measured in alternate sections of all cores from Site 899. The mean error associated with these measurements was estimated as ±0.2 W/(m·K). In the sedimentary section, the thermal conductivity values show no significant change with depth.

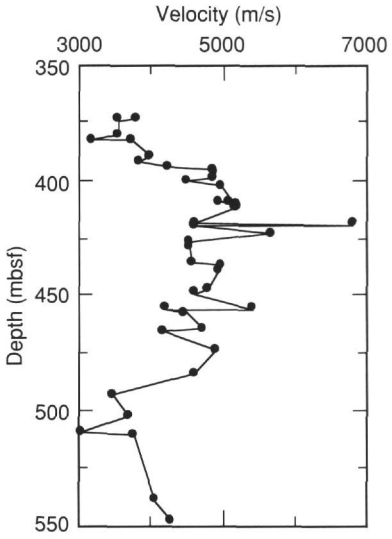

Figure 56. Compressional-wave velocity measurements in minicores of basement rocks from Hole 899B.

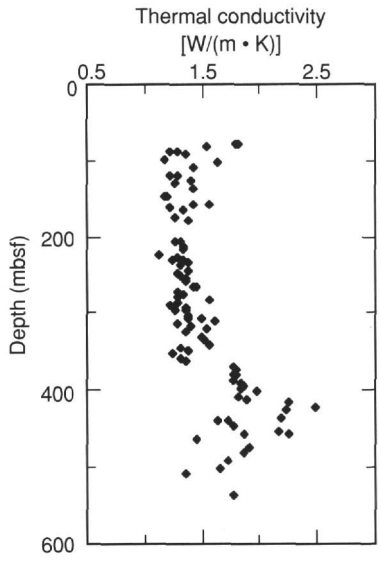

Figure 57. Thermal conductivity measurements on sediments and rocks from Holes 899A and 899B.

Between 80 and 360 mbsf, thermal conductivity values of about 1.35 W/(m·K) were observed (Fig. 57; Table 20). At 370 mbsf, an abrupt increase in thermal conductivity to 1.8 W/(m·K) marks the boundary between the soft sediments and the more lithified rocks and breccias. Data scatter increases below 370 mbsf, reflecting the lithologic heterogeneity (see "Lithostratigraphy and Petrology" section, this chapter).

Discussion

The physical properties data obtained at Site 899 are heterogeneous, reflecting the variations in consolidation and lithology. Clearly, the most important discontinuity is the contact between the breccia units and the overlying sedimentary units. Variations in physical properties in the overlying sediments also suggest the existence of smaller-scale heterogeneities in lithology and/or consolidation.

Table 20. Thermal conductivity data from Holes 899A and 899B.

Core, section	Depth (mbsf)	Thermal conductivity (W/m·K)
149-899A-		
1R-1	82.25	1.80
1R-1	82.25	1.82
1R-3	85.25	1.56
2R-1	91.80	1.23
2R-1	91.80	1.31
2R-2	93.30	1.36
3R-1	101.50	1.18
3R-3	104.55	1.64
4R-1	111.17	1.43
5R-1	120.80	1.29
5R-3	123.80	1.24
6R-1	130.55	1.42
6R-3	133.40	1.28
7R-1	139.50	1.45
8R-1	149.30	1.21
8R-2	150.80	1.19
9R-1	159.00	1.59
9R-2	160.50	1.44
9R-3	162.00	1.23
10R-1	168.40	1.35
11R-1	178.30	1.27
11R-2	179.30	1.40
14R-2	208.85	1.33
14R-3	210.30	1.28
15R-1	217.05	1.36
15R-3	220.00	1.35
16R-1	226.60	1.15
16R-2	228.10	1.29
149-899B-		
1R-1	231.25	1.25
1R-3	233.92	1.34
2R-1	235.75	1.38
2R-3	238.53	1.32
3R-2	246.60	1.40
3R-4	249.65	1.30
3R-6	252.55	1.33
4R-2	256.25	1.37
4R-4	259.25	1.38
4R-6	261.70	1.37
5R-2	265.95	1.45
5R-4	269.00	1.44
6R-2	275.65	1.30
6R-4	278.75	1.36
6R-6	281.30	1.31
7R-2	285.23	1.59
7R-4	288.25	1.30
7R-6	291.10	1.24
8R-2	294.83	1.37
8R-4	297.80	1.37
8R-4	297.87	1.29
9R-2	304.35	1.38
9R-4	307.45	1.39
9R-6	310.21	1.50
10R-2	314.23	1.63
10R-4	317.28	1.31
10R-6	319.43	1.41
11R-2	323.80	1.55
11R-4	326.74	1.37
12R-2	333.48	1.50
12R-4	336.41	1.53
13R-2	343.05	1.58
13R-4	346.15	1.33
13R-6	349.10	1.40
14R-1	351.40	1.38
14R-3	354.34	1.25
15R-1	360.95	1.33
15R-3	363.95	1.37
16R-2	371.78	1.78
16R-4	374.30	1.80
17R-1	380.26	1.80
17R-3	383.10	1.78
18R-1	389.18	1.77
18R-3	392.67	1.86
18R-5	394.61	1.88
19R-1	399.56	1.85
19R-3	401.57	1.99
20R-1	408.43	1.84
20R-3	411.19	1.90
21R-1	417.72	2.26
21R-5	423.17	2.49
22R-2	428.25	2.24
23R-1	435.95	2.21
23R-3	439.49	1.74
23R-3	439.49	1.65
24R-3	448.98	1.78
25R-1	455.41	2.18
25R-2	457.03	2.28
25R-3	458.13	1.87
26R-1	465.33	1.46
27R-2	475.30	1.94
28R-1	483.55	1.88
29R-1	492.52	1.74
30R-2	503.49	1.66
31R-1	511.45	1.37
34R-1	538.96	1.79

DOWNHOLE LOGGING

Logging Operations

Four logging runs were made in Hole 899B with only partial success. The total penetration in Hole 899B was 562.5 mbsf. Casing was set to 216 mbsf in an attempt to reduce problems with upper hole stability encountered at earlier sites during Leg 149. Problems with hole stability continued despite the setting of casing and became severe within acoustic basement (Unit IV). The wiper trip made in preparation for logging showed numerous problem zones within the hole from 372 mbsf to total depth. The scientists thus decided to log in two phases. First, the basement was to be logged while holding the end of the pipe at 394 mbsf, just below the sediment/basement contact. The pipe then would be raised inside the casing and the rest of the uncased hole would be logged. This strategy was only partially successful, because obstructions within the acoustic basement prevented the logging tools from descending below 455 mbsf. Three logging runs were made with the pipe held at the 394 mbsf position; these were the geophysical combination, the nuclear-sonic combination, and the geochemical combination tools (see below). The decreasing extent of open hole between runs led to a decision to move the end of the pipe to 193 mbsf (within the casing) and to attempt to log the rest of the hole, beginning with the Formation Microscanner (FMS) string. This tool string was not able to penetrate more than a few meters beyond the end of the casing. Further attempts to log Hole 899B then were abandoned. A summary of the logging tool strings used during Leg 149 and the basis of their measurements is given in the "Explanatory Notes" chapter (this volume). The following is a summary of the logging runs:

1. Run 1, geophysical combination; drill-pipe depth: 394 mbsf. Logged interval: 394-455 mbsf; speed: 600 ft/hr (190 m/hr) Tools: natural gamma-ray/shear sonic/resistivity/temperature.
2. Run 2, nuclear/sonic combination; drill-pipe depth: 394 mbsf. Logged interval: 394-445 mbsf; speed: 1200 ft/hr (380 m/hr). Tools: natural gamma-ray/lithodensity/standard sonic (SDT)/temperature.
3. Run 3, geochemical combination; drill-pipe depth: 394 mbsf. Logged interval: 394-437 mbsf; speed: 600 ft/hr (190 m/hr). Tools: natural gamma-ray/lithodensity/induced gamma-ray spectrometry/aluminum activation/temperature.
4. Run 4, FMS; drill pipe/casing depth: 193 mbsf. Logged interval: Aborted, except for temperature measurement. Tools: natural gamma-ray/FMS/temperature.

Quality of Logs

The wireline heave compensator was used during all logging runs; sea conditions were calm with minimal swell. Two passes of the first two strings were made to test repeatability of the measurements.

The geophysical combination was run first; the quality of both passes on this run generally were good. No cycle skipping was apparent from the dipole shear imager tool (DSI), and good shear-wave interval traveltimes were recorded from both the dipole and monopole transmitters (Fig. 58). Sonic waveforms through the logged section are presented in Figure 59. Resistivity from the induction phaser tool was noisy and correlation among shallow, medium, and deep resistivities over these intervals is poor. The shallow resistivity was repeatable between the two passes, but the medium and deep resistivities had poor repeatability. The temperature tool malfunctioned and did not capture data.

The nuclear-sonic combination was run second, although an additional 10 m of fill in the hole decreased the logged interval. Bulk density data are of good quality, as verified by laboratory measurements on discrete samples from cores (Fig. 60; see below under "Core-log Integration" section, this chapter). Sonic data from the SDT are of varying quality, with clear cycle-skipping from the long-spaced receivers compromising the quality of the real-time data. These data will require reprocessing to improve the quality. Good quality interval traveltimes (delta T), however, were recorded from the short-spaced receivers with no apparent cycle-skipping. Delta T measurements (μs/ft) from the sonic tools run in the first two strings are compared in Figure 61. Incomplete wall contact of the CNT neutron tool rendered the neutron porosity data useless. Caliper data indicate a reasonably uniform borehole diameter through the section (10.5 in.; 27 mm), except for an increase of 1.5 in. (39 mm) at 405 mbsf. The temperature tool acquired satisfactory data.

The initial run of the geochemical combination was aborted when the geochemical tool neutron source failed during testing at 160 mbrf; the string then was recovered, and the geochemical tool replaced. A failure of the neutron source in the second tool at total depth, however, precluded any data acquisition from the induced gamma-ray spectrometry tool (GST). Natural gamma-ray and aluminum measurements were obtained from a depth of 437 mbsf (representing a further 8 m of hole fill) to the base of the drill pipe. Only a single pass was made with this tool string. During this run, the temperature tool (the same unit as was used during the first run) again failed to acquire data.

Measurements by the temperature tool were the only data acquired in the fourth logging run (FMS), which penetrated only a few meters below the base of the drill pipe. These data are of good quality, but began at a shallower depth (195 mbsf) than the previous temperature run.

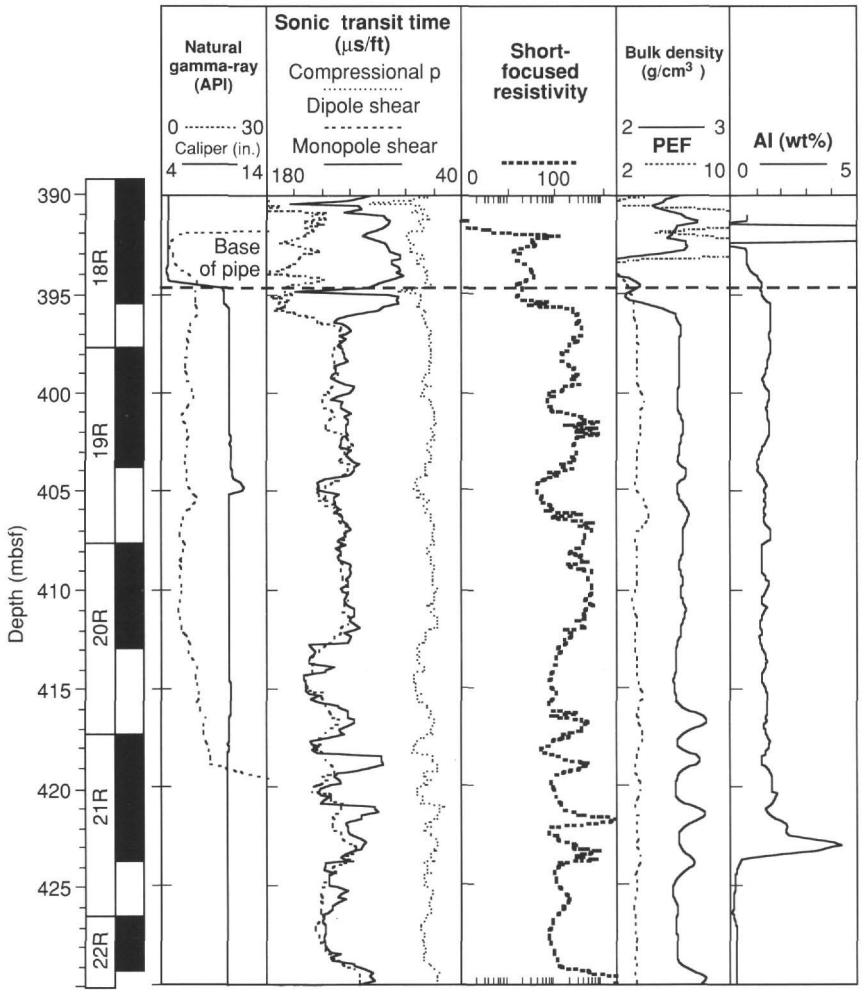

Figure 58. Composite plot of selected logs recorded in Hole 899B. Caliper, natural gamma-ray, bulk density, and photoelectric factor (PEF) data from the geophysical combination; sonic and resistivity data from the nuclear-sonic combination; and aluminum data from the geochemical combination. Core recovery is indicated in black in the left column.

Depth Shifting

Natural gamma-ray activity is below the reliable levels of detection for the spectroscopy mode (K, U, Th) and the total (K + U + Th) data (a mean of 8-10 API units) must also be regarded with caution. For this reason total NGT data were not used for depth shifting. Instead, five strong peaks recorded by the sonic, resistivity, and density tools provided much more reliable reference points for depth shifting. In addition, all nuclear data were subjected to a linear five-point (0.5 m) moving-average filter.

Temperature Data

Borehole temperatures measured by the Lament-Doherty temperature tool reflect the temperature of the seawater in the borehole, rather than the true formation temperature. The formation cools during drilling operations because of drill-fluid circulation and temperatures begin to rebound only after drilling has ceased. Data were obtained from the second and fourth runs, deployed 14 and 20 hr, respectively, after the wiper trip. The second run yielded a temperature of 13.8°C at a depth of 455 mbsf, while the fourth run measured 8.6°C at the deepest point, 193 mbsf. Measured bottom-water temperature was 2.4°C.

Logging Results

One characteristic log unit was determined from tool responses over the short interval logged. It is characterized by a general lack of change in log curves and correlates with the serpentinite breccia unit seen in the top of lithostratigraphic Unit IV. The main logs are summarized in Figure 58.

This unit is characterized by very low total natural gamma-ray values (of the order of 5-10 API units) and low aluminum content (1-1.5 wt%), which is indicative of an ultramafic lithology; it also exhibits a high resistivity from the short-focus log (100-120 Ωm), a low porosity (0%-10%), and a compressional-wave interval transit time of 70 to 80 μs/ft (corresponding to velocities of 4.3-3.8 km/s). A slightly higher interval transit time than that of pure serpentine (about 53 μs/ft or 5.75 km/s velocity) can be ascribed to the brecciated nature of the "matrix." The DSI sonic tool employed in the first string indicated a good shear-wave response from the monopole source that correlates very well with that from the dipole source and is indicative of a coherent, unfractured ("fast") crystalline formation (approximately 125-135 μs/ft; shear-wave velocity of 2.4-2.3 km/s).

Within the logged section, a local variation toward the base is shown by five distinct peaks that can be correlated between short-focus resistivity, bulk density, and sonic traveltime. These probably correspond to individual blocks of serpentinite within the brecciated subunit that systematically cause an increase in resistivity (up to 1000 Ωm), a decrease in traveltime (to 50 μs/ft, equivalent to 6.1 km/s), and a relative increase in bulk density of 0.25 g/cm^3 (resulting in a decrease in porosity to 0%-1%). High-resolution (2 in.) processing of the density data indicates that the vertical thickness of these blocks is on the order of 20 to 40 cm. An indication that a relatively permeable zone exists between 413 and 417 mbsf is illustrated by DSI Stoneley waveform data (Fig. 59B) and a corresponding decrease in focus

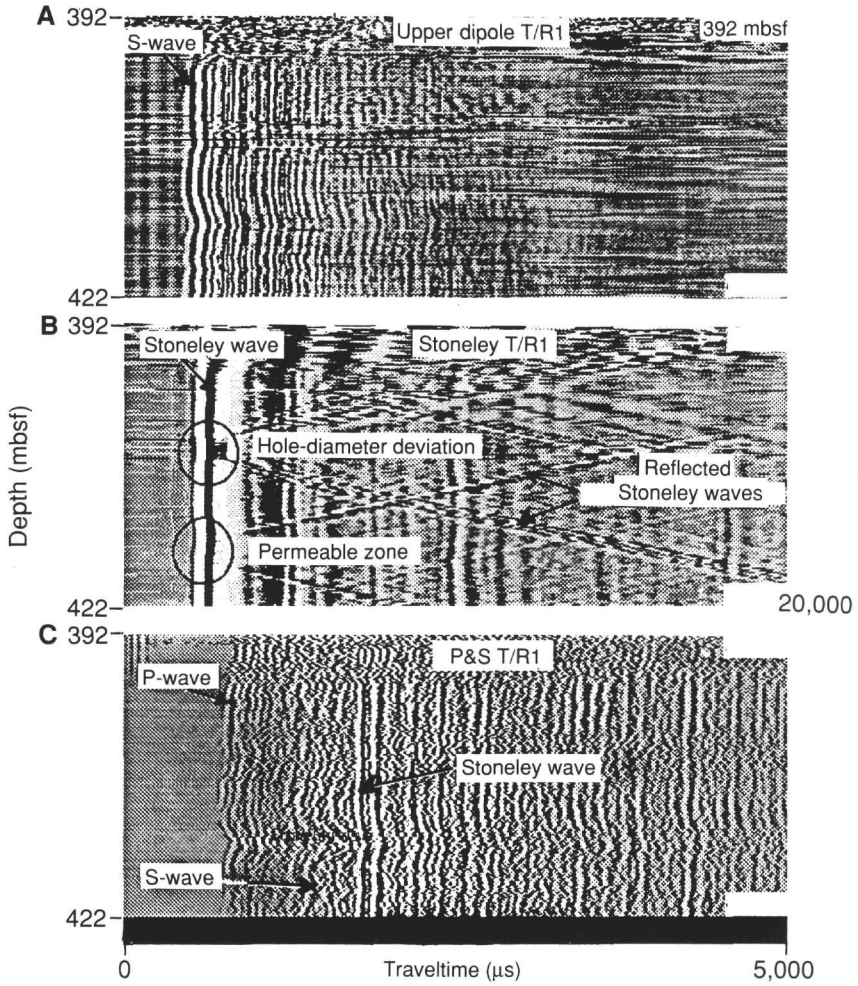

Figure 59. Sonic waveforms from the DSI tool over the logged interval of Hole 899B (392-422 mbsf). **A**. Waveforms generated by the upper dipole transmitter. **B**. Waveforms generated by the Stoneley monopole transmitter, indicating reflections from the caliper deviation at 404.5 m and a permeable zone between 413 and 417 mbsf. **C.** Waveforms generated by the P and S monopole transmitter. Horizontal axis is time, vertical axis is depth.

resistivity and shear-wave velocity (Fig. 58). The Stoneley waveform also indicates, very clearly, the borehole caliper deviation at 404.5 mbsf (Fig. 59B).

Core-log Integration

Bulk-densities derived from core measurements over the logged section correlate closely with the log-derived values (see Fig. 60). The core-derived bulk density (measured in discrete core samples in the laboratory) at 423.3 mbsf corresponds to one of the large serpentinite blocks (Interval 149-899B-21R-2, 78-81 cm) and probably correlates with one of the two distinct peaks (at 421 or 424 mbsf) in the log-derived bulk-density data. The difference between core and log measurements here is the result of a slight depth mismatch. In Figure 62, we compare laboratory-measured velocities with velocities derived from both sonic tools. In Figure 63, we compare laboratory-measured resistivity with log-derived resistivity (see the "Physical Properties" section, this chapter). In general, excellent agreement is seen between log-derived and discrete laboratory measurements in cores.

ONSHORE PROCESSING OF GEOCHEMICAL DATA

Geochemical Tool String

The geochemical logging tool string (GLT) consists of four separate logging tools: the natural gamma-ray spectrometry tool (NGT), the compensated neutron tool (CNT), the aluminum activation clay tool (AACT), and the gamma-ray spectrometry tool (GST). A schematic drawing of the GLT, which was run in Hole 899B, is shown in Figure 64. These four tools use three separate modes of gamma-ray spectroscopy for a comprehensive elemental analysis of the formation. The NGT is located at the top of the tool string so that it can measure the naturally occurring radionuclides, thorium (Th), uranium (U), and potassium (K), before the formation is irradiated by the nuclear sources contained in the lower tools (Fig. 64). The CNT, located below the NGT, contains a californium (^{252}Cf) neutron source to activate the Al atoms in the formation. The AACT, a modified NGT, is located below the ^{252}Cf source and measures the activated gamma rays in the formation. By combining the AACT measurement with the previous NGT measurement, the background radiation can be subtracted and a reading of formation Al is obtained (Scott and Smith, 1973). The gamma-ray spectrometry tool, at the base of the string, contains a pulsed neutron generator to induce prompt-capture gamma-ray reactions in the borehole and formation and an NaI(Tl) scintillation detector to measure the energy spectrum of gamma rays generated by the prompt-capture neutron reactions. As each of the elements in the formation is characterized by a unique spectral signature, it is possible to derive the contribution (or yield) of each of the major elements silicon (Si), iron (Fe), calcium (Ca), titanium (Ti), sulfur (S), gadolinium (Gd), and potassium (K) from the measured spectrum and, in turn, to estimate the relative abundance of each in the formation when combined with the elemental concentrations from the NGT and AACT. The GST also measures the hydrogen (H) and chlorine (Cl) in the borehole and formation, although these elements are not used for determining the rock geochemistry.

The only major rock-forming elements not measured by the geochemical tool string are magnesium (Mg) and sodium (Na); the neu-

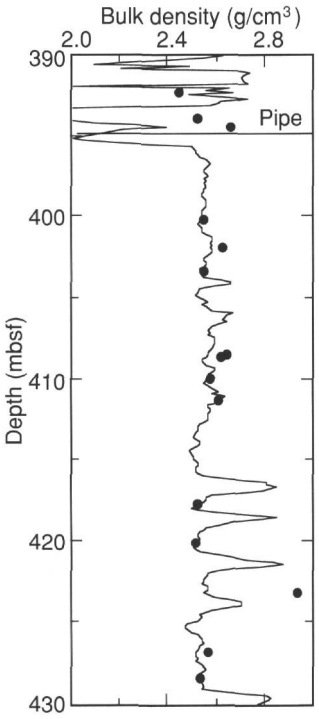

Figure 60. Log (lines) and shipboard discrete laboratory measurements (dots) of bulk density (g/cm^3). Excellent correlation can be observed. The discrepancy between the relatively high core-derived density and the log-derived density at 423.3 mbsf is ascribed to an error in computed core-depth because of incomplete core recovery.

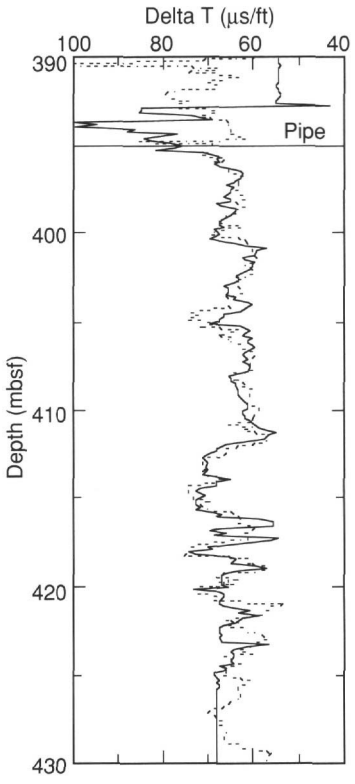

Figure 61. Compressional-wave delta T times from the SDT (solid line) and DSI (dashed line) tools.

tron-capture cross sections of these elements are too small relative to their typical abundances for the GLT to detect. Amounts of Mg + Na can be estimated in some instances by using the photoelectric factor (PEF), measured by the lithodensity tool (Hertzog et al., 1989).

As a result of the unfortunate failure of the neutron generator in both of the GST tools, no GST data were recorded. The NGT and AACT data were recorded successfully.

Data Reduction

The well-log data from the Schlumberger tools are transmitted digitally up a wireline and are recorded and processed on board the *JOIDES Resolution* in the Schlumberger Cyber Service Unit (CSU). Results from the CSU are made available as "field logs" for initial shipboard interpretation. Subsequent reprocessing is necessary to correct the data for the effects of fluids added to the well, logging speed, formation porosity, and drill-pipe interference.

The processing is performed with a set of log-interpretation programs written by Schlumberger, but that have been slightly modified to account for the lithologies and hole conditions encountered in ODP holes. The steps performed on the NGT and AACT data from Hole 899B are summarized next.

Depth Shifting

Geochemical processing involves the integration of data from the different tool strings; consequently, it is important that all the data are depth-correlated to one reference logging run. A reference run is chosen on the basis of constant, low cable tension and high cable speed (tools run at faster speeds are less likely to stick and are less susceptible to degradation of data caused by ship's heave). The depth-shifting procedure involves selecting a number of reference points based on similar log character and then invoking a program that expands and compresses the matching logging run to fit the reference logging run. The sonic-resistivity tool string was chosen as the reference run in Hole 899B.

Calculation of Total Radioactivity and Th, U, and K Concentrations

The second processing routine calculates the total natural gamma-ray radiation in the formation, as well as concentrations of Th, U, and K, using the counts in five spectral windows from the NGT (Lock and Hoyer, 1971). This routine resembles shipboard processing; however, the results are improved during post-cruise processing by including corrections for hole-size changes and temperature variations. A Kalman filter (Ruckebusch, 1983) is applied in the CSU processing at sea to minimize the statistical uncertainties in the logs, which can otherwise create erroneous negative values and anti-correlations (especially between Th and U). An alpha filter has been introduced more recently and is now recommended by Schlumberger for shore-based processing. This filter strongly smoothes the raw spectral counts, but keeps the total gamma-ray curve unsmoothed before calculating the Th, U, and K concentrations. The outputs of this program are K (wet wt%), U (ppm), and Th (ppm), as well as total and computed gamma rays (total gamma rays minus U contribution).

Calculation of Aluminum Concentrations

The third processing routine calculates the concentration of Al in the formation using four energy windows recorded on the AACT. During this step, corrections are performed for natural radioactivity, borehole-fluid neutron-capture cross section, formation neutron-capture cross section, formation slowing-down length, and borehole size.

Data from porosity and density logs need to be input into this routine to convert the wet-weight percentages of K and Al curves to dry-weight percentages (Fig. 65). A porosity log was calculated from

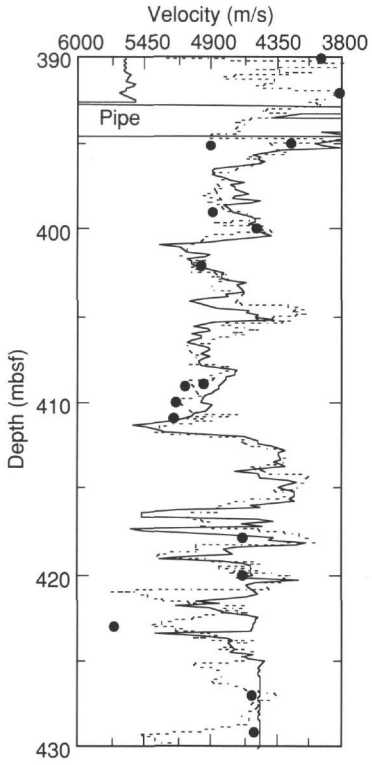

Figure 62. Comparison of compressional-wave velocities from the SDT (solid line) and DSI (dashed line) tools, and from shipboard discrete laboratory measurements (dots).

the deep induction log using Archie's relationship (1942). The program outputs dry-weight percentages of Al and K.

Calculation of Oxide Percentages

This routine converts the elemental weight percentages into oxide percentages by multiplying each by its associated oxide factor, as shown in Table 21. An error estimate for the oxides of K and Al is calculated using the total detector count rates and the logging speed on the basis of the algorithms of Schweitzer et al. (1988; Fig. 65).

INTEGRATION OF SEISMIC PROFILES WITH OBSERVATIONS FROM THE SITE

Two single-channel, seismic-reflection profiles were obtained across the site by the *JOIDES Resolution* during Leg 149 (Figs. 1 and 2). Consequently, these profiles are less distinct than multichannel profiles. Nevertheless, they show a number of reflectors that have been recognized on a regional scale in the vicinity of the Iberia Abyssal Plain and that have been dated by tracing them back to Leg 103 sites west of Galicia Bank (Mauffret and Montadert, 1988) and to Site 398 near Vigo Seamount (Groupe Galice, 1979). *JOIDES Resolution* Line 3 crosses the site in an east-west direction and one of these reflectors, separating acoustic formations 1A and 1B (Groupe Galice, 1979; Fig. 1), appears to cross the site. This reflector marks a regional unconformity produced by the folding that accompanied the Miocene compressional episode in the Rif-Betic Mountains to the south. The reflector has a rough indistinct surface near the site, which makes it difficult to recognize. The acoustic basement, which is composed of many hyperbolae, is not clearly seen at the base of the sedimentary section either.

Only very limited downhole measurements were obtained at Site 899; downhole velocity logs were obtained from 394 to 455 mbsf. However, the results of two sonobuoy lines shot over the Iberia

Table 21. Oxide factors used for normalizing elements to 100% and for converting elements to oxides.

Element	Oxide	Conversion factor
K	K_2O	1.205
Al	Al_2O_3	1.889

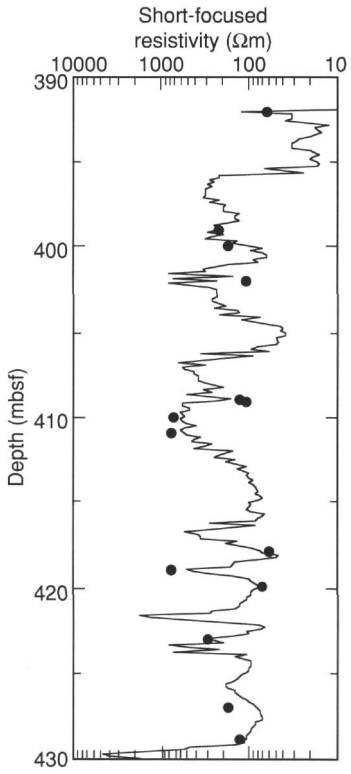

Figure 63. Comparison of short-focused resistivity measured by the phasor induction tool (solid line), and shipboard discrete laboratory measurements (dots).

Abyssal Plain (Whitmarsh, Miles, and Mauffret, 1990) were used to convert from two-way traveltime to depth (Fig. 66 in "Site 897" chapter, "Integration of Seismic Profiles with Observations from the Site" section, this volume). Thus, we did estimate the downhole depths of the formation 1A/1B and basement reflectors seen in the *JOIDES Resolution* Line 3 seismic-reflection profile; these are summarized in Table 22.

Findings

1. Reflector R1 (computed to be at 200 mbsf) is difficult to recognize in the vicinity of the site. Normally, it can be discerned from the angular relationship between the tilted and folded underlying, and horizontal onlapping, reflectors (Figs. 1 and 2). R1 may correlate with the onset at this site of a 3 m.y., late Miocene, hiatus that occurs at about 170 mbsf. This correlation implies a low interval velocity of 1.62 km/s from 0 to 170 mbsf and an improbable higher velocity between 170 mbsf and basement. It seems most likely, therefore, that R1 was picked too late in the seismic section, but the quality of the data does not allow us to make a more objective estimate.

2. The acoustic basement reflector has been computed to be at 360 mbsf. This reflector is evident in reflection profiles as a broad hyperbola, apparently within the sedimentary column. It correlates

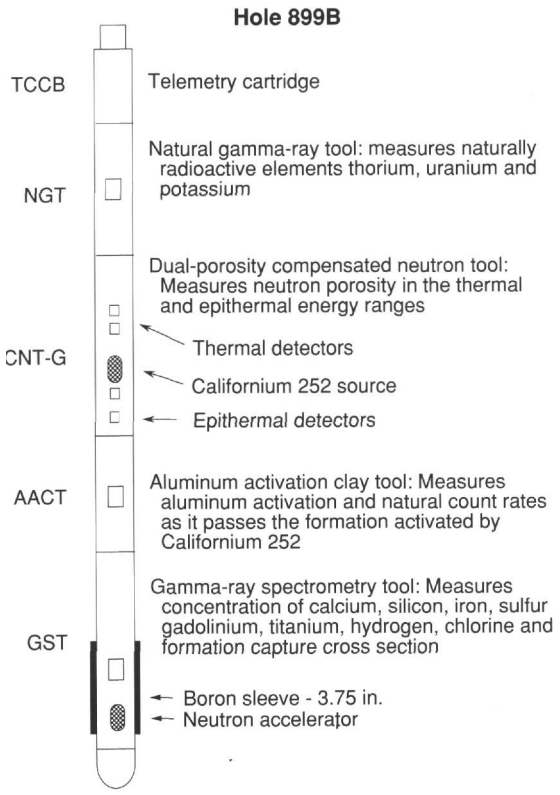

Figure 64. Schematic drawing of the Schlumberger geochemical logging tool string used for the Ocean Drilling Program.

with the serpentinite breccia at the top of Unit IV at 370 mbsf. The computed interval velocity from 0 to 370 mbsf is 1.95 km/s.

SUMMARY AND CONCLUSIONS

Site 899 is situated in the Iberia Abyssal Plain over a basement high within the presumed OCT zone off western Iberia (see "Introduction" chapter, this volume). The site is one of a transect of drill sites across the OCT designed to study the petrologic changes in the basement rocks within the OCT as a means of identifying the processes that accompanied continental breakup and the onset of steady-state seafloor spreading. The site is in a region between the thin oceanic crust to the west and the weakly magnetized, thinned continental crust to the east (see Fig. 4 in "Introduction" chapter, this volume), which is characterized by relatively high magnetization and a smooth acoustic basement between basement highs. Site 899 was chosen to sample an unusually shallow basement high that was discovered by chance while we were doing seismic profiling during Leg 149 and was chosen as an alternative drill site for Site 898 after the loss of about 3340 m of drill string. This site was an even more suitable site than Site 898 because it is closer to Site 897, thereby possibly allowing for stronger constraint on the location of the oceanward edge of the continent. The shallowness of the basement high also made it more accessible to drilling. The high is roughly circular in plan view with a steep southern slope and its shape contrasts strongly with that of the linear peridotite ridge at Site 897 and the north-south basement ridges and valleys further to the west (Fig. 2 in "Site 897" chapter, this volume). The high is located on the same subcircular positive magnetic anomaly as Site 898; the origin of this anomaly has yet to established. Two RCB holes were drilled at 40°46.3'N, 12°16.1'W with the primary scientific objective of penetrating basement to a depth sufficient to firmly establish its character. The first hole (899A) was washed to 81.5 mbsf and then drilled and cored from 81.5 to 235.5 mbsf to discover the depth to which casing should be set; a reentry cone and casing to 216 mbsf were installed at Hole 899B. The latter hole was drilled and cored to 562.5 mbsf until conditions at the bottom of the hole threatened the drill string and coring was stopped. Holes 899A and 899B yielded cores of Pliocene to Early Cretaceous age.

Table 22. Depths of reflectors in Hole 899A.

Reflector	Time (s TWT)	Computed depth (mbsf)	Estimated depth (mbsf)	Origin of reflector
R1	0.21	200	170	late Miocene hiatus/unconformity; acoustic formation 1A/1B boundary.
Basement	0.38	360	370	Top of serpentinite breccia.

The first event in the history of Site 899, which we can deduce from the cores, was the deposition in the Barremian to Aptian, a period of about 11 m.y., of blocks of peridotite with intercalated sediments and clasts of basalt, microgabbro and chlorite-bearing mylonite. Recovery of the cores from the deepest 70 m of Hole 899B was only about 10%. The mechanism of deposition is unknown. However, because the deposit is in many ways similar to the mass flow deposit cored at Site 897, we interpret it to be a series of mass flow deposits, too. There is an unusual variety of rock clasts in the cores. The results of Sites 897 and 899, only 10 nmi apart, suggest that there could have been an extensive area of peridotite exposed at the sea bed in Barremian time, perhaps even extending continuously between the two sites. We are confident that the peridotites were brought up to the sea bed by the final stretching and break-up of continental crust as Newfoundland separated from Iberia about 130 Ma (Whitmarsh, Miles, and Mauffret, 1990). The sources of the basalt and microgabbro are uncertain. The basalt is not a MORB-type basalt, which means it is not likely to have clear oceanic affinities. On the other hand, neither microgabbro nor basalt have been reported in dredge hauls from the west Iberia margin (Capdevila and Mougenot, 1988); thus, the sources of these rocks remain enigmatic. A curious feature of these mass flows is that they were cored close to the top of the highest known basement high in the area. Because mass flows move downhill, it is hard to see how clasts from tens of miles away, or farther, reached their present position as this implies that they were transported uphill. One is forced to conclude that there may have been a different arrangement of basement relief in the Early Cretaceous and the site (which is now a high) underwent significant uplift relative to its surroundings after deposition of the mass flow. A similar hypothesis was considered for the origin of the mass flow deposit cored at Site 897.

The mass flows were followed by deposition, which we can constrain to have occurred only in late Aptian to Latest Cretaceous (Campanian/Maastrichtian) time, of at least 3 layers of serpentinized peridotite breccia. Based on dates obtained from nannofossils, the mass flows and breccia units contain intercalated sediments which young upwards. Therefore, the whole sequence appears to be a normal rock succession. Because the breccia units (1) lack clasts of continental crystalline basement rock and sediment and contain only a few possible clasts of basalt and gabbro, (2) contain mainly cataclastic textures and very angular microscopic clasts suggestive of a very short transport path, and (3) are chemically indistinguishable in bulk and trace element composition from the peridotites of Hole 897D, we conclude that their source was much more local than that of the underlying mass flows and did not allow incorporation of other rock types. The three breccia units we observed appear to have the characteristics of rapidly deposited flows with shear deformation under low normal stress typical of high fluid pressures. The unusual character of these breccias and their almost unique occurrence in the oceans makes it difficult at present to establish the mechanism of their deposition. The sole possible analog known to the Shipboard Scientific Party is the active flows drilled in the Izu-Bonin-Mariana region during ODP Leg 125 (Fryer, Pearce, Stokking, et al., 1990). These flows, however,

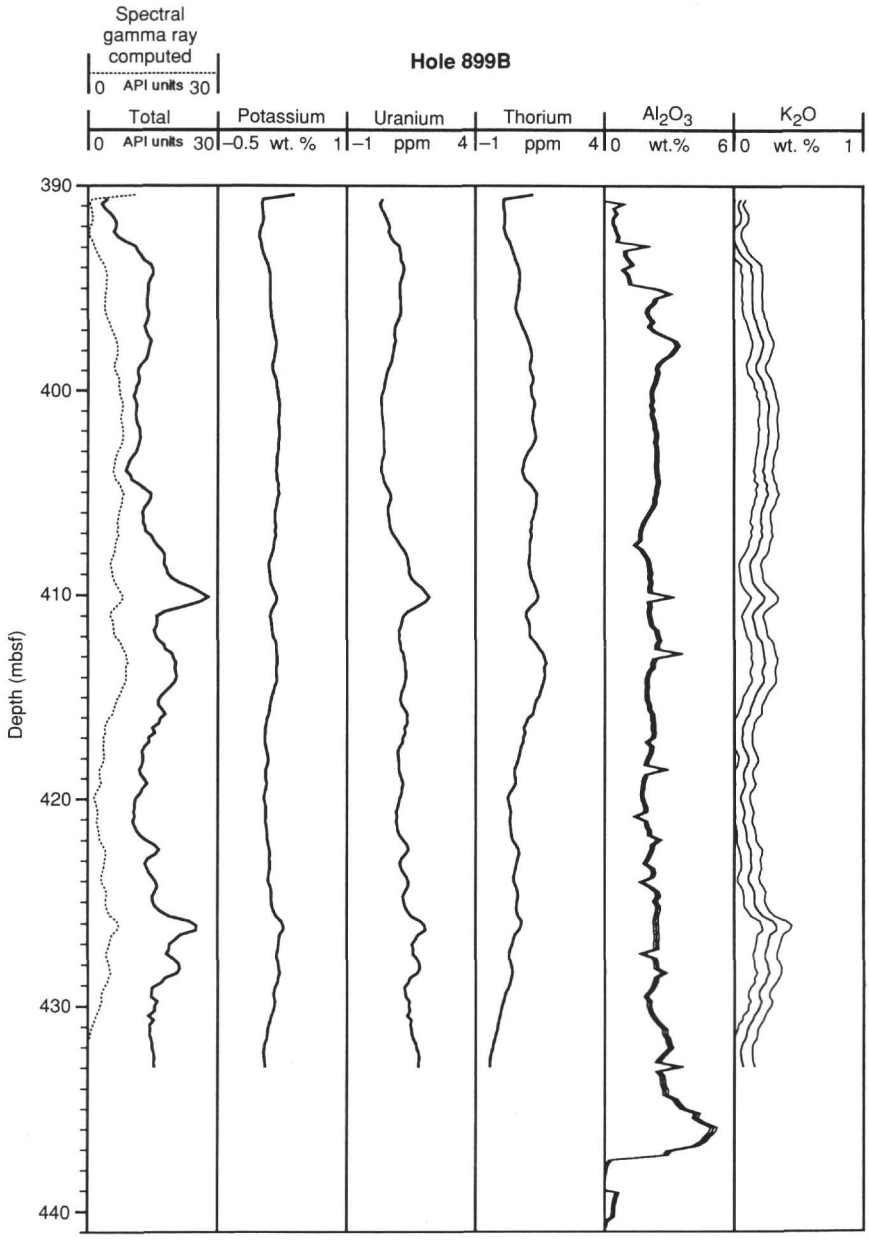

Figure 65. Processed natural gamma-ray data, estimates of potassium, uranium, and thorium and of Al_2O_3 and K_2 oxide weight fractions, and error bounds of Al_2O_3 and K_2O from Hole 899B.

are located in a forearc regime that at first glance appears very different from the rifted margin drilled during Leg 149. However, one can point out some clear similarities with breccias called "ophicalcites," encountered in some ophiolitic massifs of the western Alps (Queyras, Davos, Appenines). Because the Site 899 breccia units appear to be a kind of flow and were drilled near the top of the highest known basement in the area, we can reasonably postulate that they came from the same high (the fact that the "high" may have been lower during the deposition of the mass flow deposit does not rule out this conclusion as the "high" may have been uplifted between then and the deposition of the breccias). The breccia units appear to have been emplaced sometime between 18 and 65 m.y. after the estimated time of onset of seafloor spreading (Whitmarsh, Miles, and Mauffret, 1990) at this segment of the margin.

The top of the igneous/metamorphic crust probably was not sampled at this site. It is not clear if we have found unequivocal evidence at Site 899 for either a continental or an oceanic nature of the basement. In fact, it seems most likely that there is no crust at all beneath the site, only upper mantle peridotite and that the clasts transported to the site came from a geological environment characterized by a range of rock types, which have oceanic (the gabbros and radiolarian chert), non-oceanic (non-MORB basalts), and continental (felspathic siltstone) affinities. Such a region can probably be properly described as transitional between continental and oceanic crust.

After the deposition of the last breccia unit, a hiatus is seen in the depositional record until late Eocene (ca. 39 Ma). Immediately preceding this hiatus, a poorly cemented Campanian/Maastrichtian conglomerate with clasts of metasediments, claystone, and basalt was deposited. This may have developed as a weathering deposit with reworked material from the underlying breccia unit. The conglomerate is overlain by a few meters of fine-grained hemipelagic/pelagic deposits and high density turbidite or mass flow deposits, followed by carbonate-poor claystones, which resulted from slow accumulation in an oxygenated environment probably below the CCD.

The remaining sediments cored at this site reveal a history of sedimentation on an evolving continental margin, starting with current reworking of turbiditic sediments, followed by turbidite deposition. From the late Eocene until the middle Miocene, a sequence of

more or less carbonate-rich claystone or siltstone having significant amounts of biogenic siliceous material was deposited above the CCD. An important characteristic of these sediments is the presence of upward-darkening sequences. These range in thickness from 10 to 30 cm, usually have sharp bases and tops, and are intensely bioturbated. These features and small-scale structures in the cores point to reworking by contour currents in an abyssal plain setting. At the same time, evidence was seen of downslope sediment movement in the form of occasional mud turbidites.

The upward-darkening sequences ended in the middle Miocene. They were succeeded by clays, calcareous clays, and nannofossil clays. For the most part, these were the result of pelagic sedimentation, but occasional turbidites also carried siliciclastic sand and silts or nannofossil clay material. Moderate to intense bioturbation indicates relatively slow sediment accumulation (computed to be from 9 to 29 m/m.y.). Deposition was in an abyssal plain setting dominated by pelagic and hemipelagic sedimentation. A 2.9 m.y. hiatus beginning in the middle Miocene (12 Ma), correlates with a regional angular unconformity on seismic reflection profiles, probably caused by northwest-southeast compressional phase in the Betic Mountains in southeastern Spain, and structural inversion in the Lusitanian Basin of Portugal. Sedimentation then continued until the end of the Miocene.

The final phase of sedimentation at this site began in the early Pliocene with the onset of turbidite deposition with interbedded pelagic/hemipelagic sediments. The overall rate of sediment accumulation increased to about 35 m/m.y. The turbidites range in thickness from 5 to 150 cm and have basal sandy silt to silty sand layers that appear to be thicker in the more recent turbidites. Bioturbation is common, but lamination is seen in only a few sands. Because we did not core the section from the seabed to 81.5 mbsf, our history of the turbidite sedimentation ends in the late Pliocene.

REFERENCES*

Archie, G.E., 1942. The electrical resistivity log as an aid in determining some reservoir characteristics. *Trans. Am. Inst. Min. Metall. Pet. Eng.,* 146:54-62.

Beslier, M.-O., Ask, M., and Boillot, G., 1993. Ocean-continent boundary in the Iberia Abyssal Plain from multichannel seismic data. *Tectonophysics,* 218:383-393.

Bouma, A.H., 1962. *Sedimentology of Some Flysch Deposits: A Graphic Approach to Facies Interpretation:* Amsterdam (Elsevier).

Boyce, R.E., 1973. Physical properties—methods. *In* Edgar, N.T., Saunders, J.B., et al., *Init. Repts. DSDP,* 15: Washington (U.S. Govt. Printing Office), 1115-1128.

Bralower, T.J., Monechi, S., and Thierstein, H.R., 1989. Calcareous nannofossil zonation of the Jurassic-Cretaceous boundary interval and correlation with the geomagnetic polarity time scale. *Mar. Micropaleontol.,* 14:153-235.

Capdevila, R., and Mougenot, D., 1988. Pre-Mesozoic basement of the western Iberian continental margin and its place in the Variscan Belt. *In* Boillot, G., Winterer, E.L., et al., *Proc. ODP, Sci. Results,* 103: College Station, TX (Ocean Drilling Program), 3-12.

Claypool, G.E., and Kvenvolden, K.A., 1983. Methane and other hydrocarbon gases in marine sediment. *Annu. Rev. Earth Planet. Sci.,* 11:299-327.

Emerson, S., and Hedges, J.I., 1988. Processes controlling the organic carbon content of open ocean sediments. *Paleoceanography,* 3:621-634.

Folk, R.L., 1980. *Petrology of Sedimentary Rocks:* Austin (Hemphill Publ.).

Fryer, P., Pearce, J.A., Stokking, L.B., et al., 1990. *Proc. ODP, Init. Repts.,*125: College Station, TX (Ocean Drilling Program).

Gealy, E.L., 1971. Saturated bulk density, grain density, and porosity of sediment cores from the western Equatorial Pacific: Leg 7, *Glomar Challenger. In* Winterer, E.L., Riedel, W.R., et al., *Init. Repts. DSDP,* 7 (Pt. 2), Washington (U.S. Govt. Printing Office), 1081-1104.

Gieskes, J.M., 1974. Interstitial water studies, Leg 25. *In* Simpson, E.S.W., Schlich, R., et al., *Init. Repts. DSDP,* 25: Washington (U.S. Govt. Printing Office), 361-394.

————, 1983. The chemistry of interstitial waters of deep-sea sediments: interpretation of deep-sea drilling data. *In* Riley, J.P., and Chester, R. (Eds.), *Chemical Oceanography* (Vol. 8): London (Academic Press), 222-269.

Groupe Galice, 1979. The continental margin off Galicia and Portugal: acoustical stratigraphy, dredge stratigraphy, and structural evolution. *In* Sibuet, J.-C., Ryan, W.B.F., et al., *Init. Repts. DSDP,* 47 (Pt. 2): Washington (U.S. Govt. Printing Office), 633-662.

Hertzog, R., Colson, L., Seeman, B., O'Brien, M., Scott, H., McKeon, D., Wraight, J., Grau, J., Ellis, D., Schweitzer, J., and Herron, M., 1989. Geochemical logging with spectrometry tools. *SPE Form. Eval,* 4:153-162.

Lock, G.A., and Hoyer, W.A., 1971. Natural gamma-ray spectral logging. *Log Analyst,* 12:3-9.

Martini, E., 1971. Standard Tertiary and Quaternary calcareous nannoplankton zonation. *In* Farinacci, A. (Ed.), *Proc. 2nd Int. Conf. Planktonic Microfossils Roma:* Rome (Ed. Tecnosci.), 2:739-785.

Mauffret, A., and Montadert, L., 1988. Seismic stratigraphy off Galicia. *In* Boillot, G., Winterer E.L., et al., *Proc. ODP, Sci. Results,* 103: College Station, TX (Ocean Drilling Program), 13-30.

McIver, R., 1975. Hydrocarbon occurrence from JOIDES Deep Sea Drilling Project. *Proc. Ninth Petrol. Congr.,* 269-280.

Myers, P.A., in press. Preservation of source identification of sedimentary organic matter during and after deposition. *Chem. Geol.*

Müller, P.J., 1977. C/N ratios in Pacific deep sea sediments: effect of inorganic ammonium and organic nitrogen compounds sorbed by clays. *Geochim. Cosmochim. Acta,* 41:765-776.

Perch-Nielsen, K., 1985. Mesozoic calcareous nannofossils. *In* Bolli, H.M., Saunders, J.B., and Perch-Nielsen, K. (Eds.), *Plankton Stratigraphy:* Cambridge (Cambridge Univ. Press), 329-426.

Rio, D., Fornaciari, E., and Raffi, I, 1990. Late Oligocene through early Pleistocene calcareous nannofossils from western equatorial Indian Ocean (Leg 115). *In* Duncan, R.A., Backman, J., Peterson, L.C., et al., *Proc. ODP, Sci. Results,* 115: College Station, TX (Ocean Drilling Program), 175-235.

Robaszynski, M., Caron, M., Gonzalez Donoso, J.M., Wonders, A.A.H., and Eur, W.G., 1984. Atlas of Late Cretaceous Globotruncanids. *Rev. Micropalentol,* 26:145-305.

Ruckebusch, G., 1983. A Kalman filtering approach to natural gamma ray spectroscopy in well logging. *IEEE Trans. Autom. Control,* AC-28:372-380.

Schweitzer, J.S., Grau, J.A., and Hertzog, R.C., 1988. Precision and accuracy of short-lived activation measurements for in situ geological analyses. *J. Trace Microprobe Techn.,* 6:437-451.

Scott, H.D., and Smith, M.P., 1973. The aluminum activation log. *Log Analyst,* 14:3-12.

Shipboard Scientific Party, 1979. Site 398. *In* Sibuet, J.-C., Ryan, W.B.F., et al., 1979. *Init. Repts. DSDP,* 47(Pt. 2): Washington (U.S. Govt. Printing Office), 25-233.

Sissingh, W., 1977. Biostratigraphy of Cretaceous nannoplankton. *Geol. Mijnbouw,* 56:37-50.

Stow, D.A.V., and Piper, D.J.W., 1984. Deep-water fine-grained sediments: facies models. *In* Stow, D.A.V., and Piper, D.J.W. (Eds.), *Fine-grained Sediments: Deep-Water Processes and Facies.* Geol. Soc. Spec. Publ. London, 15:611-645.

Suess, E., 1980. Particulate organic carbon flux in the oceans—surface productivity and oxygen utilization. *Nature,* 288:260-263.

Whitmarsh, R.B., Miles, PR., and Mauffret, A., 1990. The ocean-continent boundary off the western continental margin of Iberia, I. Crustal structure at 40°30'N. *Geophys. J. Int.,* 103:509-531.

Whitmarsh, R.B., Pinheiro, L.M., Miles, PR., Recq, M., and Sibuet, J.C., 1993. Thin crust at the western Iberia ocean-continent transition and ophiolites. *Tectonics,* 12:1230-1239.

*Abbreviations for names of organizations and publication titles in ODP reference lists follow the style given in *Chemical Abstracts Service Source Index* (published by American Chemical Society).

Ms 149IR-106

NOTE: For all sites drilled, core-description forms ("barrel sheets") and core photographs have been reproduced on coated paper and can be found in Section 3, beginning on page 271. Forms containing smear-slide data can be found in Section 4, beginning on page 657. Thin-section data are given in Section 5, beginning on page 679. Index Property and MAGSUS data are presented on CD-ROM (back pocket).

Hole 899B: Resistivity-Natural Gamma Ray Log Summary

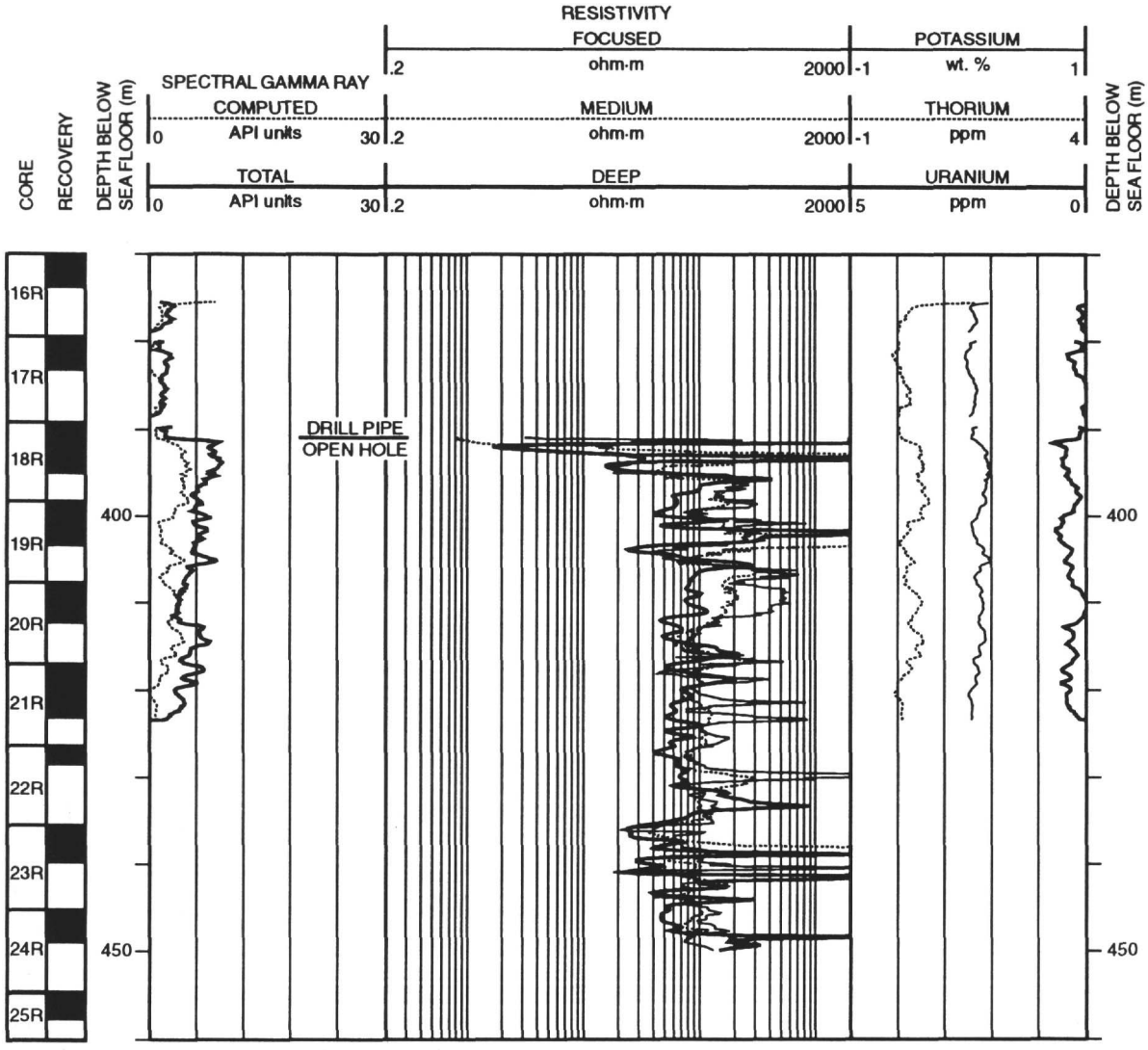

Note: These data were reprocessed post-cruise by the Borehole Research Group, Lamont-Doherty Earth Observatory of Columbia University.

Hole 899B: Velocity-Natural Gamma Ray Log Summary

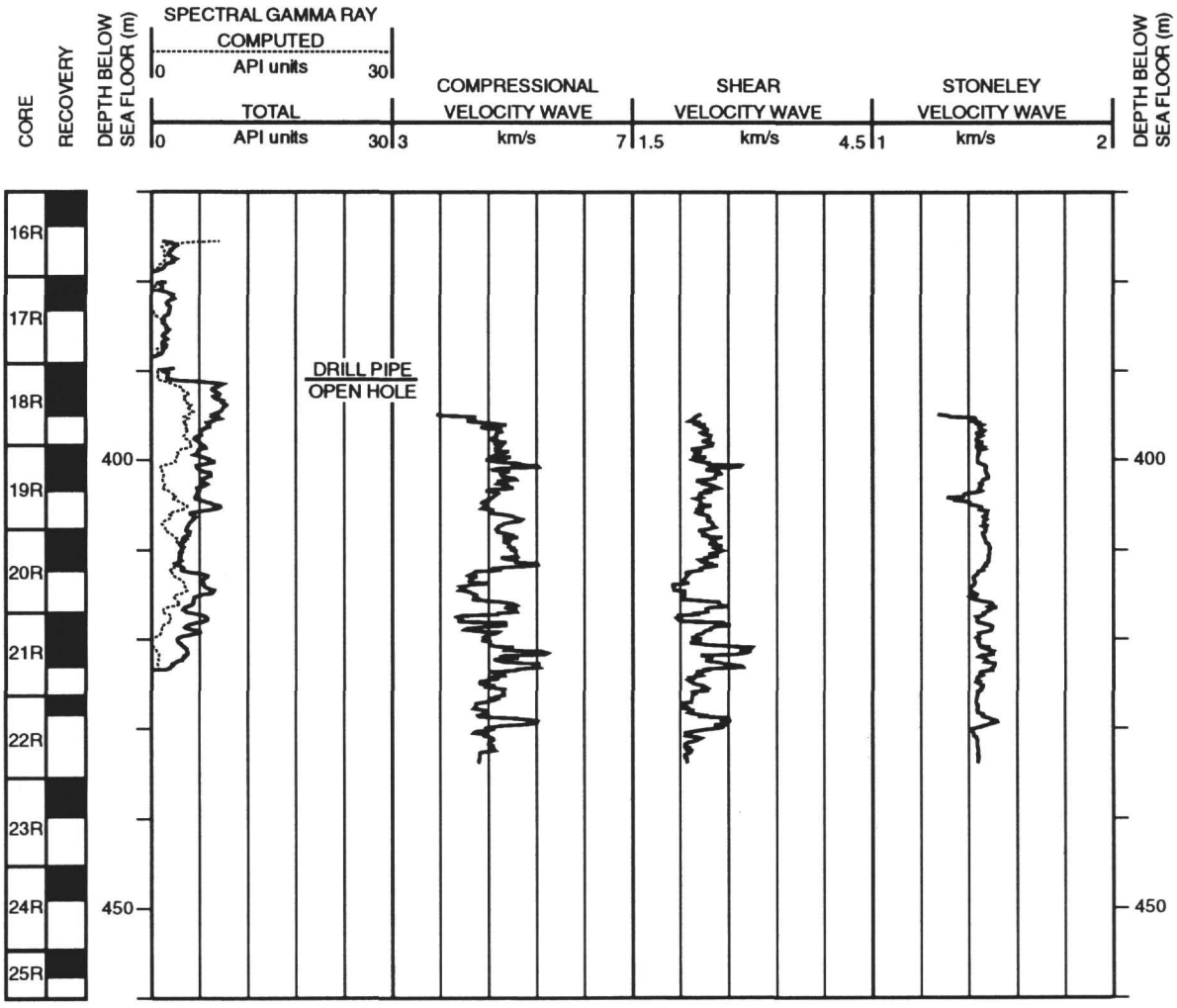

Hole 899B: Velocity-Natural Gamma Ray Log Summary

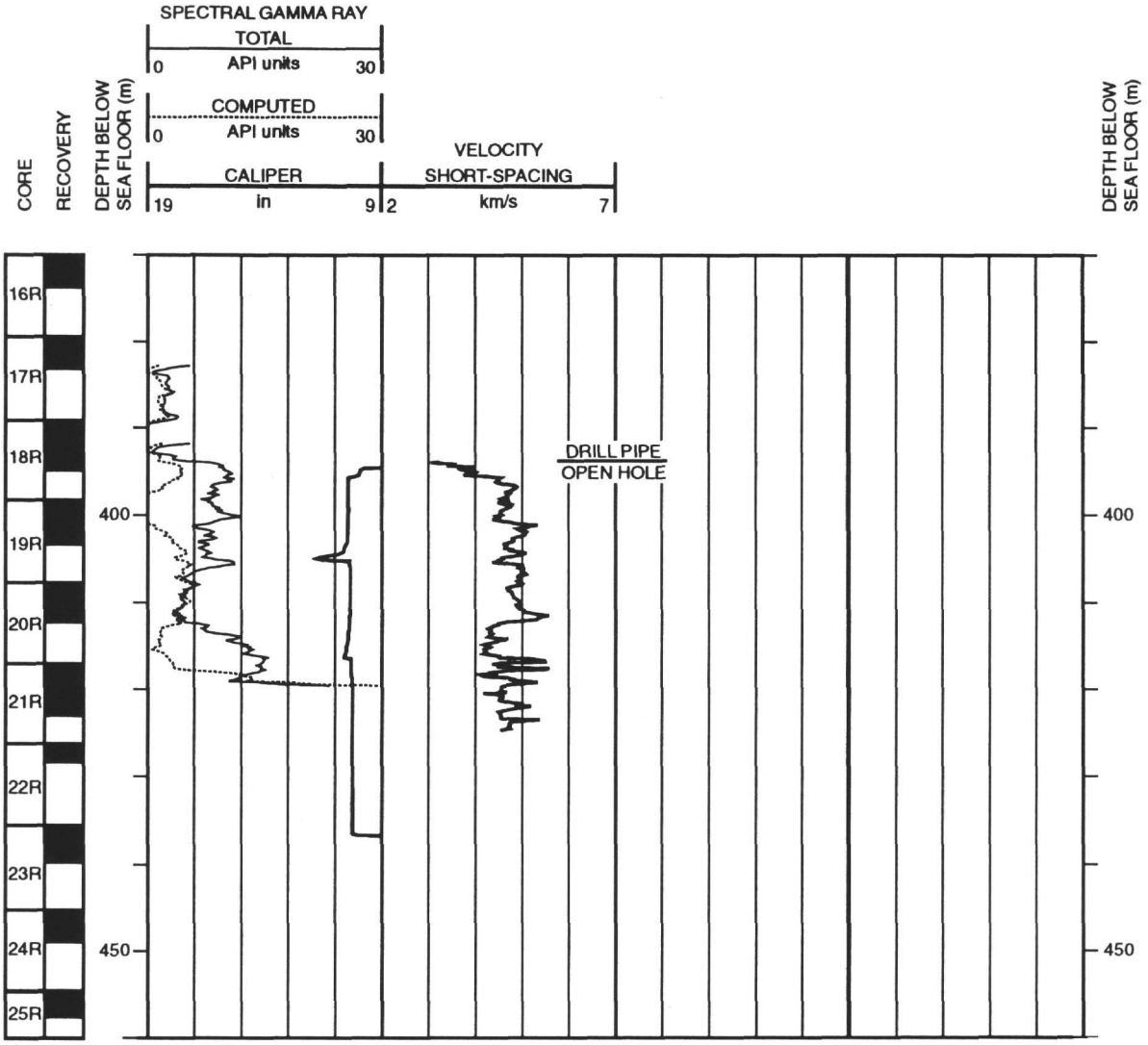

Hole 899B: Density-Porosity-Natural Gamma Ray Log Summary